Environmental factors influencing the spatial distribution of geogenic radon sources (uranium, radium) in a granitic area

by

Silvana Beltrán Torres

Ph.D. Program of Environmental Geology, Doctoral School of Environmental Sciences, Faculty of Science, Eötvös Loránd University

Ph.D. thesis

submitted to:
Doctoral School of Environmental Sciences (Prof. Jánosi Imre)
Program of Environmental Geology (Dr. Szabó Csaba)

Supervisors:

Katalin Zsuzsanna Szabó, Ph.D.
Nuclear Security Department
Hungarian Academy of Sciences
Centre for Energy Research

Csaba Szabó, Ph.D.
Lithosphere Fluid Research Lab
Institute of Geography and Earth Sciences
Eötvös Loránd University

June 2019
Budapest, Hungary

Acknowledgements

This research has been supported by the Stipendium Hungaricum Scholarship Program 2015-2018, and the National Research, Development and Innovation Office – NKFIH, PD115810. Additional support is from the New National Excellence Program of Human Capacities ÚNKP-18-3IV-ELTE-424.

All of my gratitude to my supervisor Professor Csaba Szabó and my co-supervisor Katalin Zsuzsanna Szabó for their guidance and support, without whom I wouldn't be able to reach my goals.

I am grateful to Mining Support Ltd. for the AlphaGUARD instrument and to Zsolt Homoki, National Public Health Center for the Radon-JOK equipment used in the project. I would like to thank Győző Jordán, Zsuzsanna Szabó, Attila Petrik, György Falus for their contribution. Special thanks to Ákos Horváth for his help and for the RAD7 instrument used in this research. I am grateful to Tibor Kovács, Anita Csordás, Gergő Bátor, Jácint Jónás from the Institute of Radiochemistry and Radioecology, University of Pannonia Veszprém, for their great collaboration with laboratory analysis. On the same way, thank of the Department of Soil Science and Agricultural Chemistry, Szent István University, Gödöllő for their assistance. I am thankful to the Laser Diffraction Particle Size Distribution Analyzer Laboratory, of the Research and Instrument Core Facility of Faculty of Sciences, Eötvös Loránd University specially to Csilla Király whom made this possible as well as Davaakhuu Tserendorj and Nelson Salazar. Thanks to Zsolt Benkó and László Kupi whose knowledge and experience in Velence granites helped during this work. Thanks to Professor Agi Gál for her friendship and the time we shared; it was a pleasure meeting you.

I am highly thankful to the members of Lithosphere Fluid Research Lab for all their help and support, specially to my colleagues László Aradi, Levente Patkó, Ábel Szabó, Csilla Király, Viktória Forray, Judith Pena Dembo, and Zoltán Kovács for their unconditional help and kindness since I arrived in Budapest with whom I shared great moments in these almost four years. I would like to thank to the persons who contributed in any way to the development of this work: Imane Hachoumi, Mehdi Oubame, Nóra Demeter, Diana Suasnavas, Prospero Dachala, Anna Dömök, Niki, Betti and Marci. Many thanks to Éva Bíró and Andrea Förherczné for their kindly help in administrative procedures.

During this journey far from home, I was so blessed to meet such incredible people with a warm hearth who helped me during the hardest time, to whom I am sincerely thankful.

I will be always thankful to Mauricio Moreno-Zambrano for his endless support, help, patience and for being my strength in the hardest period, thanks my love for everything. Although, the words will never be enough, I would like to thank to my mother Gladys Torres for all she has done for me, for all her kindness, infinite love, for always encouraging me to reach my goals. Finally, a big thanks for the support of my beloved nieces Nathaly, Stephanie and Romy whom are always my inspiration.

Table of Contents

Table of figures

Table of tables

1. Introduction and objectives

In average, the population receive a total effective dose of 2.4 mSv y^{-1} from natural sources, terrestrial radioactivity is the responsible of approximately 84 % (2.02 mSv y^{-1}) (UNSCEAR, 2008). Gamma radiation is the principal source of natural external radiation, which contributes with 0.48 mSv y^{-1} to the total effective dose. Internal exposure occurs by inhalation or ingestion of radionuclide (UNSCEAR, 2008). Radon is the main source of internal exposure to natural ionizing radiation (1.15 mSv y^{-1}) and represents the second cause of lung cancer after smoking (UNSCEAR, 2000).

Due to the risk that the internal and external exposure to the natural radioactivity represents for human health, national and supranational institutions have established normative to minimize the risk. In the European Union, the European Commission proposed in the newest Euratom Basic Safety Standards (BSS) announced on December 2013 (Council Directive 2013/59/Euratom 2013) to establish reference level for indoor radon concentration and to develop national radon action plan aiming to minimize radon risk exposure. These include to assess relevant parameters for indoor radon such as permeability, ^{226}Ra concentration and provide scientifically based maps of potential natural radioactivity hazard. In this framework, the Hungarian Government established the highest value determined by the Directive, 300 Bq m^{-3} for indoor radon concentrations in workplaces, public buildings and dwellings through Govt. Decree 487/2015, effective as of January 2016. Complementing the national efforts to identify and document the radon prone areas, the Joint Research Centre (JRC) leads and permanently develops the European Atlas of Natural Radiation project since 2006 (Bossew et al., 2015, 2013; Cinelli et al., 2018; De Cort et al., 2011). That project includes the European maps of annual cosmic-ray dose, indoor radon, uranium, thorium and potassium concentration in soil and in bedrock, terrestrial gamma dose rate, soil permeability, and geogenic radon. Digital version of the atlas is already available (Cinelli et al., 2018).

This research aims to asses important information for the use/formulation of predictive models and for construction of maps regarding to the sources of natural radioactivity with final goal to identify areas where natural radiation is elevated by the understanding its relationship with local geology and properties of the soil and rocks. In this framework, this

project focuses on the detailed study of terrestrial natural radioactivity through the evaluation of the most important sources of external and internal exposure: ambient gamma dose equivalent rate and soil gas radon activity concentration respectively. This research is conducted in a granitic area, considering that elevated radiation levels generally are associated with this type of acidic igneous rocks (UNSCEAR, 2000) due to its formational process.

The characterization of the study area in terms of ambient gamma dose equivalent rate, as the main contributor of external exposure, started with an extensive field campaign in the largest granitic outcrop in Hungary located in the western side of the Velence Hills. A detailed spatial analysis of the measured ambient gamma dose equivalent rate was performed. Digital spatial analysis methods were applied to the measured data in order to identify spatial pattern such as anomalies, heterogeneities and linear features. The identified features were then related to the underlying geological formations and geological structures such as faults and dikes by means of GIS spatial analysis techniques and statistical correlation analysis. This research contributes with the application of a quite novel technique in this field, which were already applied successfully in a different area for soil gas radon concentration and for ambient gamma dose equivalent rate, but with lower resolution (Szabó et al., 2014, 2017). Also, this study contributes the identification the influence of geological features in the ambient gamma dose equivalent rate (Beltrán Torres et al., 2018).

The main contributor of internal exposure from geogenic sources is radon. A commonly used evaluation of radon is based on the determination of its potential risk to the human health. One definition to quantify this geogenic radon hazard is radon potential (RP), also used as geogenic radon potential (GRP). The mathematical expression used for the quantification of RP is the proposed by Neznal et al. (2004), which involves soil gas radon concentration and soil gas permeability. The RP is currently assessed by direct field measurements of these parameters. However, to generate this information in a national or regional scale involves long term campaigns and economical resources. Consequently, there are still vast areas lacking this assessment. In Hungary, although areas with elevated natural radioactivity are well studied, there is no large scale mapping with the exception of the first geogenic radon potential mapping, carried out by Szabó et al. (2014) in Pest County. Thus, the approach of this research contemplates the evaluation of the usability of the theoretical

and empirical models to predict soil gas radon concentration and soil gas permeability. An important criterion for the selection of this models is the use of soil properties that can be found in national and international databases to ensure its applicability. Two theoretical models to predict soil gas radon concentration and one empirical model for soil gas permeability are evaluated by comparison with the field measured corresponding parameters. The soil properties that are involved in the after mentioned models were determined as well as the properties that influences directly or indirectly the soil gas radon concentration and soil gas permeability. The effect of the influencing soil parameters in soil gas radon concentration as soil gas permeability is evaluated to determine the controlling factors of the spatial distribution of radon geogenic sources. Finally, the predictive power of the models is corrected by the modification of the evaluated models.

2. Natural radioactivity

2.1. Types of nuclear radiation

Nuclear radiation is the energy emitted by an atom with an unstable nucleus (radioactive parent) when it decays to a more stable state (radioactive progeny) leading to a new atomic configuration. When the emitted energy is high enough to ionize the adjacent atoms is known as ionizing radiation and can take either the form of particles or waves (Blin-Stoyle, 1991). There are three main types of nuclear radiation: (1) alpha decay, (2) beta decay and (3) gamma rays.

2.1.1. Al**pha decay**

In this type of nuclear radiation an alpha particle ($^{4}_{2}$He) is emitted during the decay, producing a radioactive progeny that possesses higher binding energy than the radioactive parent. This extra energy can be released as kinetic energy (recoil energy) causing the recoil of the radioactive progeny (Blin-Stoyle, 1991). For example, the alpha decay of ^{226}Ra to ^{222}Rn ($^{226}_{88}Ra \rightarrow {}^{222}_{86}Rn + {}^{4}_{2}He$) is accompanied with 4.874 MeV (see Figure 2) alpha energy release (Bourdon et al., 2003).

Subsequently to the decay of parent radium isotopes (^{226}Ra, ^{224}Ra), the progenies radon (^{222}Rn) and thoron (^{220}Rn) isotopes are emitted kinetic energies of 86 and 123 keV, respectively and they are moving from the point of generation until the energy that is transferred to the material (Porstendorfer, 1994). The distance travelled is approximately from $4x10^{-2}$ μm up to $6x10^{-2}$ μm in granular material and $6x10^{-1}$ μm in the atmosphere (Gurau et al., 2014)

2.1.2. Beta decay

There are three mechanisms by which beta decay can occur, depending on whether an electron or positron is emitted, or an electron is captured by the nuclei (Blin-Stoyle, 1991):

- *Beta minus* (β^-) when a neutron turns into a proton, an electron (e^-) and an electron antineutrino ($\bar{\nu}_{e^-}$) e.g.: ${}^{210}_{81}Tl \rightarrow {}^{210}_{82}Pb + e^- + \bar{\nu}_{e^-}$ (Blin-Stoyle, 1991).
- *Beta plus* (β^+) when a proton turns into neutron, a positron, and an electron neutrino (Blin-Stoyle, 1991), e.g.: ${}^{234}_{90}Th \rightarrow {}^{234}_{91}Pa + e^+ + \nu_{e^-}$.
- *Electron capture* when a proton plus an electron forms a neutron plus an electron neutrino, e.g.: ${}^{40}_{19}K + e^- \rightarrow {}^{40}_{20}Ca + \nu_{e^-}$(Schaefer, 2016).

2.1.3. Gamma decay

Gamma decay generally occurs when an exited nuclei lose energy in the transition to a lower energy level emitting radiation in form of a gamma photon, which is electrically neutral (Lilley, 2001). This process undergoes along with alpha and beta decay. Gamma decay lifetime is very short, typically less that 10^{-9} s (Lilley, 2001)

2.2. Sources of natural radioactivity

There are two types of natural ionizing radiation; cosmic radiation that includes cosmic rays (directly ionizing cosmic radiation, photon and neutron) and cosmogenic radionuclides and terrestrial radiation coming from terrestrial radionuclides (^{40}K, ^{87}Rb, ^{238}U series, ^{232}Th series) (UNSCEAR, 2008). Terrestrial radiation is classified from the radiation exposure point of view as follows; external terrestrial exposure that corresponds to gamma radiation, and internal exposure that can be by inhalation and ingestion. The principal contributors for internal exposure by inhalation are ^{222}Rn (radon) and ^{220}Rn (thoron) and in minor proportion uranium and thorium series (mainly radon progenies in air). Whereas, the internal exposure by ingestion mainly corresponds to ^{40}K and in minor proportion to uranium, thorium, radium and lead in water (uranium and thorium series) (Figure 1) (UNSCEAR, 2008).

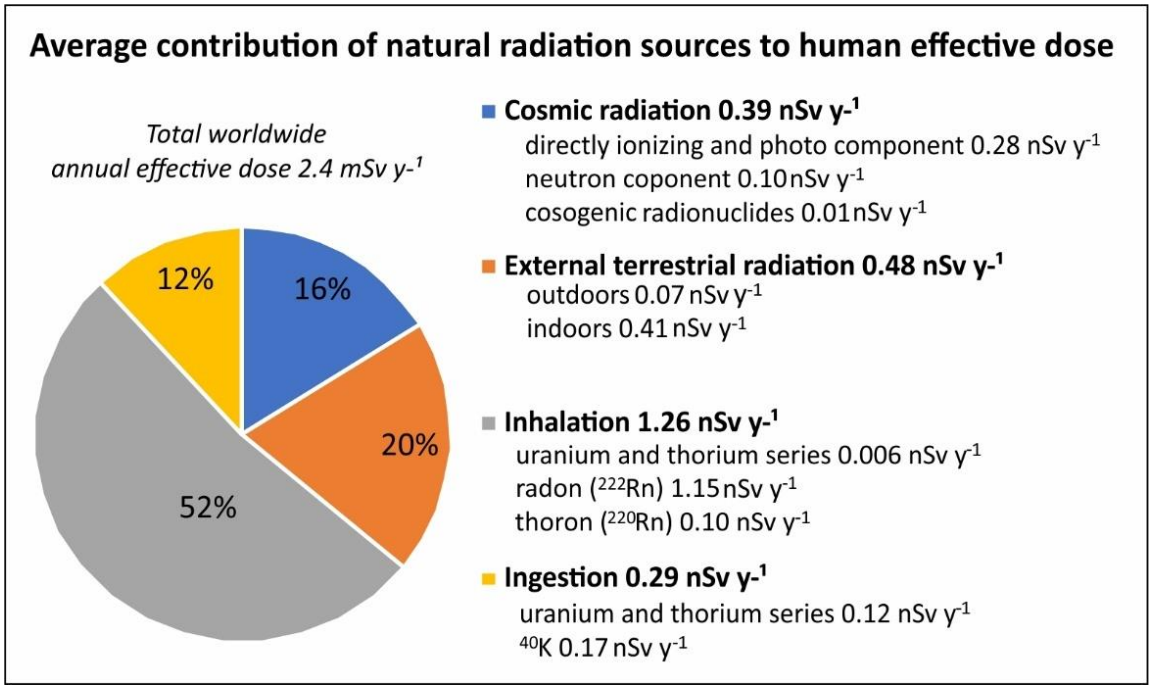

Figure 1. Average contribution of natural radiation sources to the worldwide annual effective dose.

Source: UNSCEAR, 2008

2.3. Main terrestrial natural radionuclides

Before detailing the properties of the terrestrial radionuclides, it is important to define general concepts that will be applied along this document, such as activity, activity concentration, radioactive equilibrium and secular equilibrium.

The decay rate of a radioactive isotope is expressed by the *activity* and its unit is Becquerel (Bq) that is equal to 1 s^{-1} and the *activity concentration* represents the number of disintegrations per second and per unit of volume (Bq m^{-3}) (Cothern and Smith, 1987). When the activity of the progeny is equal to the one corresponding to its parent the *radioactive equilibrium* is established. However, considering particularly the nature of radon, it is unlikely to reach complete equilibrium. The *secular equilibrium* is that situation when a radioactive parent has significantly larger half-life compared to its progeny. Thus the quantity of a radioactive isotope remains constant because its production rate (e.g., due to decay of a parent isotope) is equal to its decay rate (Cothern and Smith, 1987).

The most important natural radionuclides from the point of view of natural ionization exposures are (Figure 1): ^{222}Rn, ^{220}Rn, ^{238}U and ^{232}Th and decay chain isotopes (Figure 2), and ^{40}K a non-forming chain radioactive isotope (Table 1).

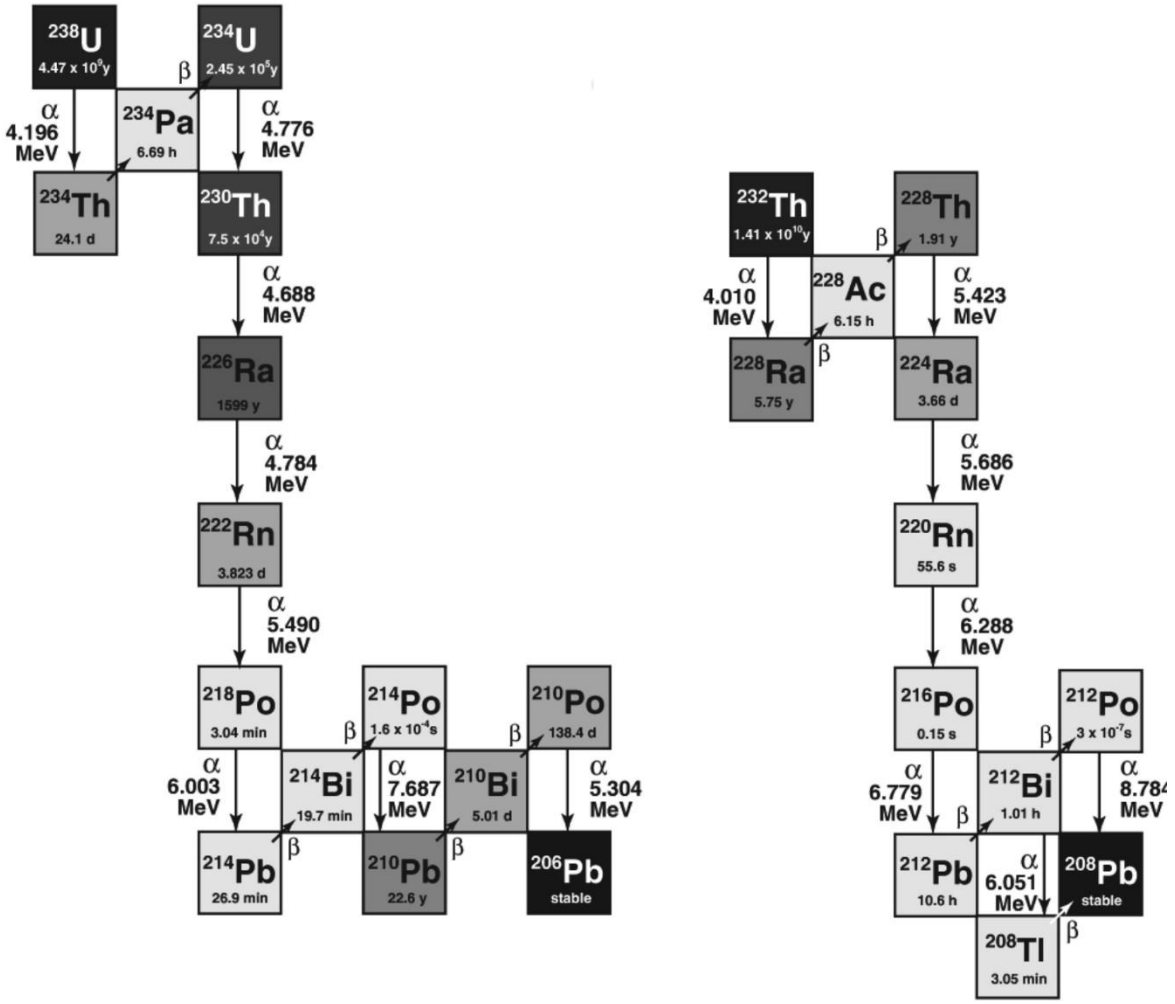

Figure 2. Natural decay series of ^{238}U and ^{232}Th. Half-life type of decay and alpha energies are shown. Grayscale reflects half-life, with darker greys for longer half-lives.
Source: Bourdon et al., 2003

General geochemistry of the relevant natural terrestrial radionuclides from the point of view of human exposure, is summarized in the Table 1 and the specific geochemical behavior of their corresponding elements is detailed below.

Table 1. General geochemistry of ^{238}U, ^{232}Th, ^{226}Ra and ^{40}K

Radio-nuclide	**Half-life**	**Isotopic abundance (%)**	**Oxidation states**	**Activity concentration in Hungarian soils** (UNSCEAR, 2000)	**Main minerals**
^{238}U	4.47 billon years	99.27 %	4+*, 6+* 3+**,5+**	29 Bq kg^{-1}	**Major minerals:** uraninite (UO_2), coffinite ($USiO_4$), brannerite ((U, Ca, Ce)(Ti, Fe)$_2O_6$) and carnotite ($K_2(UO_2)2(VO_4)_2$ $3H_2O$). **Accessory minerals (resistants):** Zircon ($Zr(SiO_4)$), apatite ($Ca_5(PO_4)_3(F, Cl, OH)$), monazite ($(Ce, La)PO_4$), xenotime ($Y(PO_4)$), allanite {CaCe}{Al2Fe^{2+}}($Si2O_7$)(SiO_4)O(OH).
^{232}Th	14 billon years	100 %,	4+*, 3+**	28 Bq kg^{-1}	thorianite (ThO_2), thorite ($ThSiO_4$), monazite ((Ce, La, Nd, Th)(PO4,SiO_4))
^{226}Ra	1600 years	Trace	2+	33 Bq kg^{-1}	radiobarite ($RaSO_4$), uranium and thorium minerals
^{40}K	1.25 billion years	0.0117 %	1+	370 Bq kg^{-1}	clay minerals (illite group), micas and K-feldspar
^{222}Rn	3.823 days	-	-	-	radium minerals
^{220}Rn	55.6 s	-	-	-	radium minerals

***** stable in natural settings, ** rare and unstable. Source: (Bourdon et al., 2003; UNSCEAR, 2000)

2.3.1. Geochemical behavior of potassium

Potassium is a major constituent element in the earth crust. The cations of potassium (K^+) are very soluble and its mobility depends on the incorporation into the lattice of clay minerals (illite group), its absorption capacity is much higher than that corresponding to Na^+ (Barton and Karathanasis, 2002). The natural isotopes of potassium are non-radioactive except ^{40}K. The 89.1 % of ^{40}K decays to ^{40}Ca via beta decay and the remaining 10.9 % produce ^{40}Ar via electron capture (Schaefer, 2016).

2.3.2. Geochemical behavior of uranium

Uranium, a lithophile and incompatible element, belongs to the actinidines group and share similar chemical behavior with them, especially due to the similar electronic configuration of the outer shell (orbitals 7s, 6d and 5f). In reducing conditions U^{4+}, forms an insoluble and considered immobile compound known as uraninite (UO_2). Such a uranium reduction can be caused by biological activity (Bourdon et al., 2003) or by high phosphate concentration at acidic pH value (< 5). Whereas, in oxidizing conditions U^{6+} forms uranyl ion $(UO_2)^{2+}$, which tends to form compounds that are soluble in water, allowing the mobility of uranium. This means that uranium is often mobile in oxidizing conditions and separates from thorium, which exists only in the tetravalent state and whose compounds are generally insoluble in water (Faure and Mensing, 2005). At acidic conditions (pH < 7) it is adsorbed into Fe^{3+}-oxides and -hydroxides (e.g. hematite, goethite) and clay minerals specially montmorillonite because of lamellar structure. Also, uranyl forms complexes with organic material. In the range of pH 4-8 forms complexes with phosphates. At alkaline conditions (pH > 7) forms complexes with carbonates such as uranyl carbonate (Bourdon et al., 2003). The most abundant isotope of uranium is ^{238}U (Table 1), which is the parent nuclide (Figure 2) of the so-called *uranium series*.

2.3.3. Geochemical behavior of thorium

Thorium is a lithophile incompatible element. Thorium only exists as Th^{+4} in the nature forming thorianite (ThO_2), which is generally insoluble in water. However, Th^{4+} is soluble

when it is hydrolyzed, allowing its mobility in a wide range of pH. At pH between 5 and 8, Th^{4+} hydrated ion has the maximum absorption into organic matter, clay minerals, Fe^{3+}-oxides, hydrous Mn-oxides and Zr-, V-, Ti-hydroxides. The mobility of Th in soil can increase by organic acids and limited or stopped by adsorption on clay minerals and organic matter. At pH < 3, Th^{4+} is soluble in sulfate compounds (Bourdon et al., 2003). The parent radionuclide of the *thorium* series (Figure 2) in 232Th which is the most abundant isotope of thorium (Table 1). It has a longer half-life and it is more abundant than ^{238}U (Table 1).

2.3.4. Geochemical behavior of radium

Radium belongs to the alkaline earth metals group with Sr, Mg, Ca and Ba. In nature, alkaline earth metals do not exist in their elemental state only in compounds as 2+ ions, due to its reactivity. Radium has similar behavior to barium because the similarity of their ionic radius (r_{Ra}=1.52 x10^{-8} cm , r_{Ba}=1.52 x10^{-8} cm) (IAEA, 2014), thus, barium is commonly used for predicting the behavior of radium. Radium can be found in soil as mineral such as radiobarite ($RaSO_4$) and precipitated on the surface of soil particles. The proportion of these forms is highly dependent on the rock material, weather conditions and permeability of the soil. During the weathering process, radium is removed from the primary mineral and adsorbed into the soil particles. Since the specific surface area increases with decreasing particle size, the relative enrichment of radium also increases with the reduction in particle size (Faure and Mensing, 2005). The adsorption of radium is function of pH, and the range of pH when the radium adsorption starts depends on the point of zero charge (PZC) of the mineral when the electrical charge is zero above this the mineral surface has a negative net charge and strongly adsorbs cations(EPA, 2004). Radium as cation, competes for adsorption sites in soil systems with other alkaline earth cations. At pH ≥ 7 radium is ready adsorbed on clays and mineral oxides. Nathwani and Phillips (1979a) studied the absorption of radium in soil and determined that organic material and clay has strong affinity for radium mainly because of their cation exchange capacity, and they observed that organic material absorbs ten times more radium as clay (Nathwani and Phillips, 1979a). Radium is one of the most strongly adsorbed on clay minerals, by ion exchange, in comparison to other alkaline earth elements, in the following order of preference: $Ra^{2+} > Ba^{2+} > Sr^{2+} > Ca^{2+} > Mg^{2+}$ (Sposito, 2008). In a

second study Nathwani and Phillips (1979b) found that at high concentration of calcium anions, the adsorption in soil is more determined its maximum adsorption capacity than the affinity for radium (Nathwani and Phillips, 1979b). Under the opposite conditions, high calcium concentrations in soil and low organic material and clay increases radium mobility (Thorne and Mitchell, 2011). According to study of Greeman and Rose (1996), it was demonstrated that the organic component makes the largest single contribution for soil gas radon emanation in soil gas, and determination of the radon emanation coefficient of minerals coated by organic material (0.46) is higher than the clays (0.22). Radium (^{224}Ra and ^{226}Ra) decays to radon (^{222}Rn and ^{220}Rn, respectively) emitting an alpha particle (Figure 2).

2.3.5. Geochemical behavior of radon

Radon is a colorless, odorless, tasteless noble gas. At standard temperature and pressure, radon forms a monatomic gas with a density of 9.73 kg m^{-3}, about 8 times the density of the earth atmosphere at sea level, 1.217 kg m^{-3}. Radon is one of the densest gases at room temperature and is the densest one of the noble gases. It is inert to most common chemical reactions, such as combustion, because the outer valence shell contains eight electrons. This produces a stable, minimum energy configuration, in which the outer electrons are tightly bound. It is sparingly soluble in water, but more soluble than lighter noble gases. It is the radioactive progeny of radium; therefore, it is highly influenced by the environmental conditions in which radium is creating. Although radon is intrinsically non-reactive, it is generally produced as individual isolated atoms rather than bulk gas. These atoms can be trapped by the environmental matrix, in which they arise. This trapping process can be highly efficient if the atoms are produced deep within the rock matrix. The recoil energy originated in radium, decay process can either help radon to be liberated or embed deeper into the grain (Faure and Mensing, 2005). From the health risk assessment point of view, the most relevant radioactive isotopes of radon are ^{222}Rn commonly called *radon* and ^{220}Rn called *thoron* (Figure 1) which are the main contributors to the internal exposure of natural radiation. Their general characteristics are summarized in Table 1. For ^{222}Rn, the typical recoil distance range are between values of 0.02-0.07 μm in minerals, 0.1 μm in water and 63 μm in air; the range of ^{220}Rn in air is 83 μm (Tanner, 1980).

2.3.6. Geochemical behavior of short-lived progenies of radon

According to Figure 2, short-lived progenies for ^{222}Rn are: ^{218}Po, ^{214}Pb, ^{214}Bi, and ^{214}Po and for ^{220}Rn are: ^{216}Po, ^{212}Pb, ^{212}Bi, ^{208}Tl and ^{212}Po. If they are produced in solid or liquid phase, they cannot migrate far and are considered in secular equilibrium with the parent radionuclide (Faure and Mensing, 2005).

2.4. Granitic soil and rock as a geogenic source of natural radioactivity

The geogenic sources of radon in granite can be explained at different scales. Firstly at macroscopic level, the elevated of uranium concentration in igneous acidic rock as granite (4.7 ppm in average), is explained by its low melting point (compared with basalt) that during the heating (hydrothermal, magmatic process), it is part of the volatile phase where uranium is enriched (Cothern and Smith, 1987). Secondly, at mesoscopic scale, the redistribution of uranium due to its geochemical behavior linked to the soil and rock characteristics and process such as weathering and alteration, influences directly the distribution of radium and consequently the radon emanation (Bourdon et al., 2003; Cothern and Smith, 1987).

Finally, at microscopic scale, besides the radium distribution in the grain directly related with radon emanation, the nature of the mineral plays and important role. It is estimated that up to one third of the radon can be directed released to the pore space from interstitial oxides. However, about 30 to 70 % of the uranium in granites is locked up in minerals such as monazite and zircon that are resistant to the weathering process called resistants. Uranium-bearing minerals such as uraninite, apatite and monazite have emanation coefficients in the range of 0.005 to 0.25. Whereas, zircons crystals has low emanation coefficients in the range of $1x10^{-5}$ to $1x10^{-5}$ (Cothern and Smith, 1987). In weathered soil and rocks, uranium and thorium released from the disintegration of other minerals and are adsorbed onto the surface of clay particles. Uranium rand radium in solution can coprecipitate with iron oxides and being deposited in fractures and pore spaces (Cothern and Smith, 1987). This surface sorption has been proved by (Barretto, 1973) through a study in two type of soil derived from weathering of granites, that the concentrations of uranium series isotopes (^{238}U, ^{232}Th, ^{226}Ra and ^{210}Pb) increases as the grain sized decreases below 0.1 mm (Cothern and Smith, 1987). However, it must be considered the influence of pH in the redistribution.

3. Ambient gamma dose equivalent rate

The most common field measured quantity of natural background radiation is the ambient dose equivalent rate, H*(10), in units of miliSievert per hour (mSv h^{-1}), which is a measurable equivalent of the above mentioned effective dose, quantifying the risk to human health associated with the radiation exposure (ICRU-51, 1993). The measured ambient gamma dose equivalent rate, H*(10) consists of several artificial and natural components, e.g. artificial: ^{137}Cs, natural: terrestrial ^{222}Rn, cosmic ^{14}C , however there are proposed algorithm decomposition methods to distinguish the natural terrestrial component (Bossew et al., 2017). Terrestrial gamma dose rate can be applied to predict the radon flux or geogenic radon potential (Bossew et al., 2015; Cinelli et al., 2015; Manohar et al., 2013; Szegvary et al., 2007). Quindós et al. (2008) tested the applicability of gamma dose rate for prediction indoor radon levels in a granitic region in Spain. They concluded that gamma dose rate is a qualitative indicator of high indoor radon level rather than a good quantitative predictor. External gamma dose rate has been proved to discriminate non-radon-prone municipalities by García-Talavera et al. (2013) based on the evaluation of 14 different lithographic units. Basic spatial analysis methods (i.e. ordinary and universal kriging) are frequently applied for natural radioactivity data (for instance, gamma-radiation), which is commonly related to the geological background using statistical methods (García-Talavera et al., 2013; Hiemstra et al., 2009; Manohar et al., 2013; Ramli et al., 2001; Sanusi et al., 2014; Yeşilkanat et al., 2015). Advanced spatial analysis (i.e. digital image processing) revealed spatial relationship between soil gas radon activity concentration, geogenic radon potential and ambient dose rate, and geological and geomorphological features (Borgoni et al., 2011; Branion-Calles et al., 2015; Pásztor et al., 2016; Szabó et al., 2017, 2014). In these studies, main spatial features, identified in the soil gas radon activity concentration, geogenic radon potential and ambient dose rate are influenced by the underlying geological structures and surface sediment distribution defined by morphological conditions in the study area.

4. Radon availability and migration in soil

It is important to clarify that radon, as a non-reactive noble gas, does not represent a hazard for human health directly. However, its danger relies on the fact that it can migrate through the soil and reach the ambient air, making possible the contact of his progenies with the human tissues by inhalation (Nazaroff, 1992).

For better understanding the factors that can either directly or indirectly influence the soil gas radon concentration, it is important to define the processes involved in the availability and migration of radon in soil, as schematized in Figure 3. Nazaroff (1992) have classified them in two clusters: radon availability and radon migration. The first one complies the influencing factors of soil gas radon concentration in steady state conditions, whereas the second one encompasses the factors influencing the movement of radon towards the ambient air (Nazaroff, 1992).

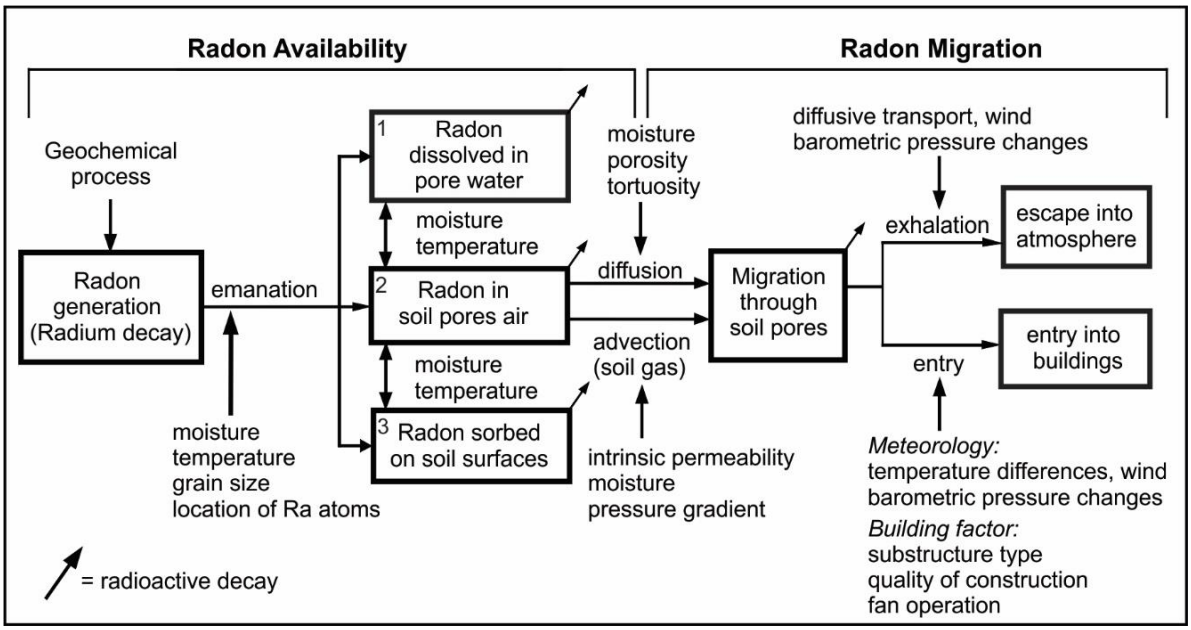

Figure 3. Schematic representation of radon production and migration in soil.
Source: (Nazaroff, 1992)

In Figure 3, the boxes represent the major steps by which radium in soil contributes to airborne radon. Horizontal arrows are labelled with names of the processes by which transition occurs. Labels on vertical arrows indicate the parameters that significantly

influence the rate of progress from one state to another. The diagonal arrows denote radon loss by radioactive decay (Nazaroff, 1992).

4.1. Radon availability in soil

4.1.1. Radium distribution

Radon is the radioactive progeny of radium (Figure 2), thus the distribution of the last one in the soil depends on geochemical process and its behavior detailed in the section 2.3.4.

4.1.2. Radon emanation

Only a fraction of the produced radon can leave the solid state and reach the soil pores through a process called emanation (Nazaroff, 1992). Considering the location of the radium atom and the recoil distance, this process has three possibilities (Figure 3): 1) the resulting radon atom may be released on the pore space and dissolved in the water contained in the pore space, 2) the radon released in the pore space can be incorporated in gas phase (soil air) and 3) it can remain in the solid phase by being embedded in the grain or travel across the pore space and get implanted into the neighbor grain. The radon in the soil air migrates by diffusion, the distance depends on the media and the radon diffusion coefficient in the media, as it is shown in Table 2.

Table 2. Radon diffusion coefficients and diffusion length for various material

Materials	Diffusion coefficient ($m^2 s^{-1}$)	Diffusion length (m)	Reference
air	$1.2x10^{-5}$	2.4	Hirst and Harrison, 1939
water	$1.0x10^{-9}$	0.022	Durrani and Ilic, 1997
sand	$3.4x10^{-6}$	1.3	R.P. Chauhan et al., 2008
silty/sandy soil	$2.7x10^{-6}$	-	R.P. Chauhan et al., 2008
clayey soil	$8.0x10^{-11}$ - 62 $x10^{-11}$	0.006-0.017	Hansen and Damkjaer, 1987
concrete	$2x10^{-5}$	0.04 - 0.026	Folkerts et al., 1984

The distribution of radon in air (C_{air}) and water (C_{water}) is quantified by the partition coefficient (k) that is function of the temperature (in Celsius degree) and can be calculated with the Eq. 1, developed by Weigel (1978):

$$k = \frac{C_{water}}{C_{air}} = 0.105 + 0.405e^{-0.0502T\ (°C)} \quad \text{Eq. 1}$$

Since the emanation is the principal process in radon availability, its influencing factors are detailed bellow.

4.1.3. Factors influencing radon emanation

Radium distribution

Since radium is removed from the primary minerals and adsorbed into soil particles, during the weathering process, it is likely to be concentrated over the surface of the grains. Therefore, it can be shown that the radium concentration increases as the specific surface increases at smaller particle size. Consequently, the emanation coefficient increases with the increasing radium concentration into the surface of the grain (Faure and Mensing, 2005; Hassan et al., 2009; Morawska and Phillips, 1993; Nazaroff, 1992).

Water content in the pore space

If there is water present on the surface of the grains in the pore space, the released radon can get stopped in the liquid phase due to the difference between the orders of magnitude of the diffusion length in air and water (Table 2) that causes an increment of the emanation coefficient. However, if the pores are filled with water, under water saturated conditions, radon is stopped in the liquid phase maintaining constant the emanation (Bossew, 2003; Hassan et al., 2009; Markkanen and Arveka, 1992; Morawska and Phillips, 1993; Shweikani et al., 1995; Straden et al., 1984). The water saturation depends not only of the water content but also of the total porosity of the material.

Grain size

When the particle size decreases, the specific surface area increases as well as the atoms of radon that can be released directly to the pores by recoil that means an increment of radon emanation (Hassan et al., 2009; Markkanen and Arveka, 1992). This effect on emanation was quantified by Morawska and Phillips (1993), who found that the emanation coefficient

decreases from both 40 and 20 % to 2 % when the radius of the grain size increases from 0.5 and 1 to 8 μm, respectively.

Temperature

With an increase of temperature, the adsorption of radon on solid grains decreases significantly, which results in a increment of radon emanation (Morawska and Phillips, 1993). This effect of temperature on the emanation coefficient was found by Barreto (1973) in a granite sample where it decreases from 0.106 at 265 °C to 0.081 at -20 °C. Hence, the impact of temperature changes in soils is minor considering the temperature ranges of common soils (Nazaroff, 1992).

4.2. Radon migration in soil air

There are two mechanisms for radon migration in soils: *diffusion* and *convection*. The diffusive transport is considered as random molecular motion from environments of high radon concentration to the low concentration ones (Nazaroff, 1992). This process is the dominant in radon migration and it is described by Fick's second law expressed in terms of radon flux density (I in Bq m^{-2} s^{-1}) in direction of z (depth in meters), the vertical distance (positive downwards) that is shown in the following differential equation (Eq. 2) (Porstendorfer, 1994):

$$I = -D_e \frac{dC}{dz} \qquad \text{Eq. 2}$$

where, D_e is the effective diffusion coefficient (m^2 s^{-1}) and C (Bq m^{-3}) is the radon concentration in the pore space (Porstendorfer, 1994). The radon effective diffusion coefficient in soil can be calculated by multiplying the bulk diffusion coefficient (D) of radon in an specific media (Table 2) by the effective porosity of the soil ($D_e = D \cdot p_e$).

On the other hand, the convective transport considers the radon transport only by the movement of the pore-filling-fluid, generally driven by gradient pressure originated by changes of meteorological conditions. This process can be described by Darcy's law that

relates the flow rate per unit of cross-sectional area (v *in* m s^{-1}) to the gradient pressure (Eq. 3) (Porstendorfer, 1994):

$$v = -\frac{K}{\mu}\frac{dC}{dz} \quad \text{Eq. 3}$$

where, K is the soil permeability and (m^2), μ the dynamic viscosity of the fluid (air) (kg m^{-1} s^{-1}). If the flux density $I = v \cdot C$, then the total flux equation for radon in the soil is expressed as in Eq. 4 (Porstendorfer, 1994):

$$I = D_e \frac{dC}{dz} + v \cdot C \quad \text{Eq. 4}$$

Considering the following processes: radon diffusion, convection, continuous radon radioactive decay (represented by the multiplication od the radon decay constant λ in s^{-1} and the soil gas radon concentration C) and generation (G in Bq m^{-3} s^{-1}), radon concentration profile in soil can be expressed by Eq. 5 (Nazaroff and Nero, 1988; Porstendorfer, 1994):

$$\frac{D_e}{p_e}\left(\frac{d^2C}{dz^2}\right) - \frac{1}{p_e}\frac{d(vC)}{dz} - \lambda \cdot C + G = 0 \quad \text{Eq. 5}$$

Eq. 5 has some implicit assumptions, such as, the radon migration is driven by the concentration gradient, the migration in this case is assumed to be homogeneous and the diffusion coefficient constant, finally the radon concentration fraction in the water phase of the pore space is neglected (Nazaroff, 1992; Nazaroff and Nero, 1988; Porstendorfer, 1994; Várhegyi et al., 2013).

4.2.1. Influencing factors on diffusion coefficient

Water content

The radon diffusion in the pore space decreases with the increment of water content in the pore space because of the difference in the diffusion coefficient of radon in water and air ($D_w = 1x10^{-5}$$m^2$ s^{-1} and $D_a = 1.2x10^{-2}$ m^2 s^{-1}, respectively) (Cothern and Smith, 1987; Durrani and Ilic, 1997; Hassan et al., 2009; Hirst and Harrison, 1939; Hosoda et al., 2009).

Grain size

Chauhan et al. (2008) found that radon diffusion coefficient increases with the diminution of the soil and sand size.

4.3. Soil gas permeability

Permeability is defined as the capacity to transmit a fluid. It depends on the volume of pores as well as the extend of its interconnection (Nazaroff, 1992). It is an important factor in the radon migration process because it determines how the fluid will migrate in the soil. This parameter varies in a wide range according to the soil type, as it shown in Figure 4. At lower permeability ranges of Figure 4, radon transport is dominated by molecular diffusion, whereas at upper end of the range, advection is the dominant mechanism Nazaroff (1992). The microscopic characteristics of the soil: size, shape, number and orientation of pores and the moisture content, determines the permeability. Being the strongly influenced by soil moisture and grain size (Nazaroff, 1992).

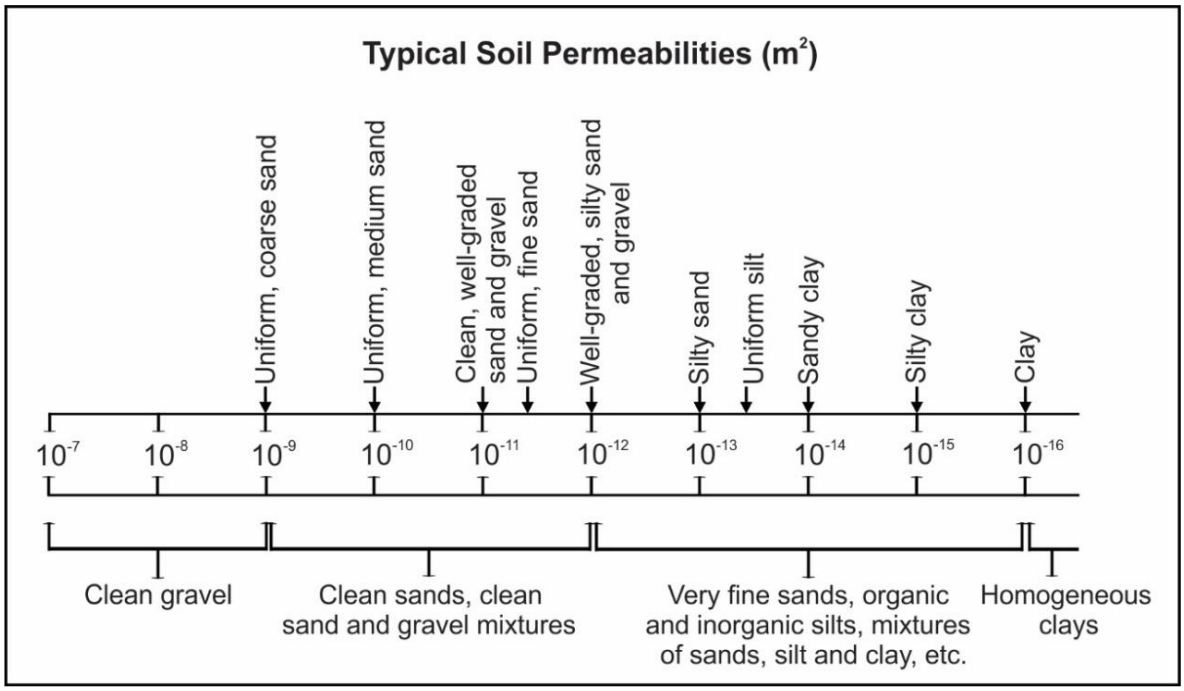

Figure 4. Typical soil permeabilities of different soil textures.
Source: Nazaroff (1992).

In sheared and fractured rock permeability is meaningful, due to the transport of radon from significant depths to the surface. Since uranium is located preferentially in the fractures, the bed rock can contribute significantly to enhance the radon concentration.

4.3.1. Empirical model for estimating soil air permeability

Rogers and Nielson (1991) developed an empirical relationship (Eq. 6) for the estimation of soil gas permeability using 137 field measurements, based on volume fraction of water saturation, total porosity and arithmetic mean diameter:

$$\boldsymbol{MP1}\text{: } K = \left(\frac{p_t}{500}\right)^2 {d_a}^{4/3} \exp(-12s^4) \qquad \text{Eq. 6}$$

K: soil gas permeability (m^2)

p_t: total porosity

s: volume fraction of water saturation

d_a: arithmetic mean particle diameter, excluding +#4 mesh (m)

The model of Eq. 6 is called MP1 (model permeability 1) for practical reasons. The applied instrument was a soil gas permeability sampler Model MK-II, (Nielson et al., 1989). Undisturbed soils and fill materials in Utah Wasatch Front and Florida area were measured and soil density samples at 0.6 m depth where collected following the ASTM drive-cylinder protocol (ASTM D-2937-83). After determining field densities and water contents (ASTM D-2216-80), the samples were subjected to particle size analyses (ASTM D-422-63) that included dry sieving from 4.75 mm (mesh #4) to 75 μm (mesh #20) and the fraction smaller than this was determined by a sedimentation process using a hydrometer (Rogers and Nielson, 1991a).

Figure 5 shows the correlation plot obtained by Rogers and Nielson (1991a) applying their empirical model based on field measurements of Utah and Florida soils. For practical reasons, in the present thesis, this model will be noted as MP1.

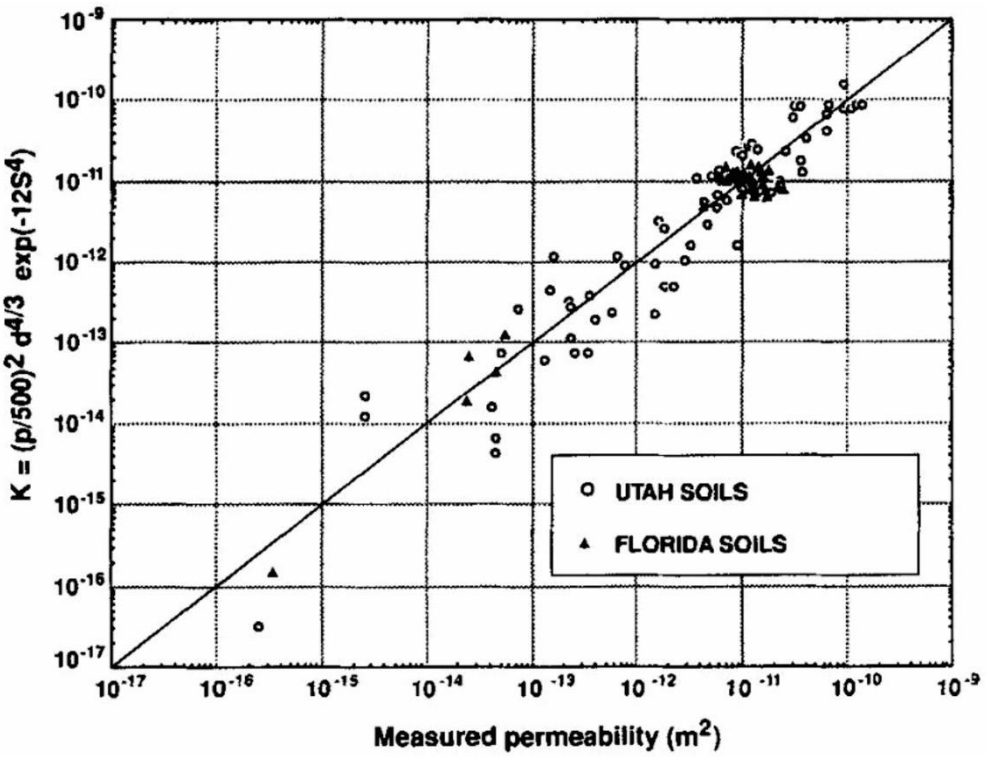

Figure 5. Results obtained by Rogers and Nielson (1991a) showing the correlation between the field measured and predicted soil gas permeability applying their empirical equation. Source: (Rogers and Nielson, 1991a)

4.4. Equilibrium radon concentration in soil air

Equilibrium or saturation concentration is defined as the maximal radon concentration in the soil air (C_∞ in Bq m^{-3}) at large depth ($z \to \infty$). Eq. 5, the term G, related to the generation rate of radon can be expressed in terms of C_∞ as in Eq. 7:

$$C_\infty = \frac{G}{\lambda} \qquad \text{Eq. 7}$$

The maximal radon concentration generated in the pore space within the radioactive equilibrium of radon concentration can be directly measured in situ. Alternatively, from the analytical solution of Eq. 3, considering that the radon concentration in the surface is zero ($C_{z=0} = 0$ Bq m^{-3}), different theoretical models involve soil physical characteristics and radioactive content have been proposed.

4.4.1. Theoretical models for the estimation of equilibrium soil gas radon concentration

4.4.1.1. Model proposed by Porstendorfer (1994)

The first relationship developed to model the equilibrium soil gas radon concentration was proposed by Porstendorfer (1994). This model assumes homogeneity in radium content, emanation coefficient, porosity and permeability of the soil, additionally the radon concentration in the water phase of the pore space is neglected (Nazaroff, 1992). The expression proposed by Porstendorfer (1994) is shown below (Eq. 8). Within this document this expression is noted as MR1 (model radon 1) for practical reasons:

$$\boldsymbol{MR1}: \boldsymbol{C_{\infty}} = \frac{\boldsymbol{C_{Ra}\varepsilon\rho_{bulk\ dry}}}{\boldsymbol{p_e}} \qquad \text{Eq. 8}$$

C_{∞}: maximal radon concentration in soil air at large depth available for transport (Bq m^{-3})

C_{Ra}: radium activity mass concentration of the material (Bq kg^{-1})

ε: emanation coefficient (dimensionless),

$\rho_{bulk\ dry}$: bulk density (kg m^{-3})

p_e: effective porosity

This relationship has been widely applied in its original form and with slight variations (Chitra et al., 2018; Cosma et al., 2001; Ielsch et al., 2002; Ishimori et al., 2013; Jiang et al., 2011; Moldrup et al., 1998; Nazaroff and Nero, 1988; Pereira et al., 2017; Petersell et al., 2015; Washington and Rose, 1992; Yakovleva, 2005).

4.4.1.2. Model proposed by Várhegyi et al. (2013)

In a recent study, Várhegyi et al. (2013) present a modification of the original model MR1 by adding a factor that considers the radon concentration in the water phase of the pore space. This model proposes a one-dimensional stationary model of radon transport for single cover layer of uranium mining and ore processing (Várhegyi et al. 2013). This expression is noted as MR2 (model radon 2) for practical reasons:

$$\boldsymbol{MR2}: \boldsymbol{C_{\infty}} = \frac{\boldsymbol{C_{Ra}\varepsilon\rho_{bulk\,wet}}}{\boldsymbol{p_e(w_m+1)-\left(\frac{\rho_{bulk\,wet}}{\rho_{water}}\right)w_m(1-k)}} \quad \text{Eq. 9}$$

$\rho_{bulk\,wet}$: wet bulk density (kg m^{-3})

ρ_{water} : water density (kg m^{-3})

w_m: is the water content in units of mass (gravimetric water content)

MR2 considers a three-phase system (soil-water-air) by including the partition coefficient (k) (section 4.1). For non-saturated conditions, the resulting expression of equilibrium radon concentration.

4.5. Geogenic radon potential (GRP)

Since the main geogenic source of ^{222}Rn is the soil, it is important to determine the geogenic radon potential (GRP) (Bossew et al., 2013), accounted as the best indicator for radon risk assessment. The quantification of GRP is based on the mathematical expression proposed by Neznal et al. (2004) in Eq. 10, which relates the radon potential with the equilibrium concentration of ^{222}Rn (kBq m^{-3}) in soil air and the soil gas permeability (m^2):

$$\boldsymbol{GRP} = \frac{\boldsymbol{C_{\infty}}}{\boldsymbol{-log_{10}(K)-10}} \quad \text{Eq. 10}$$

Neznal et al. (2004) have established three categories for GRP based on soil gas permeability and soil gas radon concentration, as result of a vast research in this field in Czech Republic that is shown in Table 3.

Table 3 Geogenic radon Potential (GRP) categorization based on soil gas permeability and soil gas radon concentration.

GRP category	**Soil gas radon concentration (kBq m^{-3})**		
Low	$C_{Rn} < 30$	$C_{Rn} < 20$	$C_{Rn} < 10$
Medium	$30 \leq C_{Rn} \leq 100$	$20 \leq C_{Rn} \leq 70$	$10 \leq C_{Rn} \leq 30$
High	$C_{Rn} > 100$	$C_{Rn} > 70$	$C_{Rn} > 30$
	Soil gas permeability (m^2)		
	Low $K < 4x10^{-13}$	Medium $4x10^{-13} \leq K \leq 4x10^{-12}$	High $K > 4x10^{-12}$

Source: (Neznal et al., 2004)

5. Study area

The study area is located in the northwest of Velence Hills, which is about 50 km far from Budapest to the southwest (Figure 6). The study area is dominated by forest, fields and includes the village of Pákozd with approximately 3,000 inhabitants. The topographic elevation varies between 110 and 241 meters above the sea level. The climate is temperate continental with a mean of annual temperature around 10 °C and average of 550-600 mm of annual precipitation (Mezősi, 2015). The geological information for this study is based on the 1:25,000 scale geological map of the Velence Hills complied by Gyalog and Horváth (1999) and its descriptive book (Horváth et al., 2004).

Since the present study involves the evaluation of the ambient dose equivalent rate and the geogenic radon potential as the main contributors to the external and internal exposure, each evaluation was carried out in a different extension within the study area considering the respective applied methodology. The ambient gamma dose rate encompasses the granitic surficial outcrop and its contact with the surrounding formations (Figure 6), whereas the evaluation of the geogenic radon potential was performed in a smaller extension in the center of the outcrop in late Pleistocene, slope deposits (Figure 7).

5.1. Study area for ambient gamma dose equivalent rate evaluation

To characterize a granitic area in terms of ambient gamma dose equivalent rate values and its relationship with geological features, the 19.8 km^2 study area located in the western side of the Velence Hills (Figure 6) was selected. These Hills main mass is made up by the outcropping Velence granite formation that was formed in the Variscan orogeny in the Carboniferous (280-300 Ma). Subaerial redeposited clastic sediments of Neogene with Pannonian age (8.9-5.33 Ma) are found inside and at the edges of the study area (Buda, 1981; Horváth et al., 2004) (Figure 6). Flat areas, valley bottoms and hill slopes are sporadically covered by Pleistocene and Holocene sediments such as loess, sand, proluvial, deluvial and eolic sediments, as well as fluvial and peat deposits (Figure 6). In the granitic outcrop a dike complex was formed in different geological times having a predominant SW-NE strike (Buda, 1981; Horváth et al., 2004).

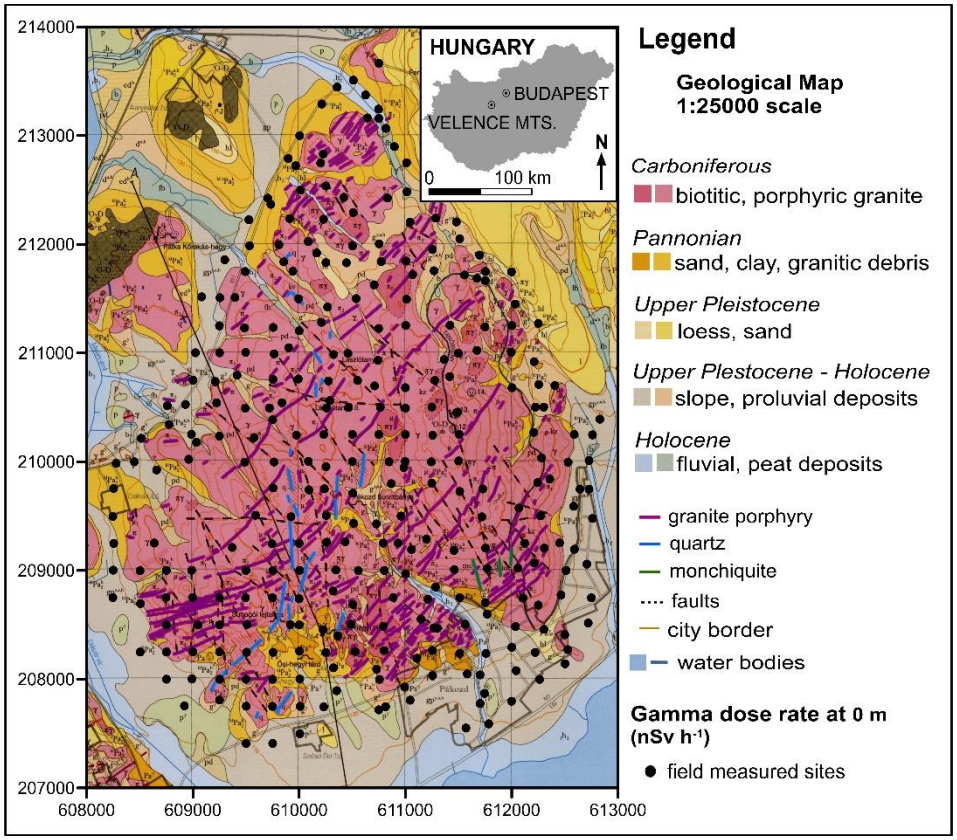

Figure 6. Geological map of the study area of ambient gamma dose rate, overlaid by the fault lines, dikes and measured sites.

Source: Horváth et al. (2004).

Based on the mineralogical composition, three types of dikes can be identified in the study area: granite porphyry, quartz and monchiquite dikes. The first one, the most abundant in the study area, was formed in the late phase of the granite intrusion, showing slight chemical difference compared to granite (Benkó et al., 2014; Horváth et al., 2004). Quartz dikes are originated by a hydrothermal activity, associated also to the granite formation (Benkó et al., 2014; Horváth et al., 2004) and their age is unknown (Horváth et al., 2004). Monchiquite dikes crystallized from a volatile rich mafic melt in the late Cretaceous (Horváth et al., 2004) (Figure 6). Only three 30-70 cm thick mochiquite dikes were mapped in the study area (Gyalog and Horváth, 1999 and Horváth et al., 2004). Such dikes are highly enriched in U (up to 10 ppm) and Th (up to 140 ppm) in the wider region (Szabó et al., 1993), whereas the Velence Hills granite shows a range of 2.5–5.4 ppm for U and 16.9– 23.3 ppm for Th (Burján et al., 2002). According to Horváth et al. (2004) and Benkó et al. (2014), the main orientation of fractures in the granite is SE-NW, perpendicular to granite porphyry dikes orientation, and

they dissect the hills along valleys and streamlets. In contrast, the orientation of the less abundant dikes, quartz and monchiquite is mainly NS (Horváth et al., 2004) (Figure 6).

5.2. Study area for geogenic radon potential evaluation

The 0.8 km^2 study area for the geogenic radon potential evaluation is located in the center of the granitic outcrop (Figure 7). The closest farm is only 180 m southwest far from the study area, whereas the border of Pákozd village only 800 m the study area. The selected area is in a field not affected by anthropogenic intervention. Therefore, the conditions assure the geogenic characteristics of the measurements. It is located entirely in a slope sediment formation that belongs to the late Pleistocene-Holocene transition period (Horváth et al., 2004). This uncovered formation contains contracted slope sediments, angular debris, clay and sand. It is formed by the superficial flushing of the material from the elevated areas by both, deluvial (aerial) and proluvial (linear) process where, generally deluvial process is dominant. These layers are redeposited at the edges of the hills, showing sand-clay talus matrix (Mezősi, 2015).

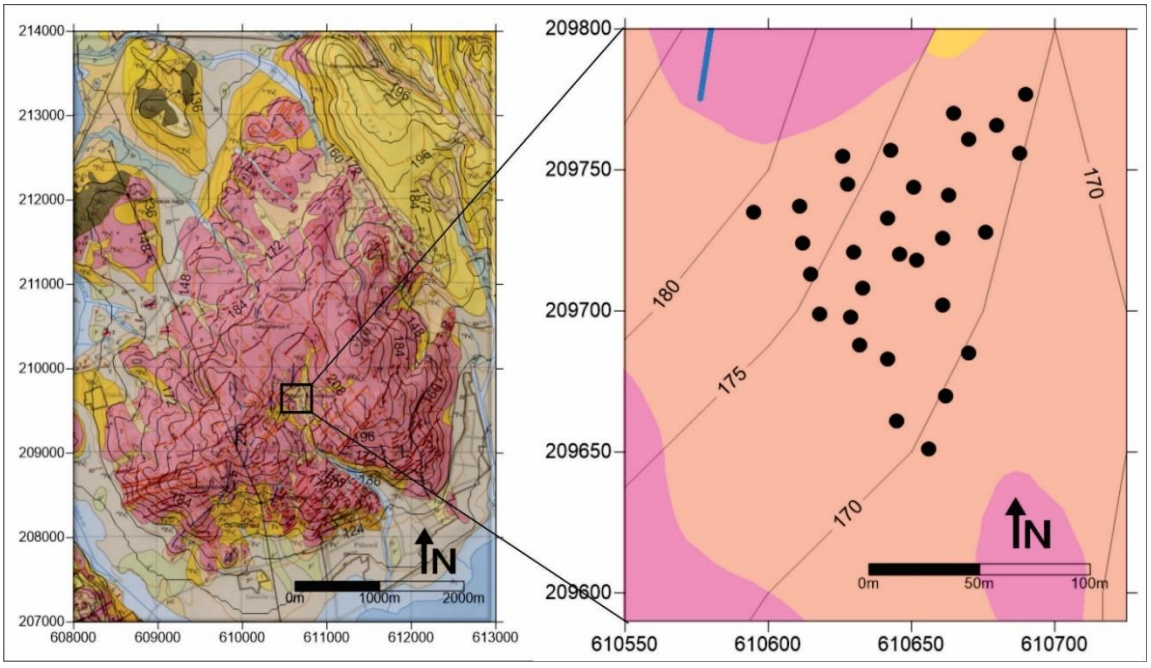

Figure 7. Geological map of the study area of geogenic radon potential, overlaid by the measured sites and the contour lines of altitude. Scale 1:25000
Source: Horváth et al. (2004)

When water enters from bellow to above through the joint system mainly NE-SW oriented, causes hydrothermal and hydrolysis effects of the weathering process, which allows the formation a regolith enriched in clay minerals and colloidal acids (Mezősi, 2015). Water in the area is drained out by Bella creek that goes across Pákozd village and ends in Velence lake. There are two soil types in the northwest of Velence Hills 1) stony soils in the proximity of the top of the hills 2) and the plane surroundings are covered by brown forest soils (cambisols) where forest and agricultural areas can be found (Mezősi, 2015).

6. Methods

6.1. Methods of ambient gamma dose equivalent rate evaluation

The results of the ambient gamma dose equivalent rate evaluation were published in the Journal of Environmental Radioactivity under the topic "Spatial relationship between the field-measured ambient gamma dose equivalent rate and geological conditions in a granitic area, Velence Hills, Hungary: An application of digital spatial analysis methods" (Beltrán Torres et al., 2018). The methodology for the spatial analysis was selected by Dr. Gyozo Jordan and Dr. Attila Petrik, also these coauthors conducted the development and formulation of algorithms. The application of methodology and interpretation of the results was performed in common agreement of the coauthors. This author executed the field measurements, statistical analysis, maps digitalization, generation of results in collaboration of the coauthors. The spatial analysis and its interpretation were performed with the help and advice of Dr. Gyozo Jordan and Dr. Attila Petrik.

6.1.1. Field measurement

Ambient gamma dose equivalent rate (H*(10)) was measured in situ by FH 40 G-L10 instrument (Thermo Fisher Scientific Inc.). Measuring range of the energy filtered proportional counter tube gamma detector is 10 - 100 mSv h^{-1} and its energy range is 30 keV-4.4 MeV. The measurements were performed at the standard heights of 1 m above and on the surface (0 m) (Figure 8). Ambient gamma dose equivalent rate of each site was calculated by averaging 3-6 values recorded each minute. Measurement error was characterized by first calculating the average and standard deviation from the 3-6 measurements for each site that yielded 300 average and standard deviation values.

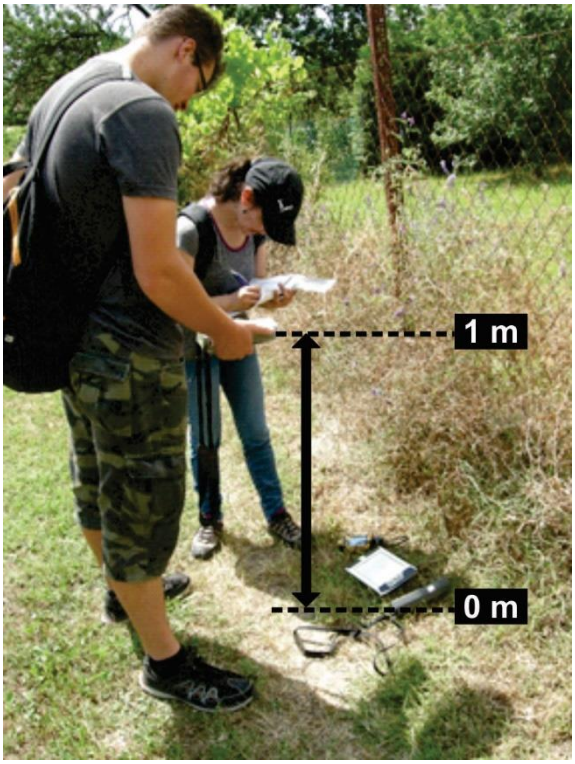

Figure 8. Ambient gamma dose equivalent rate measurements at surface and 1m height.

A grid-based sampling strategy was applied. Ambient gamma dose equivalent rate was measured at 300 sites along a 250×250 m grid over the 19.8 km^2 study area (Figure 6). Inaccessible sites were measured at the closest points. The survey focused on the granite outcrop area (Figure 6): 53 % (160 sites) and 47 % (140 sites) of the measured sites were located on the granite and other formations, respectively (Figure 6). The measurements were carried out during June and July in 2016, under similar field conditions. In addition, temperature, relative humidity and pressure were also measured at each site.

6.1.2. Statistical analysis

Measures of central tendency and variability of the ambient gamma dose equivalent rate used in this study were minimum, average (arithmetic mean), median, maximum, standard deviation, median absolute deviation (MAD) and range. The identification of the outlying values was performed according to the Tukey's (Tukey, 1977) inner fence criteria. Normality of the distributions was tested by the Chi-square test and the Kolmogorov-Smirnov test. The Mann-Whitney (Wilcoxon) homogeneity test was used to compare the median of ambient

gamma dose equivalent rate values measured over various geological rock types and ages (Mann and Whitney, 1947). The linear relationship between the measured ambient gamma dose equivalent rate and the calculated spatial parameters such as dike density in given areas was explored by Bivariate least squares regression analysis. Strength of relationship was expressed by the Pearson's correlation coefficient r (Rodgers and Nicewander, 1988). Statistical significance of the fitted linear model was tested by the F-test and its associated P-value (p). P-value less than 0.05 (since operating at the 5% significance level) indicates that a significant relationship of the form specified exists between Y and X. All the statistical tests applied in this study were significant at the 95 % confidence level.

6.1.3. Mapping and spatial analysis

Field measured ambient gamma dose equivalent rates were interpolated using the triangular irregular network (TIN) interpolation method. This TIN method is an accurate, linear interpolator honoring the original measurement values and does not require preliminary structural analysis unlike kriging for example (Guibas and Stolfi, 1985). TIN represents the modelled surface well, especially in the case of regularly located data points (Davis, 2011). The grid size (10×10 m) was determined by the shortest distance between measurement points. TIN interpolated ambient gamma dose equivalent rates map was smoothed with a low-pass moving average filter of increasing window sizes (5×5, 7×7, 9×9, 11×11, 13×13, 15×15, 17×17, 19×19) to suppress high frequency noise and enhance large scale spatial pattern. Window size of 17×17 (170×170 m) revealed, by visual inspection, the best spatial trend and pattern without losing much detail. Since the objective of this study is to analyze the main spatial patterns without the small-scale irregularities, the outlier free TIN interpolated ambient gamma dose equivalent rates map was used for digital image processing analysis. Error of interpolation was estimated by calculating the difference between the interpolated surface and the original data points.

A systematic digital image processing methodology is applied to the outlier free TIN interpolated ambient gamma dose equivalent rates map according to Evans (1972) method as extended by Jordan et al. (2005) and Jordan, (2007). This method, originally developed for digital elevation models, proceeds from simple univariate data display and evaluation,

through edge detection and image segmentation, to the multivariate interpretation of results using GIS technology.

Shaded relief models were calculated at an azimuth interval of 45° and constant insolation inclination of 45°. The models used Lambertian reflection method and ten times vertical exaggeration. Hill shading increases the contrast of very subtle intensity variations of an image, much more than contouring or pseudo color representation does (Burrough, 1986; Drury, 1987).

The identification of surface specific points including local maxima (peaks), minima (pits), saddle points (passes), flats and slope breaks is straightforward in digital spatial analysis (Jordan, 2007; Takahashi et al., 1995). Pits and peaks reveal anomalous ambient gamma dose equivalent rates and they were calculated by the simple 'higher than' algorithms (Garbrecht and Martz, 1995). Digital cross-sections were made on the TIN interpolated outlier free ambient gamma dose equivalent rate map in parallel and perpendicular to the orientation of dikes to capture spatial trends. Dike density map was calculated by using total length of all dikes, regardless of their origin, within a predefined circle of 500 m radius in order to highlight possible spatial relationship between ambient gamma dose equivalent rates and dike density. Local variability of ambient gamma dose equivalent rates was generated by two different methods. Relief map was calculated on the outlier free ambient gamma dose equivalent rate data within increasing window sizes (21×21, 41×41, 61×61, 81×81, 101×101, 121×121 and 141×141) by using the range divided by the median value of the ambient gamma dose equivalent rates.

Variability index was calculated by taking the square root of the absolute value of the squared differences between the maximum and minimum of ambient gamma dose equivalent rate within a pre-defined window size (in this study: 21×21, 41×41, 61×61, 81×81, 101×101, 121×121 and 141×141). For both methods, the 101×101 (1010×1010 m) window size proved to be the best to reveal distinct patterns of local variance. Relief and variability index maps were later smoothed with 41×41 (410×410 m) and 31×31 (310×310 m) moving average low pass filters, respectively, to enhance the main spatial pattern of different variability zones. Relief and variability index maps (Figure 18a and b) were overlain by all dikes to see whether high dike density corresponds to high local variability of the ambient gamma dose equivalent rates.

Two dimensional autocorrelogram was used to identify anisotropy present in the spatial ambient gamma dose equivalent rate data. Empirical directional variograms were also calculated in different directions using 30° tolerance angle to reveal anisotropy in the ambient gamma dose equivalent rates.

The interpolated ambient gamma dose equivalent rate map is a continuous surface of bivariate function and can be analyzed for the gradient magnitude ('slope') and gradient direction ('aspect'). These parameters were calculated using the Prewitt-operator, which is an unweighted eight-point numerical differentiation method, for its smoothing effect (Gonzalez and Woods, 1993). These gradient calculations were suitable to identify the largest change of the ambient gamma dose equivalent rates ('slope') and its direction ('aspect') at each grid point. Uniform aspect with high gradient magnitudes along linear features may indicate geological influence on the ambient gamma dose equivalent rates distribution. Profile curvature is the second derivative of ambient gamma dose equivalent rates indicating sudden change in gradient magnitude and identifies inflection lines between convex (negative curvature values) and concave (positive curvature values) areas. Classification of gradient or curvature values was performed by using the 'natural break' histogram slicing method at the inflection points on the cumulative distribution function (CDF). The hence identified classes of the mapped parameters were displayed as homogeneous areas in the classified parameter maps.

Lineaments are displayed as sharp linear edges on shaded relief surface and show sudden changes in the gamma dose rates. The final lineament map is a compilation of the manually digitized lineaments on shaded relief surface maps of ambient gamma dose equivalent rates. Lineament density gives information (Figure 22a) on the local variance of ambient gamma dose equivalent rates and it was calculated by the total length of lineaments within a predefined circle of 500 m radius similar to the dike density map calculation (Figure 17). Length and frequency distribution of lineaments were shown in rose diagrams and compared to those of faults and dikes to see the correlation.

The result maps of digital image processing analysis were compared to geological maps with special emphasis on dikes and faults using GIS overlay. Spatial modelling was performed with Surfer 10, ILWIS 3.8 and ArcGIS 10 applications.

6.2. Methods of geogenic radon potential evaluation

The sampling point selection, the field measurements, the soil sampling and basic laboratory methods based on the plan of the NKFIH, PD115810 project. This author complemented these laboratory methods with the following ones; such as dry sieving and laser diffraction for particle size distribution; porosity and volume fraction of water saturation for soil physics. In addition, in line with the objectives of the research, this author proposed and tested new models for geogenic radon potential evaluation and performed chemical composition measurements as well.

This author executed the field and laboratory measurements in collaboration with colleagues as well as the soil physical properties carried out at the Lithosphere Research Laboratory (ELTE). Soil chemical properties (sedimentation, pH, carbonate and organic material content) were measured by the Department of Soil Science and Agricultural Chemistry, Szent István University. The chemical composition of the soil samples was measured at the Bureau Veritas Commodities Canada Ltd. Gamma spectrometry, radon exhalation and emanation were measured in the Institute of Radiochemistry and Radioecology, University of Pannonia where this author learned the methodology and participated in the sample preparation. Statistical and calculations were executed by the author.

6.2.1. Sampling point selection

The sampling design applied is the simple random sampling (SRS). This method eliminates biases that can be introduces in grid sampling (Brus and De Gruijter, 1993; Buja and Menza, 2013; Wang et al., 2012) and is based on the equal probability criterion. The geographical location of the sampling points was determined by using the tool “Create random points” of ARCGIS software (Buja and Menza, 2013; ESRI, 2016) in the selected area. Considering the laboratory analyses of the soil samples, the necessary repetitions and the expected statistical significance, 30 measurement sites were planned. The selected points were designed both for field measurements and soil sample collection dedicated to further laboratory analysis (Figure 7).

6.2.2. Field measurements

6.2.2.1. Soil gas radon concentration

Soil gas radon concentration was measured with the active detector AlphaGUARD connected to a soil probe at depths around 0.8 m in a flow mode for 11 minutes with a pump rate of 1 L m^{-1} according to the international standard ISO 11665-11:2016. The field campaign was performed in May and June of 2017. To quantify thoron (^{220}Rn) activity concentration, soil gas radon concentration were conducted using RAD7 Electronic Radon Detector connected to a soil gas probe (Durridge Company Inc., 2018) (Figure 9).

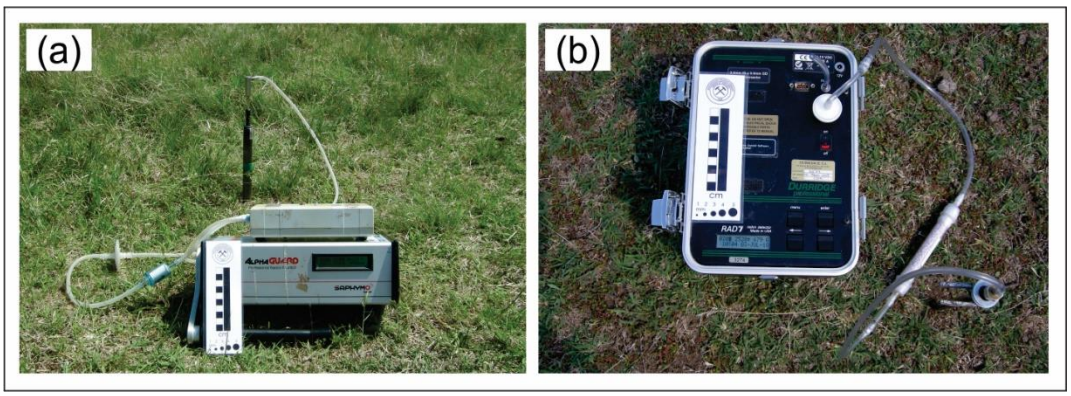

Figure 9. Soil gas radon concentration field measurements with a) AlphaGUARD and b) RAD7 active detectors radon monitoring.

The measurements were performed in thoron protocol, sniff mode, in 5 min measurement cycle. With the measured activities concentration of thoron and radon, the ratio $^{220}Rn/^{222}Rn$ was determined, for further data processing. The measurements were performed in July 2018. Considering the seasonal variability of the radon concentration, the measurements were planned to be executed under similar meteorological conditions. Therefore, rainy days as well as dry two days after precipitation were not take into account. Similarly, the measurements were carried out during the daytime from 7:00 until 19:00, take the daily variability of radon concentration into account. To ensure the representativity of the measurements, 3 replicates were measured at each sampling site (Figure 11), the replicates are located 1.5 m far from each other.

6.2.2.2. Soil gas permeability

The soil gas permeability was measured by Radon-JOK equipment as proposed by (Neznal et al., 2004). The basis of the measurement is the extraction of air from the soil by applying negative pressure. The measurements were performed using the same assemble of soil probe as the soil gas measurements at depths greater than 0.8 to prevents the interaction of the ambient air.

Figure 10. Soil gas permeability field measurement with Radon JOK

The soil probe was coupled to a 0.6 cm diameter pipe that conducts the air to the rubber sack. The air was extracted from the soil by the action of a weight which is moving down between two notches marked in the central axis. This distance determines the known air volume (2000 cm^3) in the rubber sack. The time of the displacement between the two notches (sinking time) was registered in the field and used for the calculation of the permeability according to the following formula based on Darcy's equation, assuming that the soil is homogenous and isotropic. Accordingly, soil gas permeability can be calculated by Eq.11:

$$\boldsymbol{K = \frac{Q*\mu}{F*\Delta P}} \qquad \text{Eq. 11}$$

where, K is permeability (m^2), Q is the air flow through the probe ($m^3\ s^{-1}$), F is the shape factor of the probe (m), μ is the dynamic viscosity of air (at T=10°C, μ=1.75 Pa.s) and ΔP is the pressure difference between the surface and the active area of the probe. In this case, the pressure is originated by the weigh, therefore the pressure difference with one weight is 2160 Pa (Neznal et al., 2004). The air flow is calculated in the following way, according to the manufacturer specifications (Eq. 12):

$$\boldsymbol{Q} = \frac{\boldsymbol{fixed\ volume\ (rubber\ sack\ Radon\ JOK)}}{\boldsymbol{sinking\ time}} = \frac{\mathbf{0.002}\ \boldsymbol{m^3}}{\boldsymbol{sinking\ time}\ (\mathbf{sec})} \qquad \text{Eq. 12}$$

The shape factor depends on the probe geometry and it is determined by using Eq. 13:

$$\boldsymbol{F} = \frac{\boldsymbol{2\pi L}}{\boldsymbol{ln}\left\{\frac{\boldsymbol{2L}}{\boldsymbol{d}}\left[\frac{(\boldsymbol{4D-L})}{(\boldsymbol{4D+L})}\right]^{\boldsymbol{1/2}}\right\}} \qquad \text{Eq. 13}$$

where, L is the length of the active area (m), d is the diameter of the active area (m), and D is the depth below the surface (m).

6.2.3. Soil sampling

To determine the corresponding soil properties, disturbed and undisturbed soil samples were collected at each sampling site. The soil samples were taken from two depths range, D1: 0.3 to 0.4 m and D2: 0.8 to 1.10 m, where the last depth corresponds to the total depth of the field measurements (Figure 11). The undisturbed and disturbed soil sampling methods are explained below.

6.2.3.1. Undisturbed soil sampling

Undisturbed soil sampling method preserves certain characteristics of the soil such as pore size distribution and water storage. From these, the bulk density, porosity and water content can be determined. This sampling method requires the use of a standard tool, a cylinder (ring) made of seamless tubes, smooth inside and out with a known volume coupled with an

extension to reach the desired depth (Smith and Mullins, 2000). The undisturbed sampling was executed using the sample ring kit - Augering & soil sampling equipment model C of Eijkelkamp (Eijkelkamp, 2009); the dimensions of the sampling ring is 53 mm diameter and 51 mm height. To increase the representability of the sample and decrease the error of measured parameters, 3 replicates per site were collected as it is schematized in Figure 11.

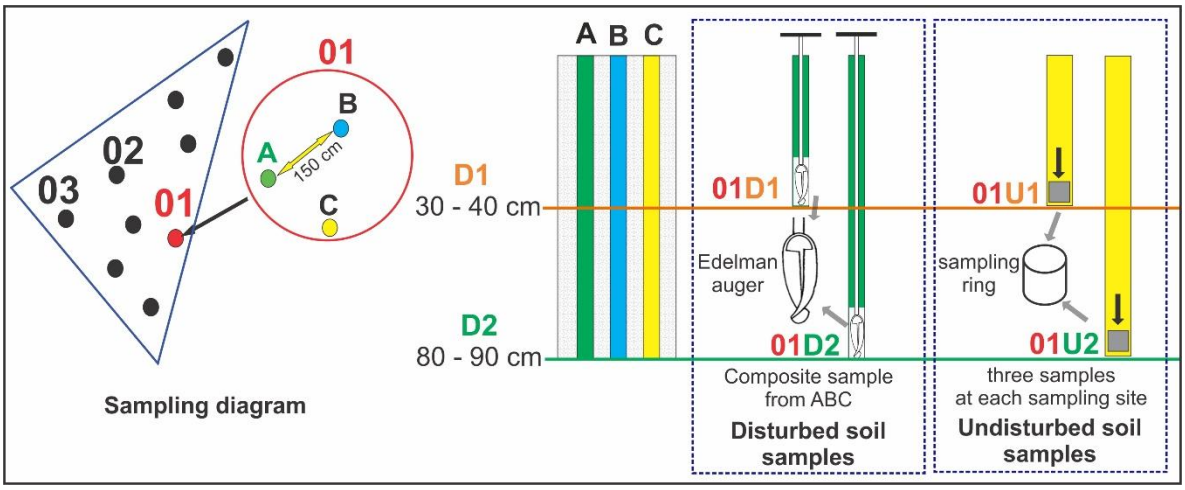

Figure 11. Soil sampling diagram illustrating the soil sampling methods.

6.2.3.2. Disturbed soil sampling

The disturbed soil sampling was carried out for determining the properties of the soil where its pore structure is not relevant (i.e. particle diameter size distribution, pH, organic content and carbonate content). The equipment used is an Edelman auger Eijkelkamp (Eijkelkamp, 2009). For this, a composite sample of the three replicates, at each measurement point, was collected from D1 and D2 depth (Figure 11).

6.2.4. Soil physical properties

The soil physical parameters have been determined from the undisturbed soil samples, following the gravimetry by drying the samples at 110 °C until a constant weight to evaporate the water content. The basis of this method is the measurement of the mass of the soil samples before and after dried (Hillel, 1998; Yu et al., 2015). These values were used for the determination of bulk density (wet and dry), water content and porosity.

6.2.4.1. Bulk density

This property was calculated based on the dried soil (dry bulk density) and in the wet soil mass (wet bulk density). (Hillel, 1998; Yu et al., 2015):

$$\boldsymbol{\rho_{bulk\ dry}} = \frac{\boldsymbol{m_{dry\ soil}}}{\boldsymbol{V_{sample}}} \quad \text{Eq. 14}$$

$$\boldsymbol{\rho_{bulk\ wet}} = \frac{\boldsymbol{m_{wet\ soil}}}{\boldsymbol{V_{sample}}} \quad \text{Eq. 15}$$

$\rho_{bulk\ dry}$: bulk density (kg m^{-3})

$\rho_{bulk\ wet}$: wet bulk density (kg m^{-3})

6.2.4.2. Water content

The water content of the soil can be expressed in units of mass or volume. It is the ratio between the mass of the liquid (water) and the mass of the dry soil (Hillel, 1998; Yu et al., 2015):

$$\boldsymbol{w_m} = \frac{\boldsymbol{m_{wet\ soil} - m_{dry\ soil}}}{\boldsymbol{m_{dry\ soil}}} \boldsymbol{x100} \quad \text{Eq. 16}$$

$$\boldsymbol{w_v = w_m} \frac{\boldsymbol{\rho_{bulk\ dry}}}{\boldsymbol{\rho_{water}}} \quad \text{Eq. 17}$$

The water content into the soil can be increased until the point that the water occupies all the pore space, it means that the volumetric water content is equal to the porosity, this point is called water saturation (Hillel, 1998; Yu et al., 2015). The volume fraction of water saturation is calculated by the Eq. 18:

$$\boldsymbol{s} = \frac{\boldsymbol{w_v}}{\boldsymbol{p_t}} \quad \text{Eq. 18}$$

w_m: gravimetric water content (%)

w_v: volumetric water content (%)

s: volume fraction of water saturation

6.2.4.3. Porosity

Total porosity is defined as the ratio of the pore volume and the total soil volume (Carter and Gregorich, 2008; Yu et al., 2015):

$$\boldsymbol{p_t = 1 - \frac{\rho_{bulk\ dry}}{\rho_{solids}}} \quad \text{Eq. 19}$$

p_t: total porosity

ρ_{solids} : density of the solids 2650 (kg m^{-3})

Effective porosity is also called macroporosity, considering that the macropores are the primary pathway for the flow when the water is saturated (Carter and Gregorich, 2008; Rogers and Nielson, 1991b; Yu et al., 2015). This parameter was determined using the expression proposed by Rogers and Nielson, (1991b) (Eq. 20):

$$\boldsymbol{p_e = p_t(1 - s + sk_H)} \quad \text{Eq. 20}$$

p_e : effective porosity

k_H: Henry's law constant, k_H=0.22 at 20 °C (Sander, 2015; Wilhelm et al., 1976)

Air filled porosity, is the corresponding porosity that excludes the volumetric fraction of water is the pore space and it is defined as it follows (Hillel, 1998; Yu et al., 2015) (Eq. 21):

$$\boldsymbol{p_a = p_t - w_v} \quad \text{Eq. 21}$$

6.2.4.4. Particle size distribution

Considering that the permeability is strongly dependent of particle diameter (Nazaroff, 1992), which is reflected in the empirical predictive model (Eq. 6) (Rogers and Nielson, 1991a), the accuracy in the determination of this parameter is fundamental. Thus, the method applied for the determination of particle size diameter can modify the predictive power of the empirical model evaluated in this research. In this research, two methods have been applied for the determination of the particle size distribution, dry sieving complemented by sedimentation and laser diffraction.

Sedimentation method, based on the Stokes sedimentation rates, assumes spherical and smooth particles with similar densities and neglects the effect of the walls of the sedimentation column (Ferro and Mirabile, 2012), which induces error in the representation of the real distribution. On the other hand, laser diffraction is a widely used technique for the determination of grain size distribution. This method is based on the forward scattering of monochromatic coherent light that considers the particles as a two-dimensional object and determines the particle size as a function of the cross-sectional area (Konert and Vandenberghe, 1997). Therefore, the accuracy and reproducibility are demonstrated by several studies to be superior in comparison with sedimentation method (Ferro and Mirabile, 2012; Konert and Vandenberghe, 1997; Li et al., 2005). Additionally, Konert and Vandenberghe (1997) proposed that grain size < 0.002 mm defined for the clay fraction by the sedimentation method is equivalent to grain size < 0.008 mm using the laser diffraction (Konert and Vandenberghe, 1997).

Since the empirical model Rogers and Nielson (1991) was developed by applying the standard method ASTM D422-63 that includes dry sieving and sedimentation, similar procedure was followed in this research to test the usability of this model. In study published by Rogers and Nielson (1991), dry sieving was applied in the range of 4.75 - 0.074 mm, and sedimentation for the faction < 0.074 mm. In present research, the dry sieving was performed in the range of 6.3 -0.063 mm, using the vibratory sieve shaker Fritsch Analysette 3 with the following sieves: 6.3 mm, 4 mm, 2mm, 1 mm, 0.5 mm, 0.250 mm, 0.125 mm, 0.063 mm at the Department of Petrology and Geochemistry of Eötvös Loránd University. The sedimentation analysis was performed in the Department of Soil Science and Agricultural Chemistry, Szent István University. For this analysis, the samples were treated by a solution of 0.5 N Sodium Pyrophosphate ($Na_4P_2O_7$), fraction greater than 0.05 mm was separated by sieving and the fraction lower than 0.05 mm was analyzed by sedimentation. For the soil texture classification the following size fractions were considered: sand (2 – 0.05 mm), silt (0.05 – 0.002 mm) and clay (<0.002 mm) (USDA, 2014).

The particle size distribution for laser diffraction was measured by Horiba Partica 950-V2 LA Analyzer at the Laser Diffraction Particle Size Distribution Analyzer Laboratory, of the Research and Instrument Core Facility of Faculty of Sciences, Eötvös Loránd University. To determine the grain size distribution by this method, the fractions greater than 2 mm were

previously separated by dry sieving (sieves: 6.3 mm, 4 mm, 2mm) and the fraction smaller than 2 mm was analyzed by laser diffraction in distilled water medium with continuous circulation (circulation speed: 9/15, agitation speed 7/15). In this method, the clay fraction is considered smaller than 0.008 mm (Konert and Vandenberghe, 1997).

Subsequently, the particle size diameter will be calculated based on the grain size distribution determined by both methods, respectively. Arithmetic mean, geometric mean and median diameter were calculated for its use as input parameter in the empirical model for the prediction of soil gas permeability.

6.2.4.5. Arithmetic mean diameter

Arithmetic mean diameter is a central tendency parameter, which is accurate when there is normal (symmetric) distribution (Merkus, 2009):

$$d_a = \frac{\sum_{i=1}^{n} d_i * f_i}{\sum_{i=1}^{n} f_i} \qquad \text{Eq. 22}$$

d_a: arithmetic mean diameter

d_i: diameter of the class (arithmetic mean diameter of the particle size limits)

f_i : primary particle size fraction

6.2.4.6. Geometric mean diameter

Geometric mean diameter is used when particle size of the soil is log-normal distributed when the distribution is symmetrical around the geometric mean in a logarithmic scale (Merkus, 2009):

$$d_g = \exp\left[\frac{\sum_{i=1}^{n} f_i * \ln(d_i)}{\sum_{i=1}^{n} f_i}\right] \qquad \text{Eq. 23}$$

d_g: geometric mean diameter

d_i: diameter of the class (arithmetic mean diameter of the particle size limits)

f_i: primary particle size fraction

6.2.4.7. Median diameter

The median diameter corresponds to the "middle" particle diameter value, separating the higher half from the lower half of the all particle size values. The advantage of the median respect to the arithmetic and geometric mean diameter is that it is independent of the statistical distribution and outliers. From the granulometric curve, it was determined the particle diameter as well as the median diameter (Merkus, 2009):
d_m: median particle diameter

6.2.5. Soil chemical properties

6.2.5.1. pH

The pH of the soil was measured in suspension in 1:2.5 soil to liquid ratio, in distilled water and in 1N KCl solution. The second one is also called exchange acidity and represents the exchangeable aluminum that can be extracted from the soil with a 1N KCl solution. Generally, the pH is determined in KCl is 0.5 to 1 unit lower than the determined in distilled water. Both measurements in conjunction give information about the nature of the total charge of the colloidal system, indicated by the sing of the difference ($\Delta pH = pH_{KCl} - pH_{H_2O}$) between them. If this value is negative, the colloid has a negative net charge and if it is the positive, the colloid has a positive net charge (USDA, 2014).

6.2.5.2. Carbonate content

The carbonate content was determined by treatment with 1N KCl solution from the international standard IS0 10693. This method is based on the following reaction (Pansu and Gautheyrou, 2006):

$$CaCO_3 + 2\,HCl \leftrightarrow CaCl_2 + H_2O + CO_2 \qquad \text{Eq. 24}$$

The produced CO_2 is measured at controlled temperature and pressure, using a Scheibler calciminer.

6.2.5.3. Organic content

Organic content was determined by the gravimetric method, considering the percentage of matter lost on ignition at 110 °C. The remain constitutes are considered as the mineral content (USDA, 2014).

6.2.5.4. Chemical composition of soil samples

In order to evaluate the controlling factors influencing the soil gas radon concentration and its geogenic sources, the chemical composition of soil within the studied area were selected along the cross-section A-B (Figure 30). This section comes across 7 measured sites (11, 10, 15, 23, 22, 24, 25) along a slope with a decreasing soil gas radon concentration from left to right (west to east), obtaining a radon concentration profile along the study area. For this purpose, the seven soil samples have been selected for major, minor and trace element compositions, including U, Th, Zr, Y, Ce, La, Rb, Al, Ca, Mg, by Inductively Coupled Plasma Mass Spectrometry (ICP-MS) by Bureau Veritas Commodities Canada Ltd. in Canada. Before the analysis, however, the soil samples under 2 mm were dried and pulverized in mild steel pulverizer. After homogenization, 15 g of sample were digested in modified aqua regia (1:1:1 HNO_3:HCl:H_2O).

6.2.6. Natural radionuclides in soil

6.2.6.1. Gamma spectrometry

To determine the activity concentration of the gamma emitters of ^{238}U, ^{232}Th, ^{226}Ra, ^{40}K, the soil samples were analyzed by gamma spectrometry at the Institute of Radiochemistry and Radioecology, University of Pannonia. For this purpose, approximately 1 kg of each soil sample was dried at 105 °C, homogenized and crushed under 0.63 mm. A portion of the samples was filled in a Marinelli baker (covered by a plastic film) with 600 cm^3 volume and then closed and sealed for 27 days for reaching the equilibrium between the measured radionuclide and its radioactive progenies.

The instrument used is a high-resolution gamma spectrometer with a high resolution ORTEC GMX40-76 HPGe semiconductor detector, with a 3 – 10000 keV, 42 % efficiency (^{60}Co 1332.5 KeV peak). The detector has a 10 cm thick lead shielding wall and 1 cm steel cover to avoid the influence of background radiation.

The specific activity concentration of ^{226}Ra was obtained from ^{214}Pb (295 keV) and ^{214}Bi (609 keV). Also, specific activity concentration of ^{232}Th was obtained from ^{228}Ac (911 keV) and ^{208}Tl (261 keV), where for ^{40}K the 1460 KeV energy was used.

6.2.6.2. Radon exhalation rate and emanation coefficient

Radon exhalation rate was measured at the Institute of Radiochemistry and Radioecology, University of Pannonia following the method of Sas et al. (2015). The measurement system is schematized in Figure 12 and the procedure is summarized below.

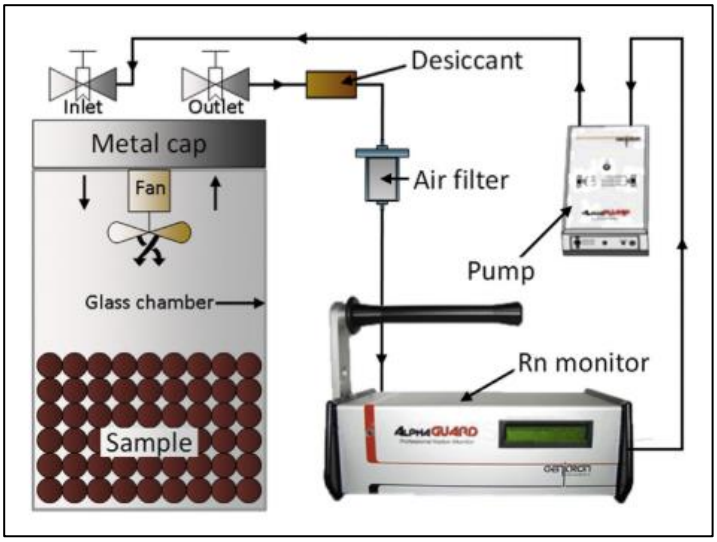

Figure 12. Radon exhalation measurement closed loop system.
Source: Sas et al. (2015)

The exhalation rate was determined by placing 500 g of the sample (dried at 105 °C, homogenized and crushed under 0.63 mm), in a glass accumulation chamber covered by a metal cap, filled with N_2 to ensure a radon free initial condition. The volume of the chamber is about ten times higher than the sample to avoid the back diffusion of radon and a 12V DC ventilator inside the chamber ensures the homogeneity of the inner air. After the

accumulation period, the air is extracted from the chamber with a radon proof pump, go through a filter system for progenies, soil particles, and wetness, and enters to AlphaGUARD 2000 portable radon monitor (under 10 min flow mode) to measure the radon activity concentration, connected within a closed loop (Figure 12). To avoid the thoron interference that cannot be detected by this instrument, the air flow was stopped after 20 minutes and the measurements were continued for 40 more minutes. When the pump stopped, thoron decay within 10 min, thus the average activity radon concentration can be measured only after 30 - 60 min (Sas et al., 2015).

After the measurements, the radon monitor was removed from the loop. The remaining concentration in the chamber was measured and the volume corrected considering the volume of AlphaGUARD and its accessories (e.g., pipes, desiccant and detector chamber). The leaking rate was measured using a PYLON RN 2000A-type passive radon source, which was lower than 1 % (Sas et al., 2015).

The radon exhalation per unit of mass was calculated using Eq. 25:

$$E = C_0 e^{-\lambda t} + \frac{CV}{mt}\frac{\lambda t}{1-e^{-\lambda t}} \qquad \text{Eq. 25}$$

E : radon exhalation rate per unit of mass (mBq kg^{-1} h^{-1})

C_o: initial radon activity concentration (Bq m^{-3})

C: accumulated radon activity concentration (Bq m^{-3})

λ: effective decay constant (h^{-1})

V: Total volume of the system (m^{-3})

t: accumulation time (h)

m: mass of the sample (kg)

6.2.7. Theoretical and empirical predictive models tested

The criteria for the selection of the models was based on one of the aims of this study that is to test usability of models for C_∞ and K prediction, which uses soil physical and geochemical parameters that can be found in national and regional databases. In this sense, two theoretical models for radon concentration estimation were selected. The first one is the relationship

proposed by Porstendorfer (1994) that is widely used and called MR1 (see Eq. 8). The second model is proposed by Várhegyi et al. (2013) and called MR2 (see Eq. 9). It is basically a modification of the first one by introducing a correction factor to consider the radon concentration in the water phase in the pores that is neglected in model MR1.

Among the theoretical and empirical models available in the literature that involves pore structure information of soils, the model proposed by Rogers and Nielson (1991), represents a simpler empirical approach involving properties that can be found in common databases (see MP, Eq. 6).

6.2.8. Statistical analysis

Univariate and bivariate analysis were performed following the methods described for ambient gamma equivalent dose rate in section 6.2.1. The central tended indicator consider in this research is median. The variability of the measured data is expressed by the standard deviation, whereas for the estimated parameters it is expressed by the error propagation based on Taylor's series method by using the propagate R-package (Spiess, 2018). The multivariate linear regression was used for the determination was used to construct a predictive model by the least squares regression method (Reimann et al., 2008).

7. Results and discussion

7.1. Results of ambient gamma dose equivalent rate

7.1.1. Statistical analysis

The summary statistics of the 300 field measurements of ambient gamma dose equivalent rate at 0 m and 1 m, respectively, are detailed in the Table 4. The average values of gamma dose rate in both heights are in the range of the Hungarian national average: 58-161 nSv h^{-1} (NERMS, 2014).

Table 4. Summary statistics of the ambient gamma dose equivalent rate field measured

H*(10) at	Min. (nSv h^{-1})	Max. (nSv h^{-1})	Mean (nSv h^{-1})	STDEV (nSv h^{-1})	Rel. var. (%)	Median (nSv h^{-1})	MAD (nSv h^{-1})
0 m	48.7	214.3	102.5	27.5	27	100.0	16.9
1 m	48.5	206.6	94.6	21.7	23	91.3	13.4

Since 3 - 6 measurements of ambient gamma dose rate were performed, at each sampling site, it is important to evaluate its variability represented by the standard deviation. In this sense, a statistical analysis was performed for ambient gamma dose rate and its standard deviation, based on the 3 - 6 measurements carried out at each of the 300 sampling sites. Table 5 presents the minimum, maximum and average of the standard deviation and ambient gamma dose rate. The standard deviation remains in average within the 10 % at each sampling site, which is an acceptable uncertainty for the purpose of this research.

Table 5**.** Statistics of the standard deviation calculated within 3 - 6 gamma dose rate measurements in each measurement site

H*(10)	Standard deviation of gamma dose rate at each sampling site (nSv h^{-1})	Related average gamma dose rate at each sampling site (nSv h^{-1})
	at 0 m	
minimum	0.2 (n=300)	80.5 (n=1)
maximum	42.8 (n=300)	146.3 (n=1)
average	10.3 (n=300)	102.5 (n=300)
	at 1 m	
minimum	0.5 (n=300)	76.4 (n=1)
maximum	43.3 (n=300)	206.6 (n=1)
average	9.3 (n=300)	94.6 (n=300)

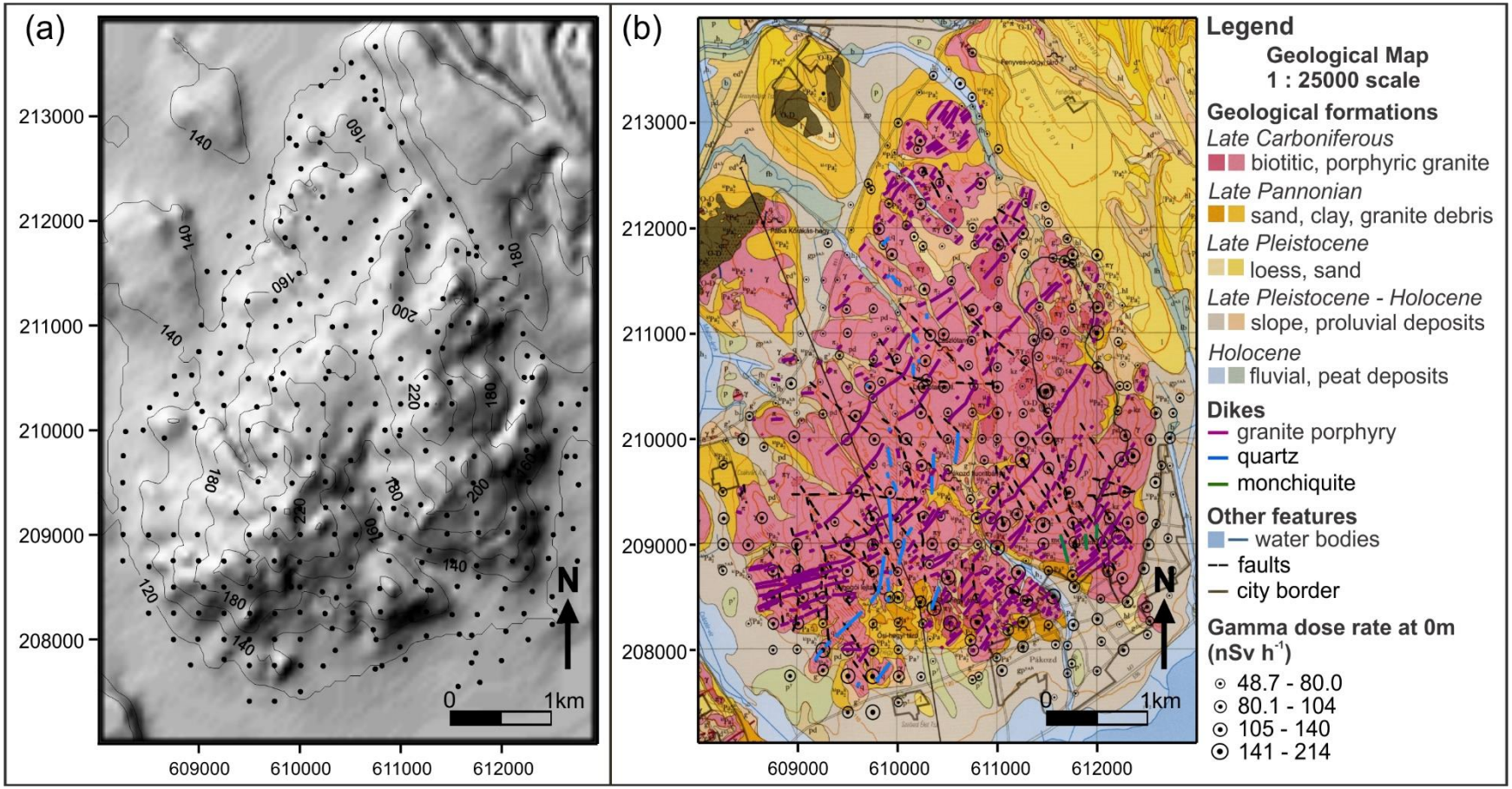

Figure 13. a) Topographic shaded relief model with the elevation contour lines overlaid and the field measured sites (solid dots). b) Geological map overlaid by the fault lines, dikes and the gamma measured sites represented by circles which radii is proportional to the correspondent gamma dose rate value.

Significant relationship between gamma dose rate at 0 m and 1 m height, excluding the outliers, was determined by simple bivariate regression obtaining a linear correlation coefficient (r) 0.98. Similar correlation of gamma dose rates, measured at 0 m and 1 m, was reported for another area of Hungary with highly different geological background, lower sampling density and with an average sampling distance of 3.2 km by Szabó et al. (2017). Results of the univariate statistical analysis of 0 m values are shown in Table 4 and Figure 14.

Ten univariate outliers were identified in the range of 175-214 nSv h^{-1}, which are located in the southern part of the study area (see Figure 16a). In all of the identified four bivariate outliers, the 0 m value is higher than 1 m value and all of them are located in the southern part of the study area similarly to univariate outliers (see Figure 16a). Since one of the aims of this research is to relate the gamma dose rate to the local geology, only the measured gamma dose rate at surface level (0 m) was considered for further analysis.

Geological formations at the study site belong to three different geological periods, Carboniferous (327-290 Ma), Neogene (6-2.4 Ma) and Quaternary (0.13 Ma – present), based on the 1:25,000 scale geological map of the Velence Hills (Figures 13b, 14b and c) (Gyalog and Horváth, 1999; Horváth et al., 2004). In the map, the Quaternary formations are subdivided into three units: late Pleistocene, late Pleistocene-Holocene and late Holocene times (Figure 14b).

Box-and-whiskers plots of gamma dose rate measured over formations of different geological ages are arranged in the order of decreasing geological age in Figure 14b. The highest average gamma dose rate value (median 109.3 nSv h^{-1}) belong to late Carboniferous time, represented by the prevailing Velence granite formation in the study area (Figure 14b) including most of the outlying values. Median gamma dose rate value of the Carboniferous time differs from the other ages according to the Mann-Whitney test. However, the gamma dose rates over the Neogene and Quaternary ages do not have statistically significant differences in the median (Figure 14b). Therefore, the gamma dose rates are not related to the age of the geological formations in the study area. Consequently, age of the geological formations is not a very proper indicator for gamma dose rate in this research area.

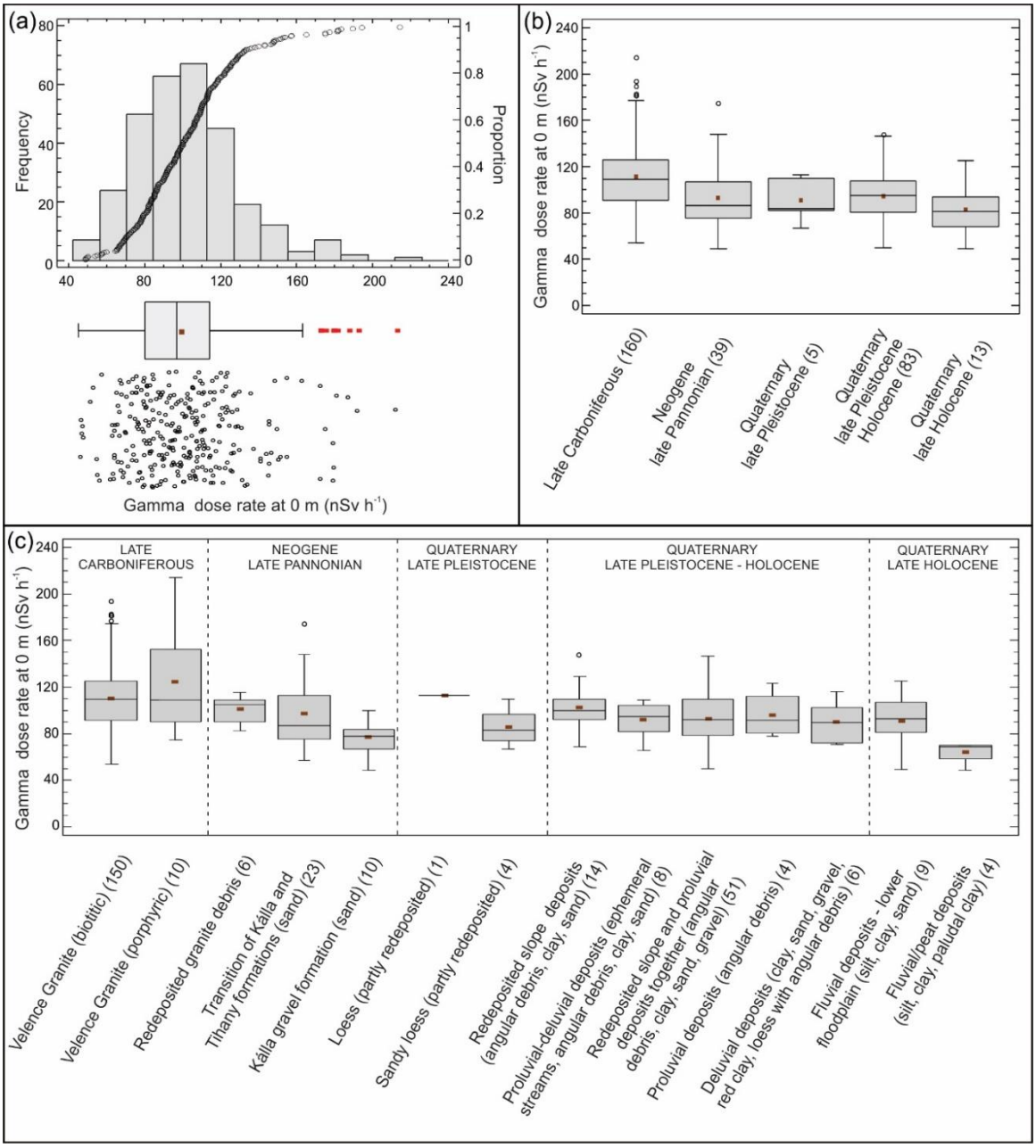

Figure 14. Statistical analysis of gamma dose rate values measured at surface. a) Empirical histogram and cumulative density plot of gamma dose rate. b) Box-and-whiskers plots of gamma dose rate measured over different geological ages. c) Box-and-whiskers plots of gamma dose rate measured over different geological formations. Numbers in the brackets are the number of measurement sites.

Box-and-whiskers plots of gamma dose rate measured over the different geological formations are arranged first in the order of decreasing geological age and second in the order of decreasing median value (Figure 14c). Late Carboniferous Velence granite has the highest

gamma dose rate median value as it is expected for acidic igneous rocks (like granite) (UNSCEAR, 2000). Similar results were found in Spain by García-Talavera et al. (2013), where the average gamma dose rate in the Paleozoic acid plutonic rock are higher than any kind of Neogene formations. Two types of the Velence granite, biotitic and porphyric ones, distinguished in the geological map (Horváth et al., 2004; Jordan et al., 2018), have the same median gamma dose rate value (109.7 nSv h^{-1} and 109.0 nSv h^{-1}, respectively, Figure 14c) based on the Mann-Whitney median homogeneity test. Thus, they can be grouped together from the gamma dose rate point of view. Note that the redeposited granitic debris of Neogene age derived from the main granitic rocks (Horváth et al., 2004) has similar gamma dose rate value (median 105 nSv h^{-1} based on 6 measurements). However, we cannot state that it is statistically similar to Velence granite formation, since the minimum data for the Mann-Whitney median homogeneity test is 9 (Mann and Whitney, 1947). Two other sand formations from the Neogene, the Transition of Kálla and Tihany formations and the Kálla gravel formation are similar, having median values of 87.1 nSv h^{-1} and 78.0 nSv h^{-1}, respectively. Thus, these can be grouped together from gamma dose rate point of view. They are also statistically different in the median from Velence granite formation. All of the Quaternary formations, having enough data for the test, are similar statistically.

The relationship between gamma dose rate and dyke density, local variability index, local topographic terrain relief and variability index obtained from the digital elevation model, was evaluated by linear regression. The corresponding plots are shown in Figure 15, where Pearson's linear correlation coefficients are shown in each plot and red crossed points are bivariate outliers excluded from the regression analysis. Simple regression between the measured gamma dose rate and the felsic dike density at each of the 300 measurement sites (Figure 15a) shows a significant positive correlation ($r=0.34$, $p=0.00$). This positive correlation between gamma dose rate and dike density could be attributed to elevated U and Th concentration of the dikes, which are essentially granite porphyry, compared to the host granite body. Significant positive linear correlation was found between gamma dose rate and its variability index ($r=0.54$, $p=0.00$). Thus, where the gamma dose rate is high it is also variable, and where it is small, it is less variable (Figure 15b, 16a and b). The correlation coefficient should be viewed with caution, however, as variability index is calculated from the gamma dose rate values and, thus, it is not an independent variable. The correlation

between the gamma dose rate and the elevation above sea level was evaluated, however, no linear correlation was found (r=0.16, p=0.0049). Similar result was found by Szabó et al. (2017). However, there is a significant correlation between the relief and variability index of the topographic elevation (DEM) and the measured gamma dose rates (r=0.41, p=0.00 and r=0.38, p=0.00, respectively) (Figure 15c and d). Most probably this apparent correlation is induced by the resistance of felsic dikes against weathering, which results in high surface variability, why the chemical composition of the dikes contributes to the high measured gamma dose rates.

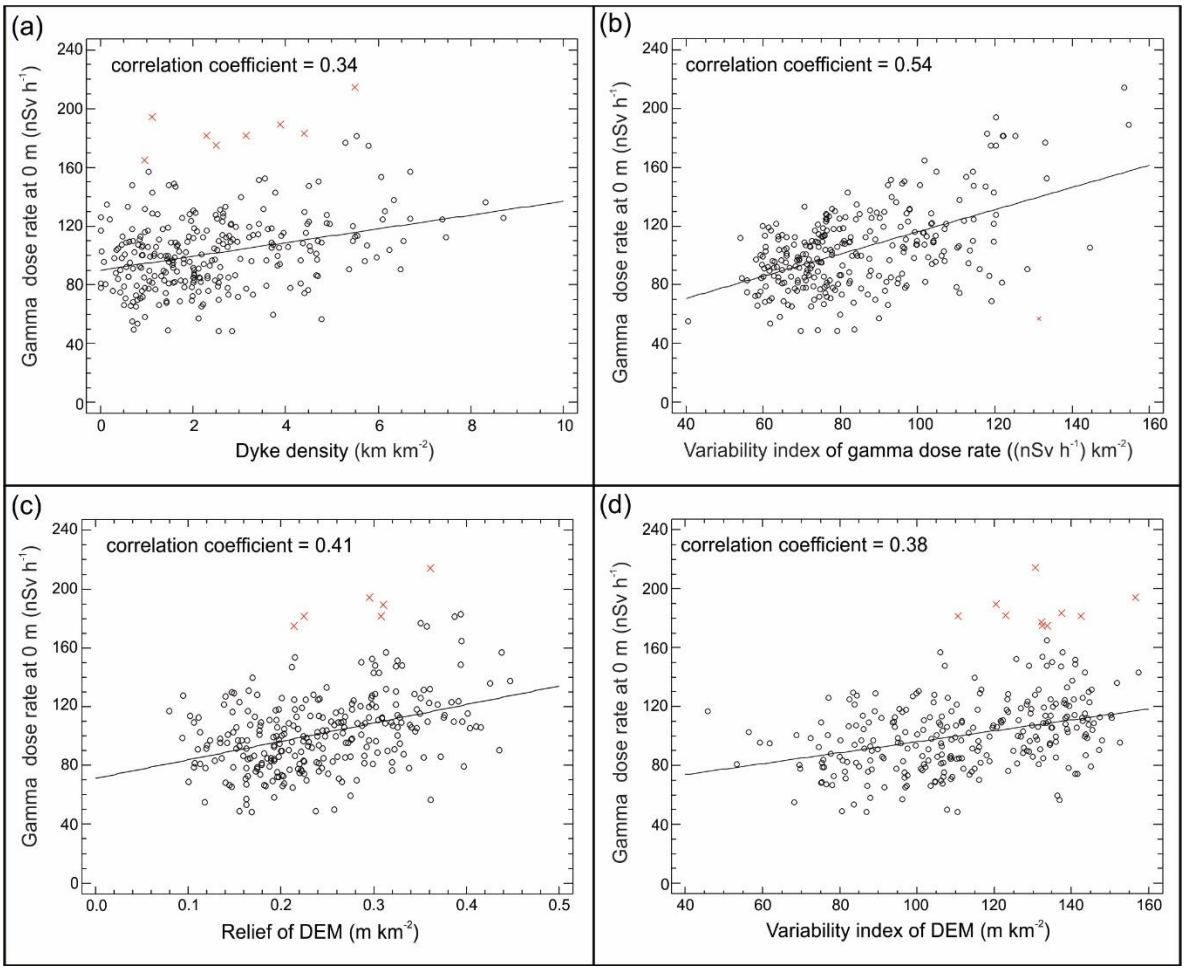

Figure 15. Bivariate regression analysis of gamma dose rate with a) dyke density; b) variability index of ambient gamma dose rate; c) local variability of digital elevation model (DEM) measured by the relief and d) local variability of digital elevation model (DEM) measured by the variability index.

7.1.2. Mapping and spatial analysis

The interpolated surface of ambient gamma dose rate is the base for the spatial analysis; thus, the smoothed interpolated surface has been evaluated by the estimation of the error of interpolation. Results of this procedure show that the applied smoothed triangular irregular network (TIN) interpolation (Guibas and Stolfi, 1985) is a good model as the average error is -1.21 nSv h^{-1}, equal to a 1.3 % relative error, with unbiased symmetric distribution. The t-test confirmed that the expected average error is zero at the 95 % confidence level. The outlier free data set has a lower average error of -0.75 nSv h^{-1} equal to a 0.8 % relative error. At the few (10) outlier values, in the main linear zone anomaly (Figure 16a), the error can be as high as -47 and 76 nSv h^{-1}, which confirms the efficiency of the applied smoothing for regional trend pattern recovery.

The obtained smoothed interpolated surface of ambient gamma dose rate is shown in Figure 16. Figure 16a and b show the TIN interpolated surface for the gamma dose rate calculated for all data and excluding the outliers, respectively.

Figure 16a is a composite image of the color-coded gamma dose rate map with the contour lines and the shaded relief map. Overlaid to this map are the local maxima (purple dots), univariate outliers (light green crosses), bivariate outliers (light blue circles) and the digital cross-sections along the identified patterns. It can be noticed that all of the univariate outliers and bivariate outliers are located in a SW-NE trending zone in the southern part of the study area (Figure 16a).

In the smoothed TIN model for the gamma dose rate without outliers shown in Figure 16b, the dikes and faults extracted from the 1:25,000 scale geological map of Velence Hills (Horváth et al., 2004; Jordan et al., 2018) are also overlaid to illustrate their location in the high gamma dose rate zones. The high anomalous gamma dose rates have a predominant SW-NE trend and are associated to high fault and dike density zones (Figure 16b and 17). Despite the high enrichment in U and Th of monchiquite dikes (Szabó et al., 1993), no anomalies on ambient gamma dose rate were found directly related to these dikes in the study area. It can be explained by the fact that spatially distribution of these three dikes is steep (i.e., subterraneous), therefore their influence on the surface is rather punctual, and their presence was not reflected in the site of the particular sampling grid.

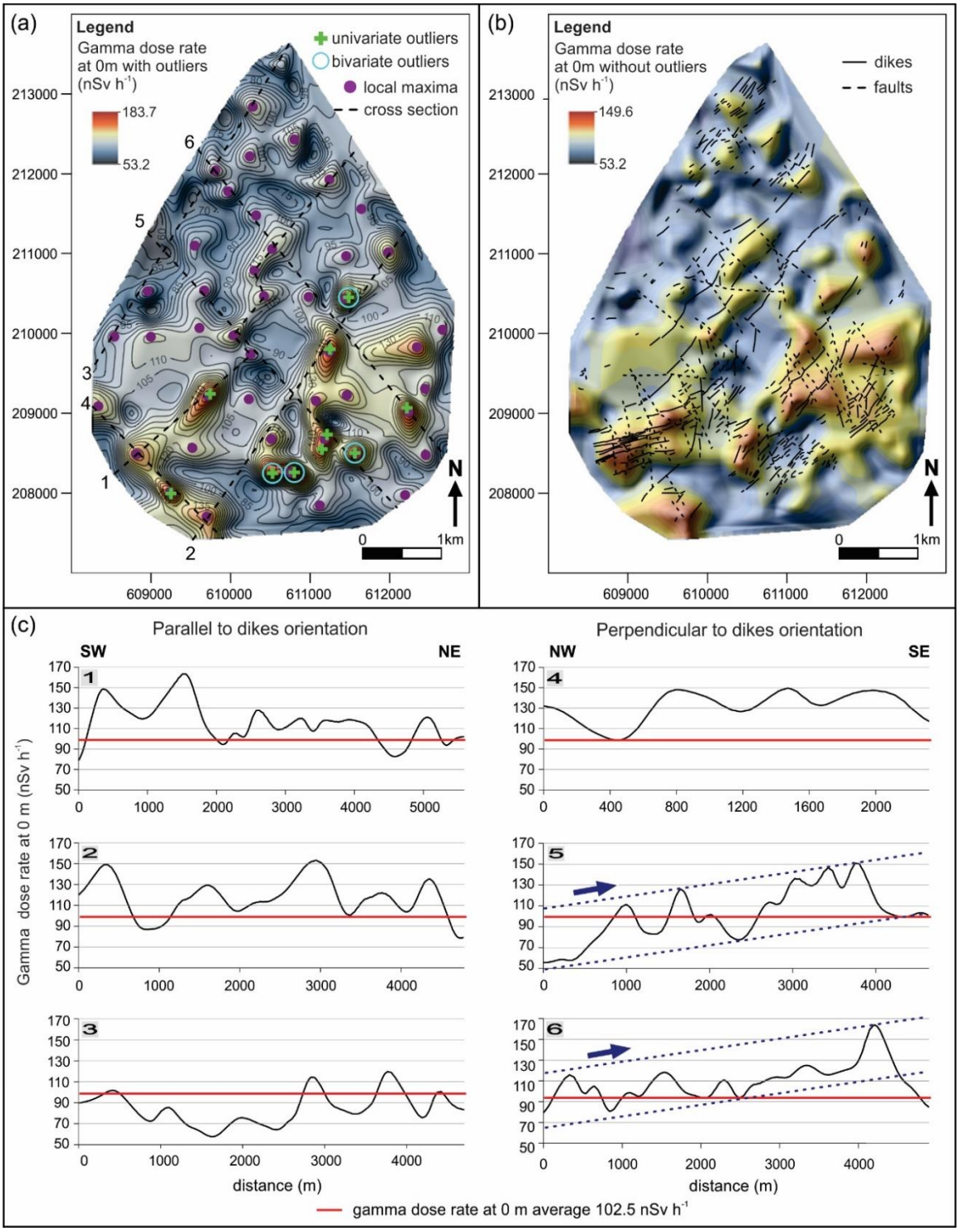

Figure 16. Smoothed triangular irregular network (TIN) interpolated surface for gamma dose rate measured at 0 m; a) including outliers (univariate: light green crosses and bivariate: light blue circles), showing the local maxima (purple dots) and b) excluding the outliers, with dikes and tectonic fault lines overlaid. c) Digital cross-sections along high gamma zones identified in a) showing the average gamma dose rate in red.

Digital cross-sections (Figure 16c) were calculated in SW-NE (cross sections: 1, 2, 3) and SE-NW (cross sections: 4, 5, 6) directions, oriented parallel and perpendicular to the orientation of dikes (see Figure 22), respectively, in order to capture spatial trends.

Cross sections 1 and 2 were made in SW-NE orientation along the highest gamma zones (Figure 16a and 16c). They clearly show that gamma dose rates are above the average in these zones (102.5 nSv h^{-1}) (red lines in Figure 16c). It is obviously seen that this area is characterized by granite porphyry dike systems of the same SW-NE orientation. Moreover, high density of dikes characterizes the areas around anomalous high gamma dose rate zones (Figure 17). Cross-section 3 located entirely in the northwest shows low gamma dose rate values calling attention to heterogeneity in the study area (Figure 16a and c). Digital cross sections 5 and 6 drawn in SE-NW orientation show a significant increasing tendency of gamma dose rate towards to south, illustrated by blue dashed lines and arrows in sections 5 and 6 in Figure 16c, where the high dike density was revealed (Figure 17).

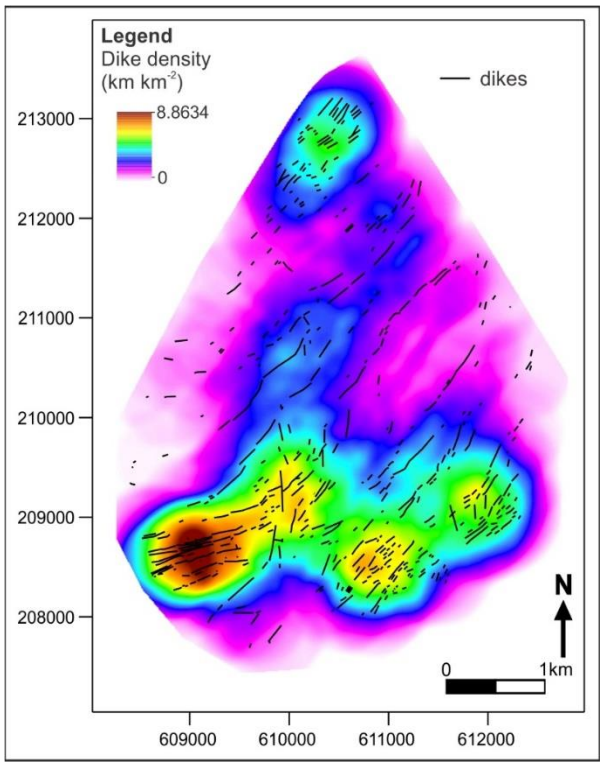

Figure 17. Dike density map, also showing the dikes (black lines).

The dike density map (Figure 17) shows the highest values (8.86 – 5.35 km km^{-2}) in the southern part of the study area where high gamma dose rates were also identified (Figure 16). This was also confirmed by significant linear correlation (r=0.34, p=0.00) between these two parameters described above (Figure 15a).

Local variability of gamma dose rate is represented by relief and variability index, respectively (Figure 18a and 18b). Both maps are overlaid by the dikes and it can be noticed that the high relief and variability index (high local variation) values concentrate in the high dike density field in the southern part of the study area.

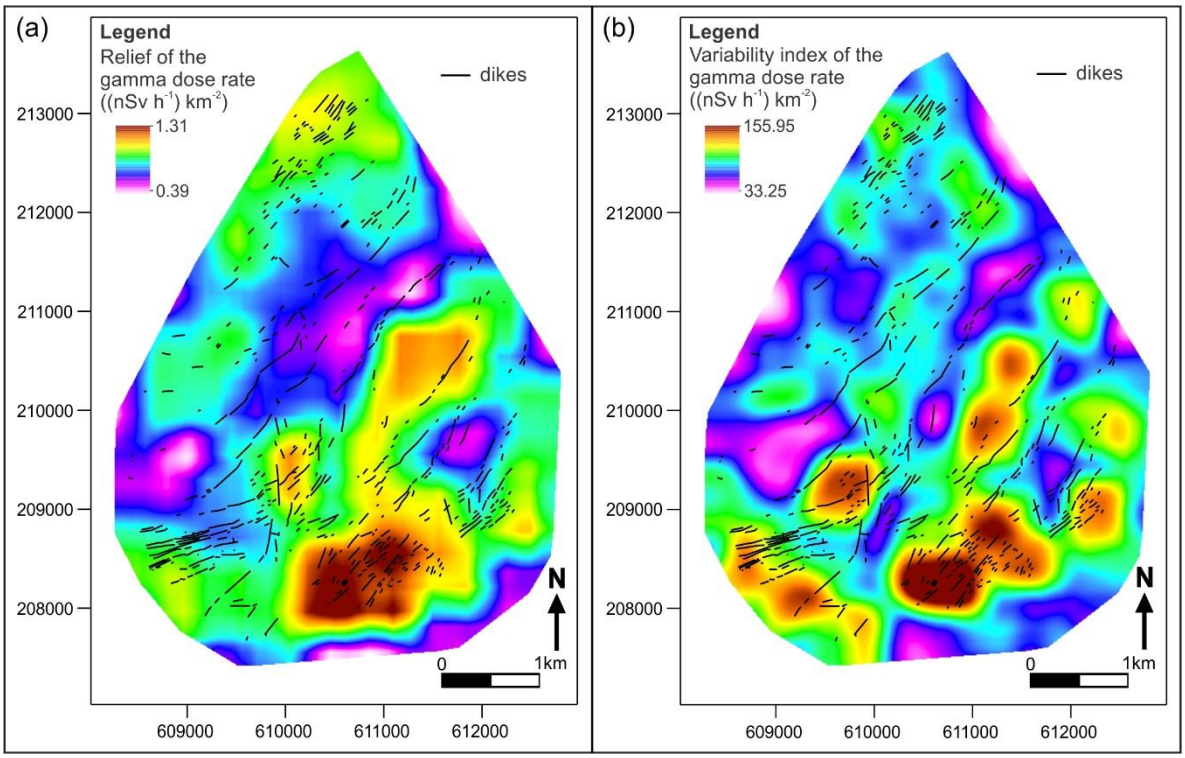

Figure 18. Local variability analysis for the measured gamma dose rate at the surface, obtained by two methods: a) relief and b) variability index, overlaid by the dikes.

High relief (1.31 – 0.97 nSv h^{-1} km^{-2}) and local variability (155.95 – 103.17 nSv h^{-1} km^{-2}) values were found in the high granite porphyry dike density zone in the southern part of the study area, southward from about 210 000 latitudes (Figure 17). It was also confirmed by bivariate regression analyses among these variables (r=0.33, p=0.00 and r=0.44, p=0.00, respectively). The low and high local variability zones follow SW-NE trends and have sharp linear edges in the middle of the study area in parallel to the orientation of the majority of the

dikes (Figure 18a and 18b). These findings also show that the dikes are related to the measured gamma dose rates spatial distribution.

The spatial autocorrelation of gamma dose rate at 0 m without outliers is represented in the 2D autocorrelogram (Figure 19a) illustrating a striking anisotropy in the SW-NE orientation, parallel to the main dikes (see Figure 22). The directional variograms in SW-NE and the perpendicular directions identify and describe the same anisotropy emphasized by the solid white arrow in Figure 19b and 19c.

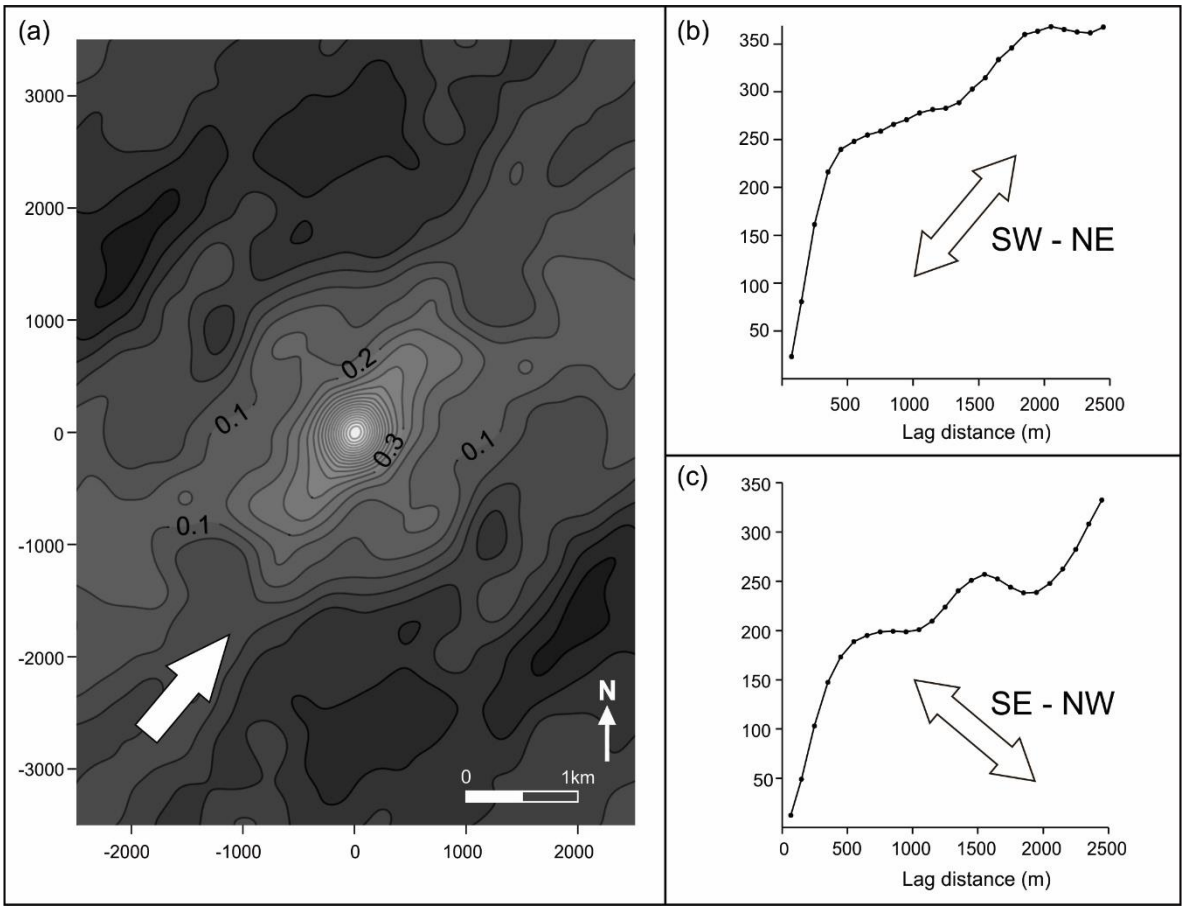

Figure 19. Spatial autocorrelation analysis for the measured gamma dose rate at the surface represented by a) 2D autocorrelogram and directional variograms in two directions: b) parallel to the main dike orientation SW-NE (azimuth 60 degree, tolerance 30 degree) and c) parallel to the major fault lines SE-NW (azimuth 150-degree, tolerance 30 degree).

The direction of the major change in gamma dose rates per distance unit, the gradient direction, is shown in Figure 20. Gray scale gamma gradient direction map (Figure 20a) reveals the predominant gradient direction and its spatial location. The orientation was

classified in classes of 45 degrees (Figure 20b) to identify regions with similar gradient direction. The predominant direction (270-360 °) marked with blue in the figure has SW-NE trending linear edges, white arrows in the Figure 20, corresponding to the main orientation of dikes (see Figure 22).

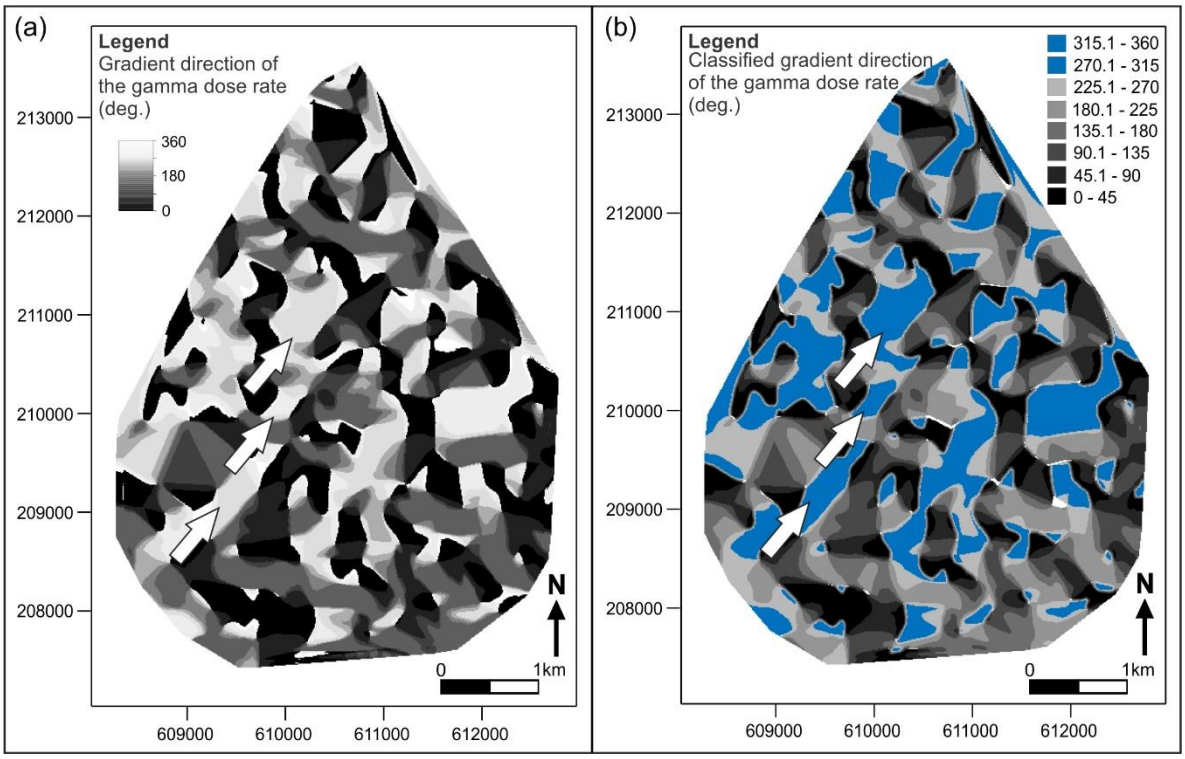

Figure 20. Gradient direction analysis of the gamma dose rate measured at the surface is presented in a) grey scale shading map and b) classified map in 45-degree classes. Solid white arrows indicate the SW-NE oriented linear edges. The zero-degree direction is the North.

The profile curvature map shows the spatial location of the sudden changes in the gradient magnitude of gamma dose rate (Figure 21). Negative and positive values correspond to convex ('ridges') and concave ('valleys') zones, respectively (Jordan, 2007). Convex features like ridges (i.e., positive gamma dose rate anomalies) have SW-NE orientation and they form a left stepping en-echelon pattern. Classified profile curvature map in Figure 21b enhances the SW-NE oriented linear edges of convex features, emphasized by solid white arrows, which are parallel to the main dike orientation.

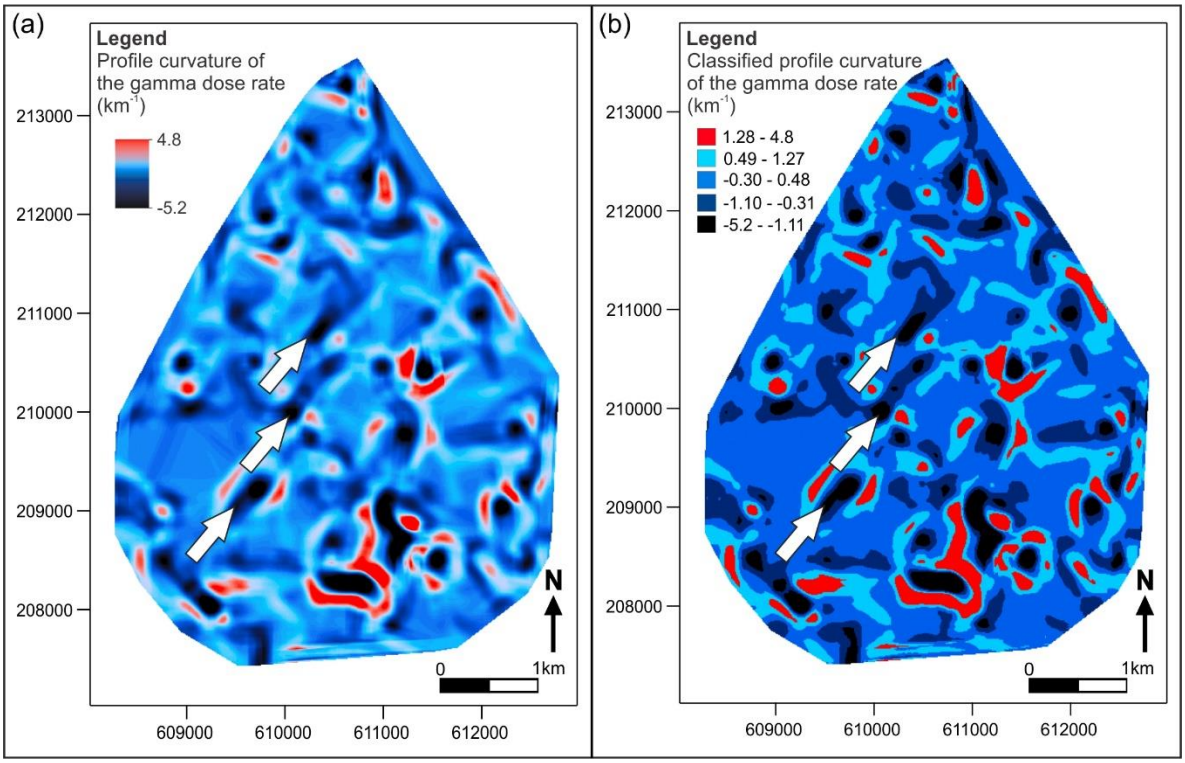

Figure 21. Profile curvature analysis for the measured gamma dose rate at the surface is presented in a) color scale map and b) classified map. White arrows indicate the dominant profile curvature direction SW-NE parallel to the main dike orientation. Positive values correspond to concave surface points and negative values to convex surface points, respectively.

The sudden changes in gamma dose rate are represented by the lineaments (Figure 22a), identified from the shaded relief maps of gamma dose rate (Figure 16a). The lineament density map shows the spatial distribution of the lineaments in the study area. The highest total length of lineaments per unit area can be found in the southern part (Figure 22a), where the highest variability and dike density were also identified (Figure 17 and 18). Frequency and length, based rose diagrams of lineaments, reveal two main orientations: SW-NE and SE-NW indicated by grey shading in Figure 22b. Similar evaluation was performed on the orientation of faults and dikes of the study area extracted from the 1:25,000 scale geological map of Velence Hills (Horváth et al., 2004) (Figure 13b). The main orientation of faults is SE-NW, whereas the main orientation of dikes is SW-NE (Figure 22c), which corresponds to the extensive structural measurements on granite porphyry and quartz dikes and joints made by Benkó et al. (2014) in Velence Hills (Figure 22d). Concluding, the gamma dose rate sudden changes represented by lineaments having the same directions as the faults and

granite prophyre dikes. The N-S and E-W directions in the rose diagram cannot be explained at this point of the research.

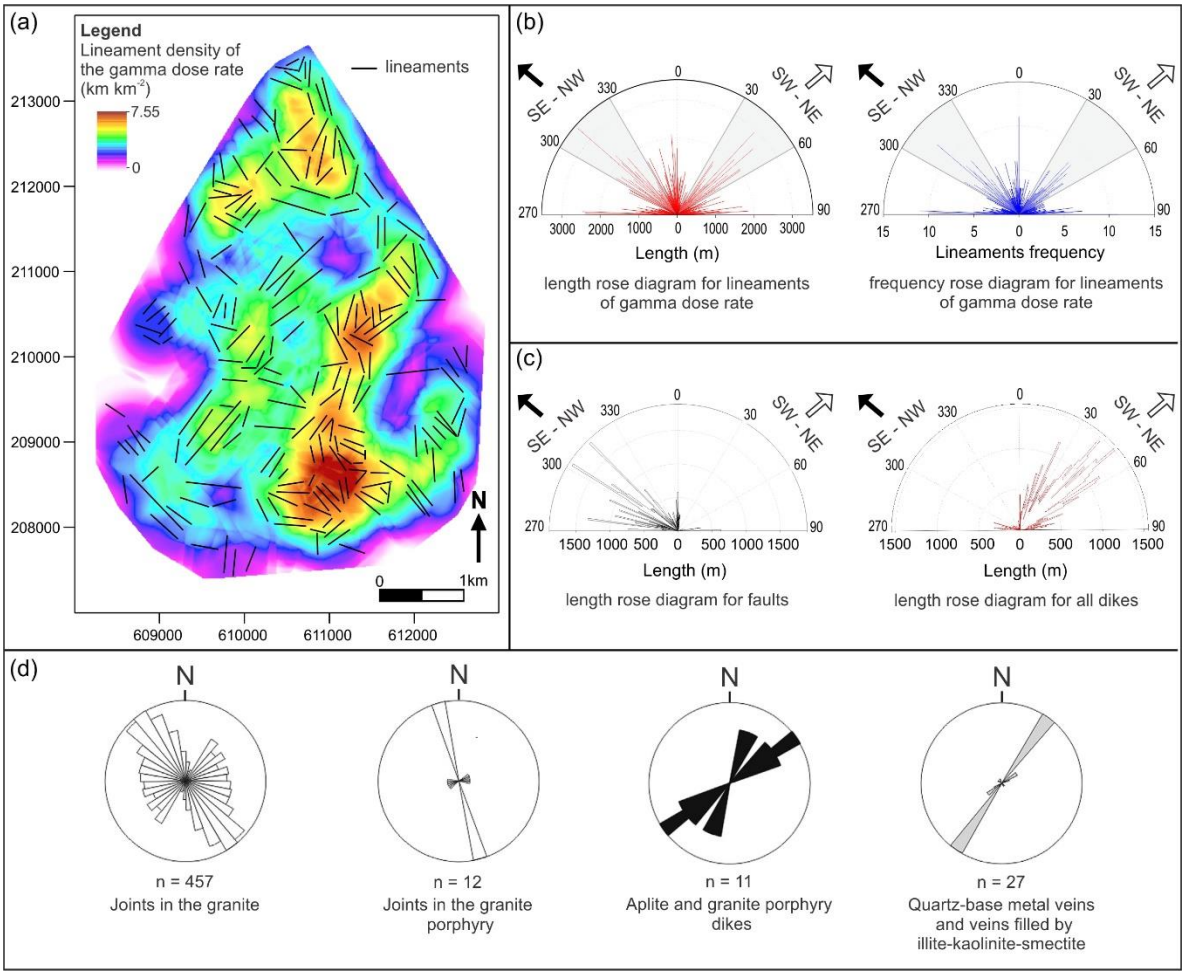

Figure 22. Lineament analysis for the measured gamma dose rate at the surface. a) Color scale lineament density map of gamma dose rate. b) Length and frequency rose diagrams for the measured gamma dose rate lineaments. c) Length rose diagram for all types of dikes and faults. d) Orientation of dikes, hydrothermal veins and joints in the studied area according to Benkó et al. (2014).

7.2. Results of geogenic radon potential evaluation

The measured parameters (soil gas radon activity concentration and soil gas permeability) were averaged at each sampling site, from its three replicates, to ensure its representativity.

7.2.1. Field measurements

The summary statistics for field measured soil gas permeability and soil gas radon concentration at 30 sampling sites are detailed in Table 6, as well as calculated GRP applying the Eq. 11 proposed by Neznal et al. (2004) for the field measured input parameters.

Table 6. Summary statistics of the field measured parameters (n=30)

	Min.	Max.	Mean	Median	STDEV
soil gas permeability (m^2)	2.15E-12	2.03E-12	3.92E-13	1.45E-12	3.00E-12
total soil gas radon concentration (Bq m^{-3})	13400	94900	30303	26050	16340
soil gas radon (^{222}Rn) concentration (Bq m^{-3})	6100	27500	13150	13150	4526
soil gas thoron (^{220}Rn) concentration (Bq m^{-3})	4400	67400	17153	13700	12256
GRP	3.70	18.60	7.94	7.65	3.04

The meteorological conditions of the field measurements are shown in Table 7, carried out in July from 7:00 to 19:00. Thus, the range of temperatures corresponds to the natural variability during the daytime in summer. The range of pressures is quite narrow varying only 11 hPa. The median measurement depth is 0.89 m. The minimum depth corresponds to the sampling site 11, where the underlying granitic rock were found at 0.76 m because this sampling site is the closest to the top of the hill (Figure 7 and Figure 30).

Table 7. Summary statistics of measurement conditions (n=30)

	Min.	Max.	Mean	Median	STDEV
ambient temperature (°C)	23.7	40.4	31.8	32.2	4.89
ambient absolute pressure (hPa)	975	986	980	980	3.32
ambient relative humidity (%)	24	55	38.5	38	8.85
depth (m)	0.76	0.92	0.88	0.89	0.03

Since the field measurements were performed in similar conditions to avoid the effect of seasonal and daily variation of radon there is no correlation between the field measured soil gas radon concentration and the meteorological conditions.

Composite representation of descriptive statistics is on the Figures 23a, 25a and 27a, where in the upper side, the histogram is overlaid with the cumulative density function (CDF) that gives a clear idea of the distribution of the correspondent evaluated parameter. The bottom box-and-whiskers plot shows the position of the median value and an indication of the existence of outliers. Overlaid to the box-and-whiskers plot, the scatter plot, with the scale alienated to the upper plot, shows the number of measurements corresponding to the respective bin of the histogram. In the same sense, Figures 23b and 25b show the field measured parameter at each sampling site where the error bar represents the standard deviation from the three replicates.

The field measured soil gas permeability presents a bimodal distribution (Figure 23) and its median is within the range of uniform fine sand and well graded silty sand according to typical soil permeabilities shown in Figure 4.

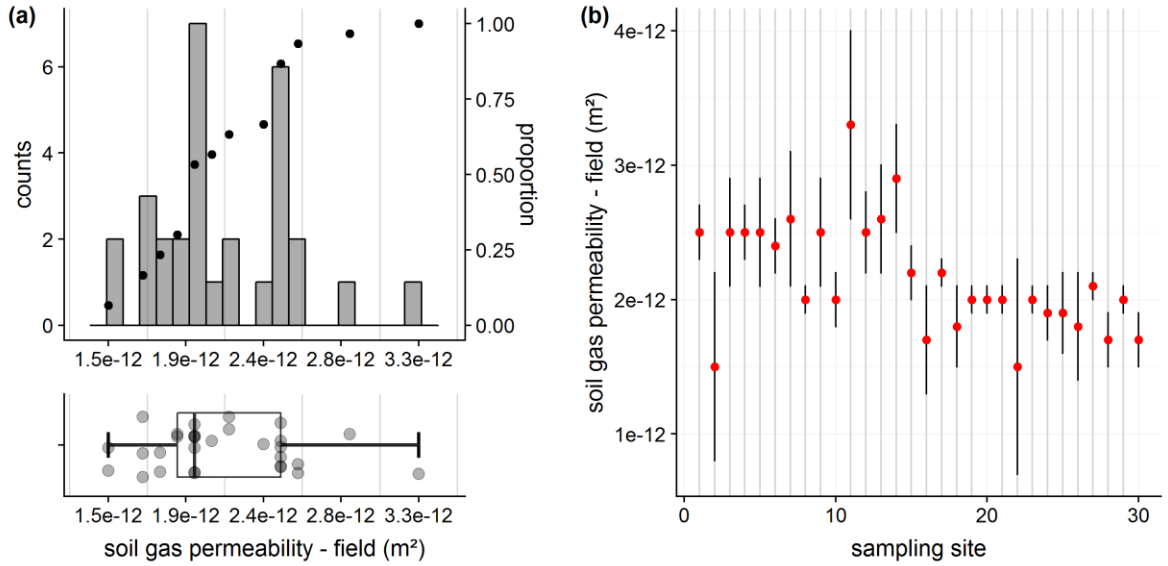

Figure 23. a) Descriptive statistics diagram showing the histogram (overlaid by the cumulative density function) and box-and-whiskers plot (overlaid by the scatter plot), and b) scatter plot of field measured soil gas permeability at each sampling site, where the error bar represents the standard deviation from the three replicates.

Since the study area is located in a slope the variability of the soil thickness together with the local geology (angular debris, slope deposits, clay and sand) contributes to the variability and heterogeneity in the distribution of the soil gas permeability (Figure 23).

For illustration purposes, a color code is used for the classification of soil gas permeability, soil gas radon concentration and geogenic radon potential (GRP) as follows: yellow for low, blue for medium and red for high classes based on the classification proposed by Neznal et al. (2004) (Figure 26 and Figure 27). Applying this classification for the field measured soil gas permeability, all measurements are in the range of $4x10^{-13}$ - $4x10^{-12}$ m^2, which correspond to the medium class (yellow). The spatial distribution of soil gas permeability over the geological map 1:25000 scale (Horváth et al., 2004) (Figure 26a) the radius of the circles are proportional to the permeability scale ranges as showed in the legend.

The total soil gas radon (^{222}Rn and ^{220}Rn) varies in a wide range (see Table 6) within the measured sites. The $^{220}Rn/^{222}Rn$ ratio varies from 0.38 to 2.45, reflected in Figure 24, showing the soil gas radon and thoron concentrations at each sampling site. The sampling site 11 presents the highest radon and thoron concentration (Table 6) (Figure 25), where the thickness of the soil is lower than 80 cm (Table 7). Therefore, the elevated values in radon and thoron concentration in this sampling site can be attributed to the rock contribution.

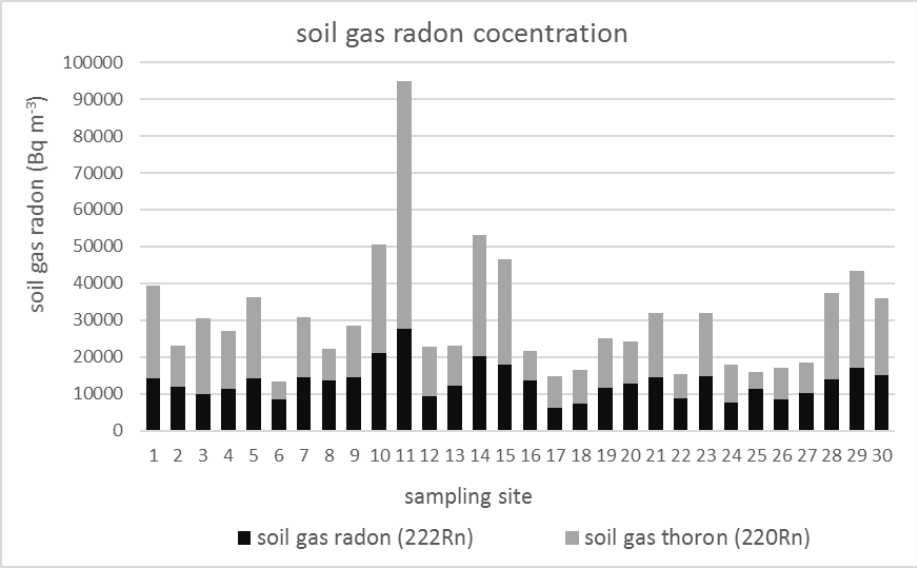

Figure 24. Field measured soil gas radon (^{222}Rn) and thoron (^{220}Rn) concentration.

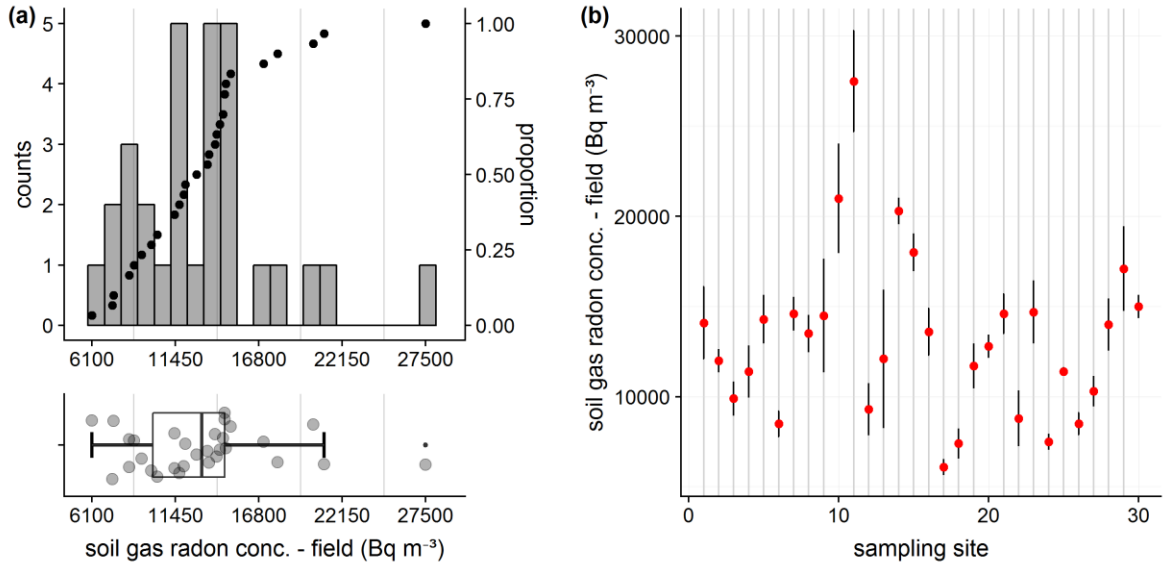

Figure 25. a) Descriptive statistics diagram showing the histogram (overlaid by the cumulative density function) and box-and-whiskers plot (overlaid by the scatter plot), and b) scatter plot of field measured soil gas radon concentration at each sampling site, where the error bar represents the standard deviation from the three replicates.

The sampling site 11, constitutes an extreme value in the statistical distribution of soil gas radon concentration as it is shown in Figure 25. The spatial distribution of soil gas radon concentration over the geological map (Figure 26b) shows its variability within the range of 6100 to 27500 Bq m^{-3} (Table 6). Based on the medium soil gas permeability and applying the classification proposed by Neznal et al. (2004) (Table 3), the corresponding categories for soil gas radon concentration is as follows: low for values smaller than 20 000 Bq m^{-3}, medium in the range of 20 000 to 70 000 Bq m^{-3} and high for values greater than 70 000 Bq m^{-3}. Therefore, the field measured soil gas radon concentration belongs mostly to the low category (blue), except three sampling sites, including the extreme values, corresponding to the sampling site 11 that belongs to the medium category (yellow) (Figure 26b). Considering the median as a representative central value indicator for the 30 measured sites, the soil gas radon concentration (median: 13 700 Bq m^{-3}) (Table 6) in the study area belongs to the low category.

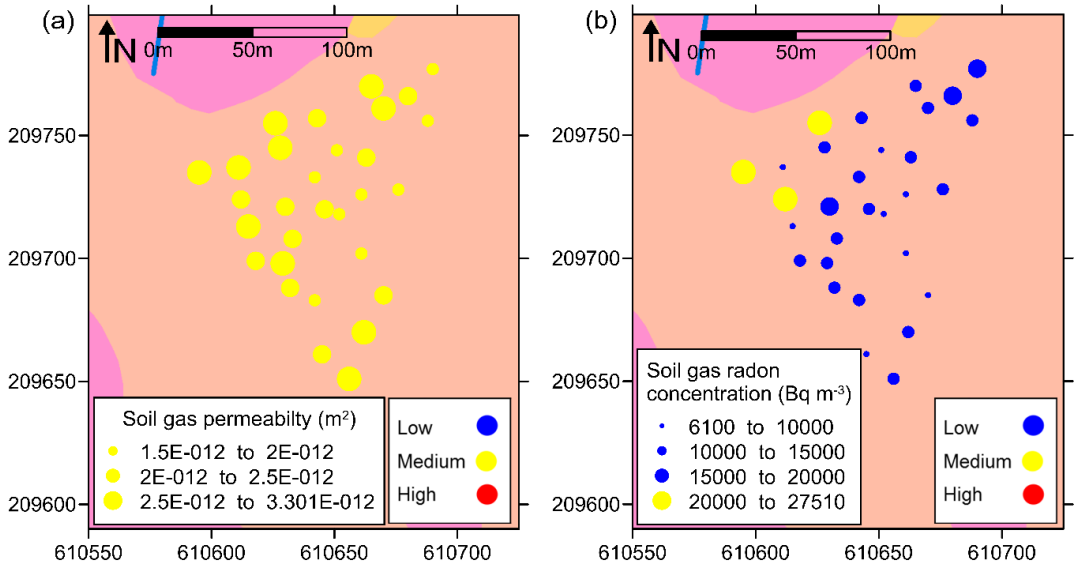

Figure 26. Spatial distribution of the field measured soil gas permeability and soil radon concentration over the geological map.

The geogenic radon potential (GRP) calculated for the field measurement input parameters applying Eq. 11 (Neznal et al. 2004) for each sampling site is shown in Figure 27b. The GRP is directly proportional to the field soil gas radon concentration; therefore, they show similar distribution. The extreme value corresponds to the sampling site 11 (Figure 27a).

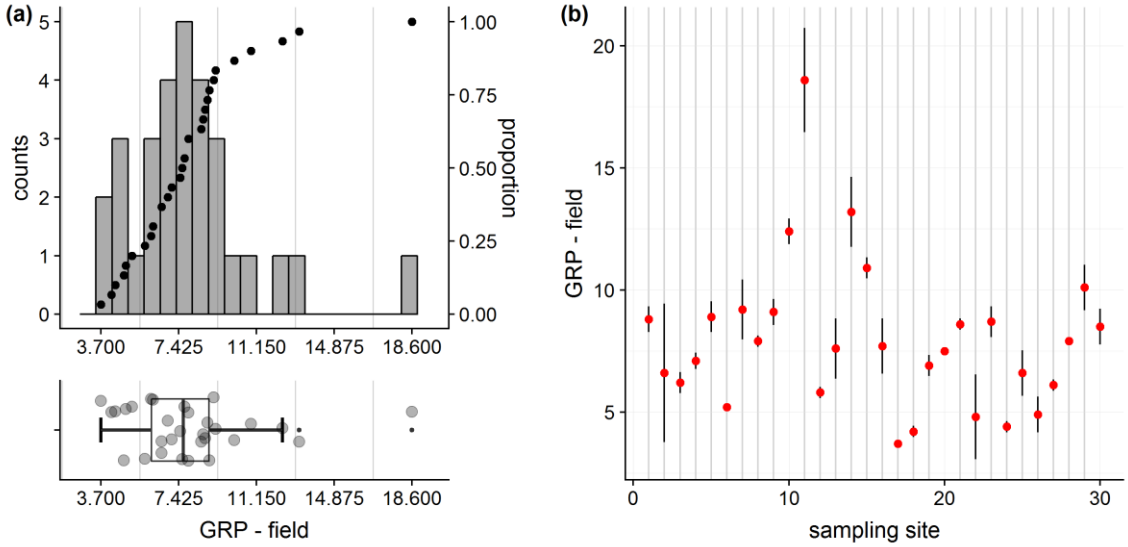

Figure 27. a) Descriptive statistics and b) scatter plot of geogenic radon potential (GRP) calculated with the field measured parameters at each sampling site where the error is calculated by the error propagation formula based on Taylor's series.

Applying the classification proposed by Neznal et al. (2004) (Table 3), the categories for GRP are as follows: low for values lower than 10, medium for values between 10 and 35 and high for values greater than 35.

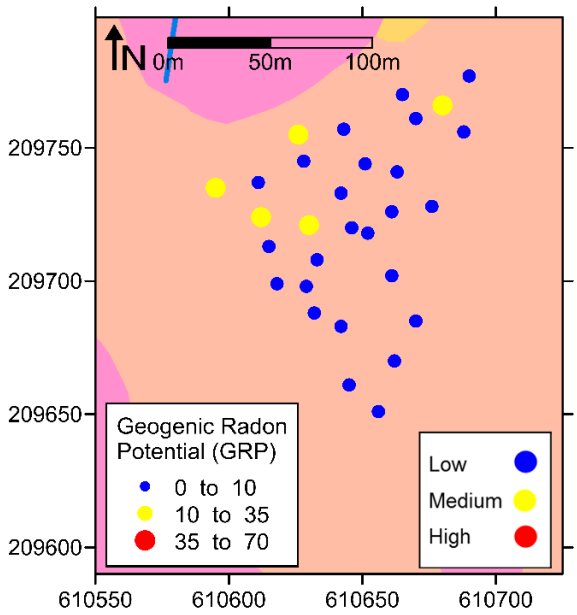

Figure 28. Spatial distribution of the geogenic radon potential (GRP) from the field measured parameters showing low and medium categories.

Within the study area, most of the measurements low (25 sampling sites) corresponds to the low category (Figure 28) and low median value (Table 6).

7.2.2. Soil properties

As the initial step the study area was evaluated in terms of soil gas radon concentration and soil gas permeability based on field measurements, subsequently calculated the geogenic radon potential (GRP) and characterized by applying the classification proposed by Neznal et al. (2004) (Table 3). In order to apply the above described theoretical models for the determination of soil gas radon concentration and soil gas permeability, the soil properties, involved in the model and the influencing parameters in radon production, and emanation and migration processes was determined by laboratory analyses. Summary statistics for the determined soil parameters are listed in Table 8 and descriptive statistics and scatter plots are detailed in Annex I.

Table 8. Summary statistics of the physicochemical characteristics of the studied soil (n=30)

	Min.	Max.	Mean	Median	STDEV
bulk density dry soil (kg m^{-3})	1430	1690	1573	1580	64.76
bulk density dry soil (kg m^{-3})	1500	1800	1647	1650	73.67
gravimetric water content (%)	2.80	8.97	4.71	4.63	1.32
volumetric water content (%)	4.10	14.80	7.40	7.30	2.13
volume fraction of water saturation	0.09	0.39	0.19	0.19	0.06
total porosity	0.36	0.46	0.407	0.40	0.03
effective porosity	0.26	0.42	0.35	0.35	0.04
air filled porosity	0.23	0.41	0.33	0.34	0.04
pH distilled water	6.10	9.20	8.52	9.00	0.84
pH KCl	5.00	8.20	7.38	7.90	0.90
carbonate content (%)	0.00	16.70	8.31	9.40	6.24
organic material content (%)	0.03	0.67	0.28	0.24	0.17

The bulk density of the dry soil, determined for the measured sites, varies in the range of 1430 and 1690 kgm^{-3} without outlying values (Figure a 1). The gravimetric content within the study area varies in a wide range (Table 6) and shows two outliers above 7 % that corresponds to the sites 7 (7.43 %) and site 11 (8.97 %) (Figure a 2). Based on the range of soil total porosity of the study (Table 6), it corresponds to the range of fine sand without outlying values. Since the soil water saturation conditions are function of both water content and total porosity, one outlying value was found among the measured site that corresponds to the site 15 (Figure a 4). At this site, volume fraction of the water saturation is 0.39, whereas all the other values are below 0.25 and the median is 0.19 (Table 6). Soil pH determined in distilled water has a heterogeneous distribution, where two groups can be distinguished (Figure a 5): the first one between 6.1 to 7.7, only sampling site 30 has acidic pH, whereas all the remain sampling sites show a range of pH between 8.2 to 9.2. As it is expected this groups are reflected in the carbonate content distribution, noticing the same marked groups: the first one < 3.83 m/m % (for 9 sampling sites) and the second one > 6.2 m/m % (for 11 sampling sites). Organic material content is heterogeneously distributed among the sampling sites (Figure a 7). Despite no outlying values can be distinguished in the box-and-whiskers plot it is important to mention that the sampling site 14 shows the highest organic material content (0.67 m/m %).

As it was described in the section 6.2.5, the particle size distribution was determined by two methods: dry sieving (from 6.3 to 0.063 mm) by sedimentation (for this method DS-SED is used in this section) and dry sieving (from 6.3 to 2 mm) by laser diffraction (for this method DS-LD is used in this section). From the grain size distribution, the arithmetic mean, geometric mean and the median particle diameter were determined for both methods, respectively. By comparison of medians (Table 9), the values of particle size obtained from dry sieving - sedimentation method are overestimated compared to the values obtained by dry sieving - laser diffraction in different percentage. Arithmetic mean diameter is overestimated in 81 %, the geometric mean diameter in 63 % and the median diameter in 14 %. Arithmetic mean diameter is applicable for a normally distributed grain size. The soil samples from the study area present a lognormal distribution. An example of this is shown in Annex II. which is the grain size distribution for the sampling site 1. Therefore, the arithmetic mean is not representative for the particle size in this study. This confirms that the median diameter is a robust indicator with slightly influence of the method applied for the particle size determination. Due to the known accuracy of the laser diffraction method, the results obtained by DS-LD are used for the determination of the particle size diameter.

Table 9. Particle diameter determined form the particle size distribution measured by dry sieving – sedimentation and dry sieving laser diffraction, (n=30)

method	particle diameter (mm)	Min.	Max.	Mean	Median	STDEV
dry sieving - sedimentation DS-SED	arithmetic mean	0.297	1.937	0.627	0.557	0.346
	geometric mean	0.187	0.468	0.284	0.272	0.067
	median	0.189	0.358	0.231	0.218	0.040
dry sieving - laser diffraction DS-LD	arithmetic mean	0.094	1.077	0.378	0.308	0.218
	geometric mean	0.094	0.346	0.168	0.167	0.055
	median	0.142	0.255	0.196	0.192	0.024

Sand, silt and clay fractions were determined for the soil samples under 2 mm by the dry sieving - sedimentation (DS-SED) and compared to the dry sieving - laser diffraction method (DS-LD). For the evaluation of this results, the values obtained by laser diffraction will be considered the reference level due to its accuracy and reproducibility in the determination of the particle size distribution.

Table 10. Sand, silt and clay grain size fractions determined by dry sieving – sedimentation and laser diffraction (n=30)

Method	Fraction (%)	Min.	Max.	Mean	Median	STDEV
dry sieving - sedimentation DS-SED	sand	65.20	93.29	83.75	85.94	7.63
	silt	1.90	18.94	7.85	6.53	4.50
	clay	4.81	16.13	8.40	7.46	3.32
laser diffraction DL	sand	50.94	97.27	79.63	82.07	11.83
	silt	1.38	40.57	15.41	13.55	10.16
	clay	1.36	8.50	4.97	4.56	1.82

The results (Table 10) indicates an overestimation of the clay fraction in 64 % comparing the corresponding median values and underestimates the silt fraction in 48 %, based on the median values (Figure 29). Additionally, to the overestimation of the DS-SED method in the clay fraction, showing 5 outlying values, which are not present in the clay distribution by LD. This makes less reliable the DS-SED method as it is demonstrated in the literature (Ferro and Mirabile, 2012; Konert and Vandenberghe, 1997; Li et al., 2005). Therefore, values of sand, silt and clay fractions determined by laser diffraction are used in this thesis.

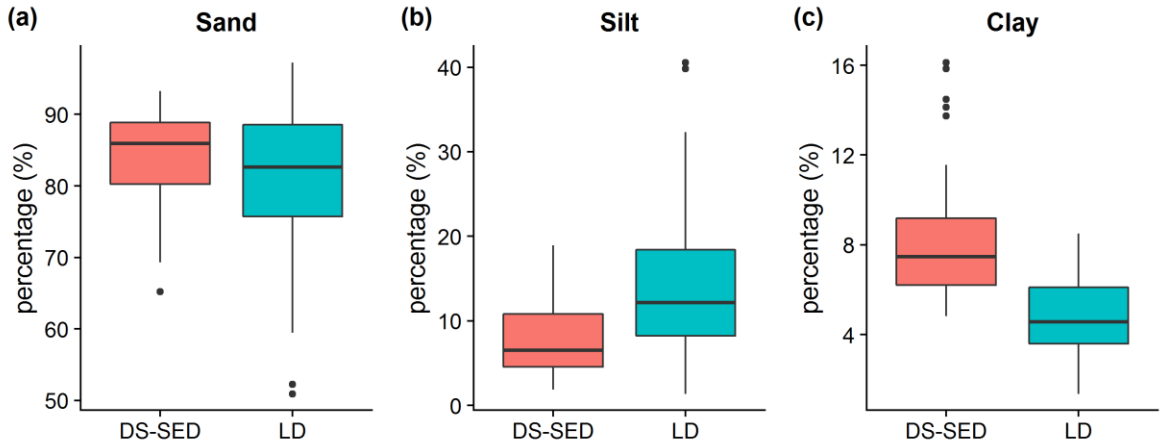

Figure 29. Sand, silt and clay grain size fractions determined by dry sieving – sedimentation (DS-SED) and laser diffraction (LD) used for the determination of grain size distribution.

The determination of the radioactive content of the soil is fundamental in the evaluation of the geogenic radon potential. The activity concentration of uranium, thorium, radium and potassium of the soil samples at 0.89 m median depth varies in a wide range (Table 11).

These values are smaller than the average activity concentration for the surficial Hungarian soils published by UNSCEAR (2000) (Table 1).

Table 11. Summary statistics of the activity concentration radionuclides and radon exhalation and emanation of the soil (n=30)

	Activity concentration in Hungarian soils (UNSCEAR, 2000)	Min.	Max.	Mean	Median	STEDV
radon exhalation (mBq $kg^{-1}h^{-1}$)	-	0.40	53.70	20.77	15.40	15.95
radon emanation coefficient	-	0.011	0.245	0.105	0.098	0.065
Ra-226 (Bq kg^{-1})	33	9.40	28.01	17.35	17.00	4.95
U-238 (Bq kg^{-1})	29	2.06	35.39	12.24	11.47	7.71
Th-232 (Bq kg^{-1})	28	7.07	32.12	16.32	15.43	6.31
K-40 (Bq kg^{-1})	370	198.92	454.02	274.57	258.75	66.56

The bulk chemical composition was determined for 7 soil samples, listed and described in Table 12 and Table 13, with a decreasing soil gas radon concentration from left to right, along a slope (elevation from 180 to 170 m above sea level) located at the cross-section AB (Figure 30). Because of the variability of soil gas radon concentration among them, its chemical composition is associated to determined soil properties (Table 12 and Table 13).

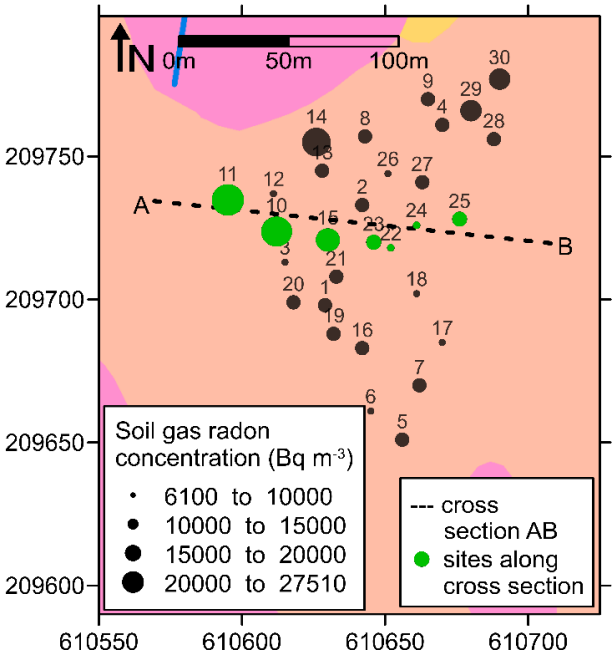

Figure 30. Cross-section AB along the slope that involves 7 sampling sites (green dots) with decreasing soil gas radon concentration profile (radius of the dots proportional to the soil gas radon concentration) from A (180 m a.s.l.) to B (170 m a.s.l.).

For this, the correlation coefficient is used as a reference, but the significance is not shown due to the low number of samples (n=7). Based on the chemical composition of the common uranium- and thorium-bearing minerals in granitic rock (Table 1), their major chemical compositions are shown in Table 12. On this sense, zirconium is associated to the zircon ($ZrSiO_4$) content of the soil sample, in the same way, yttrium represents xenotime (YPO_4) and cerium, in turn, does monazite ($CePO_4$) content of the soil sample. The weak correlation (r=0.55) between soil gas radon concentration and zirconium can be explained by the low radon emanation coefficients attributed to the zircon grains (Cothern and Smith, 1987) that are different of the soil radon emanation that has a strong correlation with the soil gas radon concentration (r=0.82).

Table 12**.** Elemental composition (U, Th, Zr, Y, Ce, La, Rb, Al), clay fraction by laser diffraction LD, pH value, soil gas radon concentration and radon emanation of seven soil samples (see Figure 30) associated to the geochemical behavior of radon and its geogenic sources.

sampling site	soil gas ^{222}Rn (Bq m^{-3})	radon emanation coefficient	^{226}Ra (Bq kg^{-1})	U (ppm)	Th (ppm)	Zr (ppm)	Y (ppm)	Ce (ppm)	La (ppm)	Rb (ppm)	Al (%)	clay LD (m/m %)	soil pH in water
10	21000	0.16	21.84	1.1	6.7	1.3	11.55	37.4	19.5	6.3	0.61	3.56	9.2
11	27500	0.151	28.01	1.3	8.3	1.3	16.38	50.1	27.7	13	1.05	5.51	7.4
15	18000	0.191	22.68	0.8	8.1	2.3	13.6	46.3	23.4	25.8	1.61	6.61	7.2
22	8800	0.068	18.01	0.9	4.2	0.8	9.28	25.3	13.4	6.8	0.64	3.00	9.2
23	14700	0.163	15.58	0.7	4.6	0.9	9.96	30.3	15.8	12.8	0.88	3.83	7.6
24	7500	0.013	17.26	1.0	4.9	0.7	10.05	31.0	16.5	7.0	0.71	3.25	9.1
25	11400	0.134	17.25	1.0	4.7	0.6	10.38	31.2	16.1	9.8	0.82	3.47	9.1

Table 13. Physical and chemical soil properties associated with the geochemical behavior of radon and its geogenic sources.

Site	soil gas ^{222}Rn (Bq m^{-3})	radon emanation coefficient.	^{226}Ra (Bq kg^{-1})	Carbonate content (m/m %)	Ca (m/m %)	Mg (m/m %)	soil pH in water	organic material (m/m %)	volume fraction of water saturation	total porosity	sand LD (%)	silt LD (%)	clay LD (%)
10	21000	0.16	21.84	13.1	6.7	1.3	9.2	0.24	0.16	0.42	90.8	5.67	3.56
11	27500	0.151	28.01	0	0.3	0.2	7.4	0.4	0.12	0.4	77.5	17	5.51
15	18000	0.191	22.68	0	0.3	0.4	7.2	0.54	0.39	0.38	73.4	20	6.61
22	8800	0.068	18.01	11.2	6.8	1.3	9.2	0.12	0.19	0.39	88.9	8.11	3
23	14700	0.163	15.58	0	2	0.5	7.6	0.19	0.19	0.41	84.8	11.3	3.83
24	7500	0.013	17.26	14.2	8.2	1.4	9.1	0.12	0.21	0.4	84.5	12.3	3.25
25	11400	0.134	17.25	15.4	8.1	1.4	9.1	0.43	0.22	0.38	80	16.6	3.47

Under oxidizing conditions and acidic pH, uranium as uranyl ion $(UO_2)^{2+}$ is mobile, therefore it can migrate by forming solutions (Eh-pH diagram of the system U-C-O-H) (Takeno, 2005). Thus, it explains the weak correlation of uranium (r=0.54) with the soil gas radon concentration. On the other hand, yttrium, cerium (and lanthanum) show strong correlation with the soil gas radon concentration (r_Y=0.88, r_{Ce}=0.86, r_{La}=0.88) that is clear indication of the content of xenotime and monazite minerals in the soil. The correlation between these minerals and the clay fraction is also strong (r_Y=0.82, r_{Ce}=0.88, r_{La}=0.84) that means that the clay fraction might be enriched in these uranium bearing phosphate minerals.

The content aluminum (a major element in clay minerals) and rubidium (a trace element commonly adsorbed in clay minerals) is associated to the content of clay mineral in the soil sampling sites, since rubidium it is strongly sorbed by clay minerals such as illite under acidic conditions and aluminum is a part of kaolinite. The correlation of rubidium and aluminum with clay fraction ($r_{Rb-clay}$=0.91, $r_{Al-clay}$=0.94) suggests the content of clay minerals in the finest fraction (lower than 0.008 mm).

The influence of the physical and chemical soil properties on the soil gas radon concentration by correlation for the 7 selected samples based on the values of Table 13. As it is expected, the determined carbonate content of the soil samples is strongly correlated with the concentrations of calcium and magnesium independently (r=0.98 in both cases). Despite the weak negative correlation between soil gas radon concentration and carbonate content (r= 0.58), it can be noticed that in the sampling sites, where the carbonate content is zero (pH < 8), the radon emanation coefficient is the highest (sites11,15, 23) (Figure 30). This relationship was found in 9 sampling sites out of the 30 measured (Table 16). Additionally, the emanation coefficients are not in direct connection with radium activity concentration, total porosity, amount of sand and clay fraction and organic content in these three samples. Sample 15 has the highest gravimetric water content (8.97 %) and its total porosity (0.38) indicates the saturation conditions. These conditions must have been depended on the organic material content (0.54 %), which reflects on the radium content in the clay fraction. Based on this detailed analysis, it can be noticed that the complexity of the soil processes influences directly or indirectly the soil gas radon concentration.

7.2.3. Soil factors influencing on soil gas permeability and soil gas radon concentration

Influence of factors, involving radon generation and migration through the soil pores, is evaluated by a correlation test. The correlation coefficient and the statistical significance are included in the correlation plot.

7.2.3.1. Influencing factors on soil gas permeability

Permeability is an important factor in radon migration through soil pores (Figure 3). As a summary of section 4.3, it can be affirmed that factors influencing the soil gas permeability are: soil porosity effected by water content and grain size of the soil. Based on this general statement, a detailed correlation analysis was performed between the field measure soil gas permeability and the different types of porosity (total, effective and air filled porosity), the different ways to express water content (gravimetric percentage or in terms of volume fraction of water saturation) and the particle diameter determined by laser diffraction (arithmetic, geometric and median particle diameter).

The results of this correlation test are summarized in Table 14, represented by the correlation coefficient and the statistical significance under 95 % of confidence interval for the 30 sampling sites.

Table 14. Correlation between field measured soil gas permeability and its influencing factors (n=30)

soil parameters		correlation coefficient (r)	statistical significance (p)
porosity	total porosity	0.001	0.994
	effective porosity	**0.324**	**0.081**
	air filled porosity	0.241	0.2
water content (%)	**volume fraction of water saturation**	**-0.371**	**0.043**
	gravimetric water content	**-0.459**	**0.011**
particle diameter (mm)	arithmetic mean	0.08	0.676
	geometric mean	-0.108	0.342
	median	-0.09	0.635

There is no significant correlation between the measured soil gas permeability and the particle size diameter, neither with total porosity nor air filled porosity. Although the correlation between soil gas permeability and effective porosity is not significant, there is a clear tendency to positive correlation as shown in Figure 31a. Since the sampling site 15 is the only one, which has saturation conditions, it was removed from the data and the correlation was recalculated.

By excluding sampling site 15 (labeled in Figure 31), the correlation between soil permeability and effective porosity increases slightly to r =0.379 and became significant (p=0.043) but still weak correlation. Whereas, the negative correlation of soil gas permeability and volume fraction of water saturation improves significantly with r=-0.513 and p=0.04. Besides this improvement, the correlation with these two parameters is not strong but still significant.

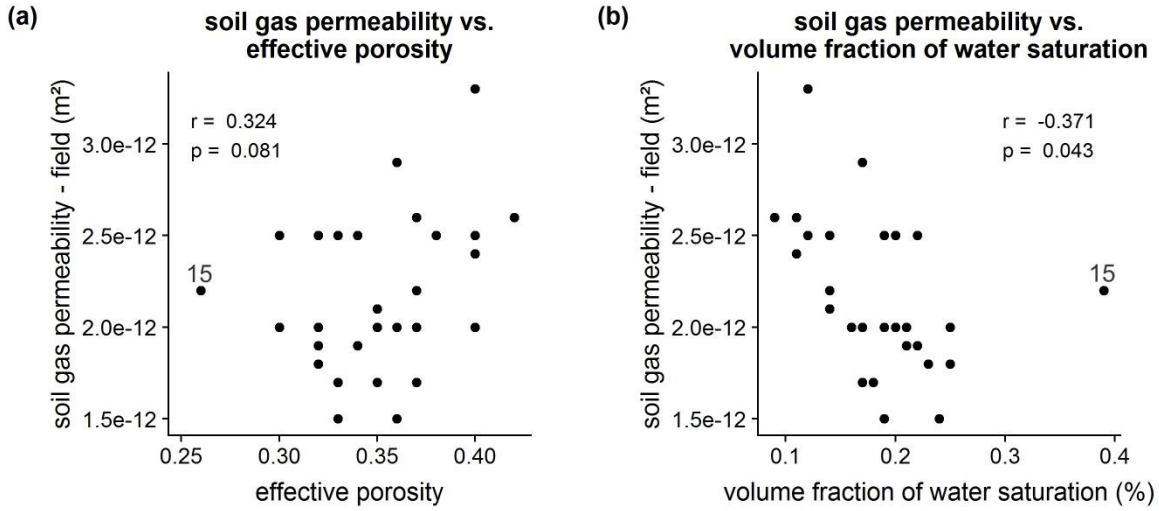

Figure 31. Correlation plots a) between field measured soil gas permeability and b) effective porosity and volume fraction of water saturation.

7.2.3.2. Influencing factors on radon generation process

Following the process of radon availability and migration in soil (Figure 3), the first step is radon generation. The influencing factors: geochemical process and radium activity concentration. Based on the geochemical behavior of radium, detailed in section 2.2.4.5, it can be summarized that in case of absence or low concentration of calcium (from $CaCO_3$)

radium is preferentially adsorbed on organic material and clay minerals (Nathwani and Phillips, 1979a). According to Greeman and Rose (1996), the emanation coefficient of minerals coated by organic material is two times higher than the clays. The evaluated influencing factors are: clay fraction, particle diameter, organic material content and pH. The correlation coefficients and statistical significance of correlations of those factors whose radium activity concentration are shown in Table 15.

Table 15. Correlation between radium concentration and its influencing factors (n=30)

soil parameters correlated with radium activity concentration	**correlation coefficient (r)**	**statistical significance (p)**
median particle diameter (mm)	-0.158	0.405
clay fraction (%)	0.26	0.165
organic material content (%)	**0.437**	**0.016**
pH	**-0.437**	**0.016**

The particle grain size does not correlate with radium concentration, considering all sampling sites (Table 15), however it can be noticed a positive correlation with excluding of 6 sampling sites demonstrated in Figure 32a. The radium concentration, in the including samples, can be related to the proximity of the underlying bedrock to the sampling site, which is clearly shown in the geographical location of sampling sites 11 and 14 (Figure 7 and Figure 30). There is not significant correlation between radium content and clay fraction (Figure 32b). Whereas, the organic material content has a significant positive correlation with radium concentration, despite the presence of bivariate outlying values sampling sites 11 and 27 (Figure 32c).

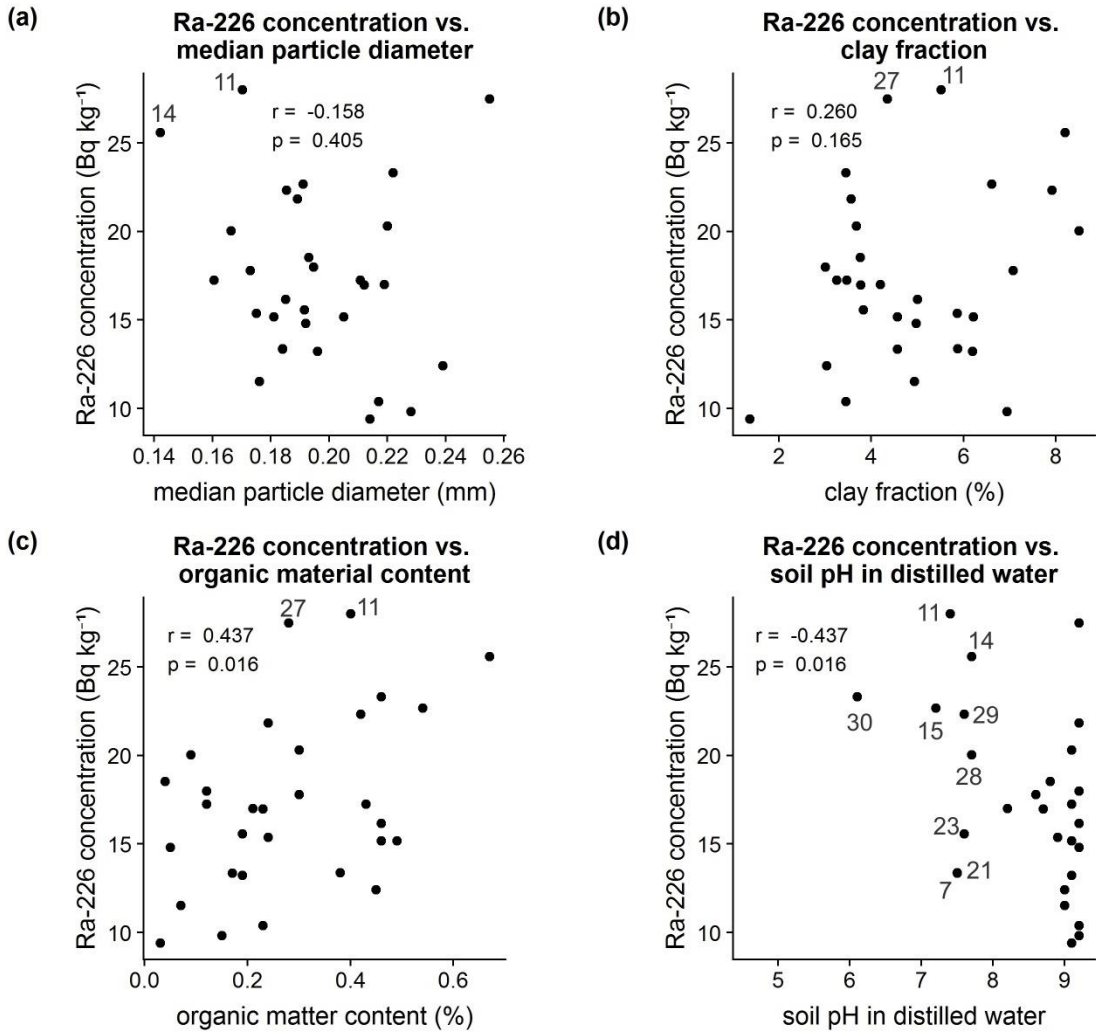

Figure 32. Correlation between Ra-226 concentrations and influencing parameters: a) grain size, b) clay fraction, c) organic matter and d) pH of soil.

A special distribution of the sampling sites in the correlation plot between ^{226}Ra and soil pH in distilled water is shown in Figure 32d. Besides the significant correlation shown in the plot (Figure 32d), two groups of sampling sites can be distinguished around pH=8. The sampling sites that belongs to group in the range of pH from 6.1 to 7.7 corresponds to the sites where the carbonate content is zero or close to zero as it is detailed in Table 16. For the sampling points listed in Table 16, it can be noticed that almost all soil samples have the highest radon emanation coefficient among the 30 sampling sites. Most of the sampling sites indicated in Table 16 have values of radon emanation greater than the median (0.098) of the 30 sampling sites (Table 11), except sampling site 28, which has the lowest organic content

but the highest clay content among the soils in Table 16. This is explained by the geochemical behavior of radium, which is preferentially adsorbed on organic material and clay minerals in absence or low concentration of calcium (from $CaCO_3$) (Nathwani and Phillips, 1979a,b). According to Greeman and Rose, 1996, the emanation coefficient of minerals coated by organic material is two times higher than the clays that is reflected in Table 16.

Table 16. Soil properties at pH < 8

sampling site	222-Ra (Bq kg^{-1})	radon emanation coefficient	carbonate (%)	soil pH in distilled water	organic material (%)	clay LD (%)	total porosity
7	13.38	0.166	0	7.5	0.38	5.87	0.45
11	28.01	0.151	0	7.4	0.4	5.51	0.4
14	25.59	0.136	3.33	7.7	0.67	8.2	0.41
15	22.68	0.191	0	7.2	0.54	6.61	0.38
21	13.36	0.245	0	7.5	0.17	4.56	0.41
23	15.58	0.163	0	7.6	0.19	3.83	0.41
28	20.04	0.073	0	7.7	0.09	8.5	0.39
29	22.35	0.221	0	7.6	0.42	7.92	0.43
30	23.33	0.164	0	6.1	0.46	3.45	0.43

The preferential adsorption of radium in organic material was not found at pH > 8 within the measured sites. Since at high pH, the carbonate content increases due to the competition between radium and calcium, in this case the affinity of the organic material is not significant. Note that the preferential adsorption of radium in clay minerals is not modified under these conditions(Nathwani and Phillips, 1979b, 1979a; Sposito, 2008; Thorne and Mitchell, 2011).

7.2.3.3. Influencing factors on radon emanation process

As it was detailed in section 4.1.6.4. that, at environmental conditions, the influencing factors on radon emanation are particle size and water content. The correlation plots as well as the correlation coefficient and its significance are shown in Figure 33.

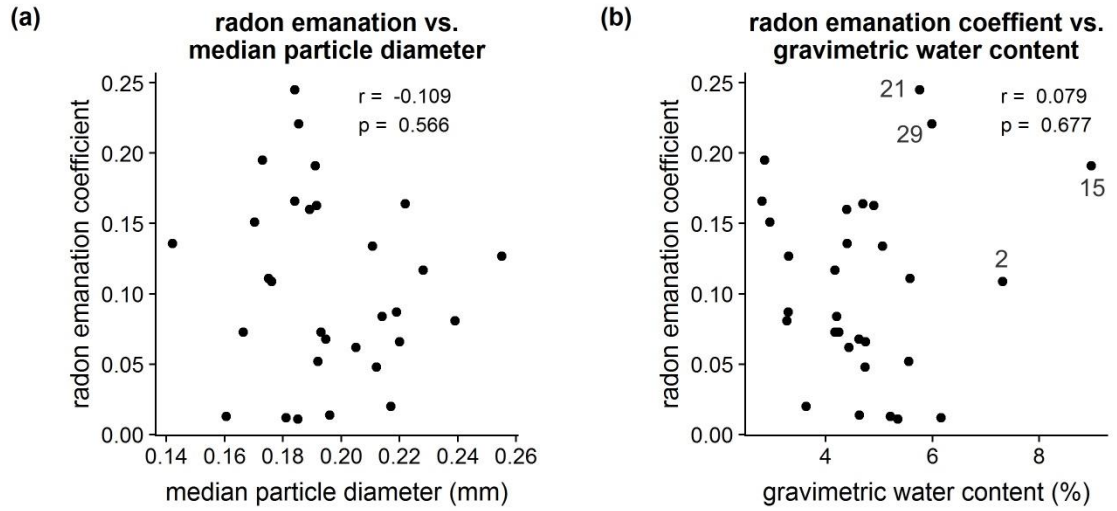

Figure 33. Correlation between radon emanation coefficient and its influencing parameters.

No correlation between radon emanation coefficient and median particle diameter was found (Figure 33a) considering the 30 sampling sites. Despite the lack of correlation between radon emanation coefficient and gravimetric water content for all the sampling sites (Figure 31b), a marked negative correlation can be observed after excluding the bivariate outliers. By excluding the 4 sampling sites labeled in Figure 33b the correlation improves significantly (r=-0.479, p=0.013).

7.2.3.4. Influencing parameters on soil gas radon concentration in air soil

The relationship between soil gas radon concentration and its direct influencing parameters was evaluated by a linear correlation bivariate analysis. The factors that influences directly the soil gas radon concentration are radium concentration, radon emanation coefficient, porosity and water content.

Additionally, the factors that influence the radon emanation and radium concentration were evaluated by correlation with the field measured soil gas radon concentration as indirect influencing factors. Correlation analysis was performed for all sampling sites (n=30), for both direct and indirect influencing factors. However, considering the special behavior of the sampling sites 11 and 15 explained in sections 7.2.1 and 7.2.2, respectively, a second correlation analysis was performed without those sampling sites (n=28). The results of the two correlation analyses are detailed in Table 17.

Table 17. Correlation between field measured soil gas radon concentration and its influencing factors

Soil parameters	n=30		n=28	
	r	p	r	p
radon emanation coefficient	**0.605**	**0.000**	**0.636**	**0.000**
radium concentration (Bq kg^{-1})	**0.563**	**0.001**	**0.397**	**0.037**
gravimetric water content (%)	-0.030	0.873	-0.023	0.906
organic content (%)	**0.343**	**0.063**	0.270	0.164
pH	**-0.571**	**0.009**	**-0.498**	**0.007**
soil gas permeability (m^2)	**0.449**	**0.013**	0.202	0.302
total porosity	0.135	0.478	0.282	0.146
effective porosity	0.234	0.213	0.277	0.153
air filled porosity	0.117	0.537	0.257	0.186
clay fraction (%)	**0.352**	**0.056**	0.359	0.061
silt fraction (%)	0.324	0.081	0.358	0.061
sand fraction (%)	-0.333	0.072	-0.364	0.057

Soil gas radon concentration has a positive and significant correlation with radium concentration and emanation coefficient (Table 17 and Figure 34). When the sampling sites 11 and 15 are excluded, the correlation coefficient between soil gas radon concentration and radium concentration decreases considerably, meanwhile the correspondent to the radon emanation slightly increases (Table 17). Whereas there is no significant correlation of soil gas radon concentration and soil water content.

Although there is not a significant correlation between soil gas radon concentration and effective porosity (Table 17), a positive correlation tendency can be seen in Figure 34c. As it is illustrated in Figure 34d, there is no correlation between soil gas radon concentration and total and air-filled porosity.

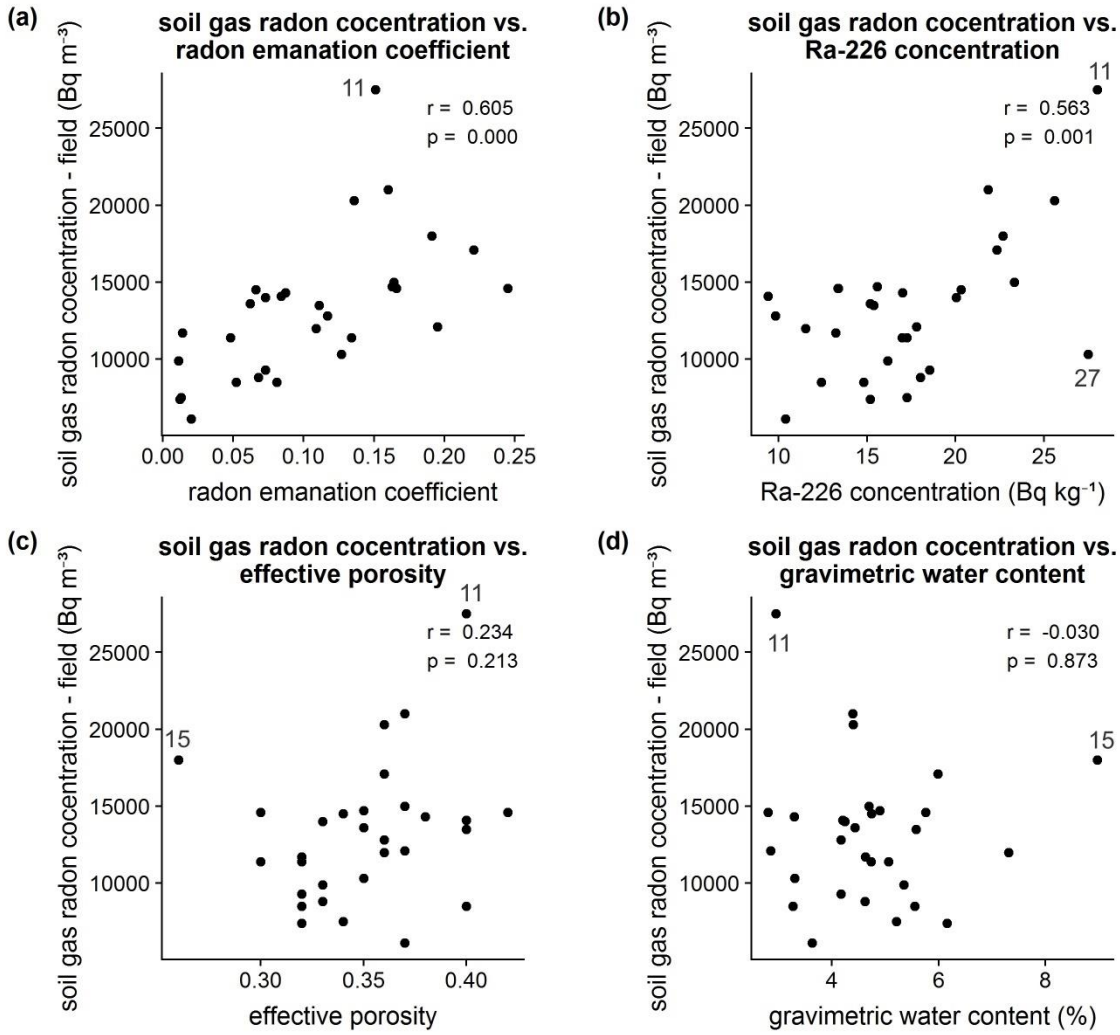

Figure 34. Correlation between soil gas radon concentration and its direct influencing factors.

Soil gas radon concentration has no direct relationship with the evaluated soil properties (Figure 35).

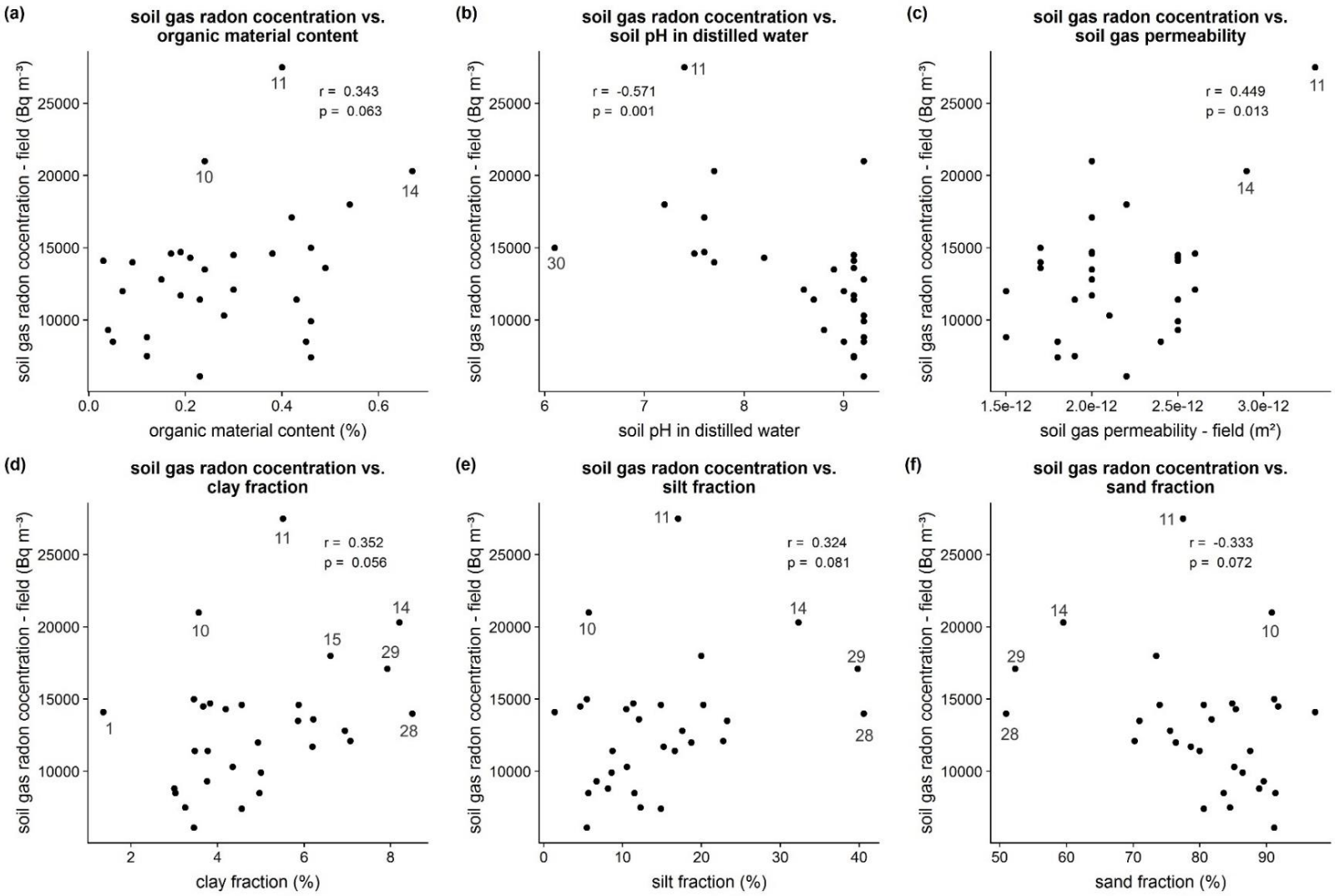

Figure 35. Correlation between soil gas radon concentration and its indirect influencing factors.

7.2.4. Estimated soil gas permeability and soil gas radon concentration

According to the aim of this research, the empirical model developed by Rogers and Nielson (1991) model MP1 (Eq. 6) and the theoretical models developed by Porstendorfer (1994) model MR1 (Eq. 8) and by Várhegyi et al. (2013) model MR2 will be applied to the study area to test its usability.

7.2.4.1. Soil gas permeability field measured vs. estimated soil gas permeability

According to the empirical model developed by Rogers and Nielson (1991) model MP1 (Eq. 6), the input parameters for the estimation of the soil gas permeability are: total porosity, arithmetic mean diameter, excluding particles > 4.7 mm, and volume fraction of water saturation. A variation to this model is introduced by the particle diameter that was determined by two methods of grain size distribution; dry sieving - sedimentation (DS-SED) and dry sieving - laser diffraction (DS-LD) (Table 18). In this way, the influence of the method applied for the determination the grain size distribution in the empirical model MP1 is evaluated.

Table 18. Variation of the model for estimation of soil gas permeability MP1 based on the methodology of grain size distribution

model	**model MP1 (Eq. 6) (Rogers and Nielson, 1991a)**	**particle diameter (d_a) characteristics**	**remarks**
MP1 DS-SED	$K = \left(\frac{p_t}{500}\right)^2 \boldsymbol{d_a}^{4/3} \exp(-12s^4)$	obtained from DS-SED	method: used by the authors
MP2 DS-LD		obtained from DS-LD	method: accurate widely used

The summary statistics of the field measured and estimated soil gas permeability is shown in Table 19.

Table 19. Summary statistics of field measured and estimated soil permeability (n=28) for models MP1 DS-SED and MP1 LD

Soil gas permeability (m^2)	Min.	Max.	Mean	Median	STDEV
FIELD measured	1.50E-12	3.30E-12	2.16E-12	2.00E-12	4.18E-13
MP1 DS-SED estimated	9.86E-12	3.45E-11	1.88E-11	1.73E-11	6.57E-12
MP1 LD estimated	6.69E-12	3.03E-11	1.35E-11	1.12E-11	6.31E-12

The estimated soil gas permeability by applying for the evaluated models MP1 is one order of magnitude greater than the corresponding field measured values (Table 19, Figure 36). Considering that perfect estimation of the predicted value, by the theoretical model, respect to the measure one is 100 %, therefore overestimation is calculated as the percentage of the predicted value which exceeds the field measured value. The median of the estimated soil gas permeability applying the model MP1 DS-SED represents an overestimation of 765 % referred to field measured value, whereas with the model MP1 DS-LD the overestimation is 460 %.

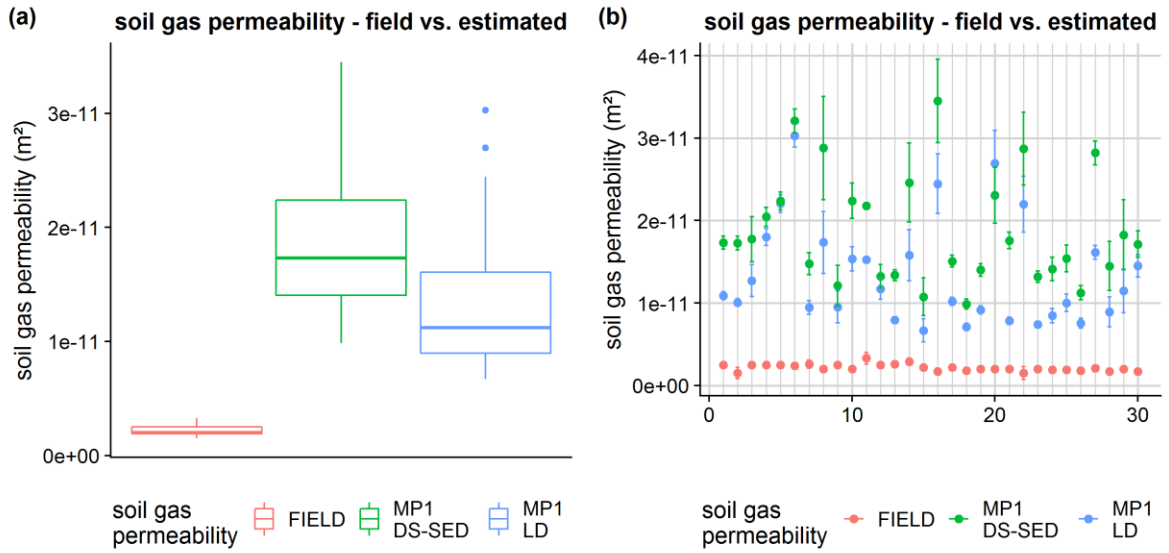

Figure 36. Comparative plot between field measured and estimated soil gas permeability obtained through the application of the models MP1 DS-SED and MP1 LD, illustrated by a) box-and-whiskers plot and b) scatter plot by sampling site.

The difference of the median between the estimated soil gas radon concentration by applying the models MP1-DS-SED and MP1 DS-LD is 6.1E-12, which means that the model MP1-DS-SED overestimates the model MP1 DS-LD in 54.4 %. The variability between the

models MP1-DS-SED and MP1 DS-LD reflects the sensitivity of this model to the particle size. Furthermore, the model uses arithmetic mean diameter as input parameter which does not represent the real particle diameter since the grain size distributions of all 30 samples are not normal, but lognormal, as it is illustrated in Annex II.. The estimated soil gas permeability by the models MP1-DS-SED and MP1 DS-LD at each sampling site is shown in Figure 36b with the error estimated by Tylor's series.

The correlation plot between the field measured and the estimated soil gas permeability is shown in Figure 37 in logarithmic scale. Correlation coefficient and significance are indicated in the legend. No correlation was found between the field measured soil gas permeability and the estimate ones by the models MP1-DS-SED and MP1 DS-LD, respectively.

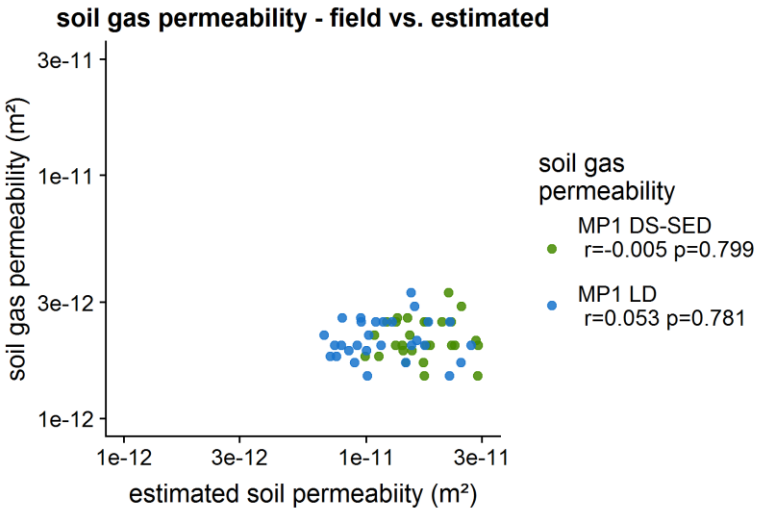

Figure 37. Correlation plot between the field measured and estimated soil gas permeability without outliers (n=30)

7.2.4.2. Soil gas radon concentration field measured vs. estimated soil gas radon concentration

The theoretical models applied for the estimation of soil gas radon concentration are model MR1 proposed by Porstendorfer (1994) (Eq. 8) and model MR2 proposed by Várhegyi et al. (2013) (Eq. 9), who modifies the model MR1 (Eq. 8) by introducing a factor in model MR2,

which considers the radon concentration in the water phase of the pore space (Eq. 9) that is neglected in by Porstendorfer (1994) in model MR1. (Table 20).

Table 20. Remarks of theoretical models for the estimation of equilibrium soil gas radon concentration

Model and formula	remarks
MR1 $C_\infty = \frac{C_{Ra}\varepsilon\rho_{bulk\ dry}}{p_e}$	widely used model; the radon concentration in the water fraction of the pore space is neglected.
MR2 $C_\infty = \frac{C_{Ra}\varepsilon\rho_{bulk\ wet}}{p_e(w_m+1)-\left(\frac{\rho_{bulk\ wet}}{\rho_{water}}\right)w_m(1-k)}$	in the model the fraction of radon in the water and air phase is considered; it is only valid for non-saturated conditions

The box-and-whiskers plot of Figure 38a shows the estimated soil gas radon concentration by the models MR1 and MR2, respectively, plotted together with the field measured values. Besides differences in the medians between the measured and estimated values, there is a clearly marked outlier in the predicted distribution of model MR2.

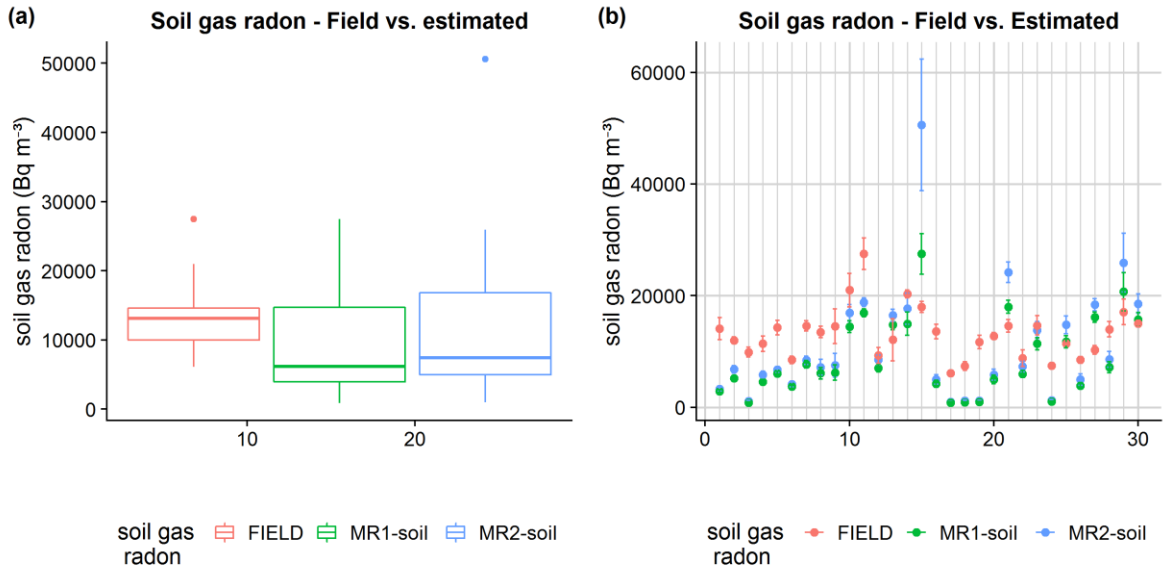

Figure 38. Comparative plot of field measured and estimated soil gas radon concentration obtained through the application of the models MR1 and MR2, illustrated by a) box-and-whiskers plot and b) scatter plot by sampling site.

This outlier corresponds to the sampling site 15 which is seen in Figure 38b. As it was described earlier this sampling site is undersaturation conditions and considering that the model MR2 cannot valid for saturation conditions, therefore, this sampling site is excluded of this analysis. For comparison purposes, the outlier of the field measured soil gas radon concentration is excluded, as well.

The summary statistics of the models MR1 and MR2 models with the determined soil properties, excluding the sampling sites 11 and 15 (outliers), is seen in Table 21. Comparing the median values of the estimations and the measured soil gas radon concentration, it can be affirmed that the model MR1 underestimates the field measured soil gas radon concentration in 51.2 % and MR2 one in 41.6 % and in both cases, the values are distributed in a wider range than the correspondent to the field measured range.

Table 21. Summary statistics of measured and estimated soil gas radon concentration (n=28)

Soil gas radon concentration (Bq m^{-3})	Min.	Max.	Mean	Median	STDEV
FIELD measured	6100	21000	12464	12450	3608
MR1-soil estimated	863	20718	7804	6068	5838
MR2-soil estimated	994	25920	9390	7263	7146

In spite of the numerical differences between the field measured soil gas radon concentration and the corresponding values obtained through the application of the models MR1 and MR2, respectively, the estimated values have significant positive correlation with the field measured values, reflected in the correlation coefficient above 0.62 ($r_{MR1} = 0.647$ and $r_{MR2} = 0.62$) and the significance lower than 0.05, shown in Figure 39.

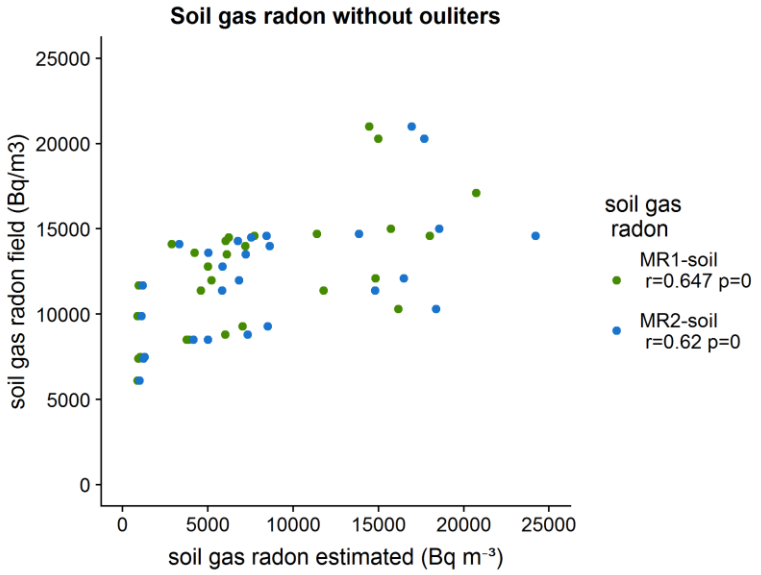

Figure 39. Correlation plot between the field measured and estimated soil gas radon concentration, without sampling sites 11 and 15 (n=28).

The difference between the estimated and the field measured soil gas radon concentrations can be mainly attributed to two types of radon transport mechanism and geochemical process. Regarding to the mechanism of radon transport in soil, the evaluated theoretical models MR1 and MR2 were determined considering only molecular diffusion. Consequently, the fraction of radon, transported by advection, is neglected. Based on the geochemical behavior of radium, there are process that influences significantly the soil gas radon concentration such as the preferential adsorption of radium in organic material at low concentration of carbonates and high concentration of organic material and clay minerals (Thorne and Mitchell, 2011).

7.2.5. Modification of the models

7.2.5.1. Modified models to estimate soil gas permeability

Two modifications on the empirical model MP1 for the estimation of soil gas permeability are proposed in this evaluation, to improve the predictive power of model MP1. The modified models MP2 (Eq. 26) and MP3 (Eq. 27) use the particle diameter of soil obtained from grain size distribution for the methods of dry sieving – sedimentation (DS-SED) and dry sieving – laser diffraction (DS-LD) independently.

$$\boldsymbol{MP2}\text{: } K = \left(\frac{p_t}{500}\right)^2 {d_a}^{8/5}\exp(-12s^4) \qquad \text{Eq. 26}$$

The empirical model MP1 (Rogers and Nielson, 1991a) based on 137 in situ measurements of soil gas permeability. Most of these measurements are in the range of $1x10^{-11}$ m^2 (Figure 5) that corresponds to well-graded sand and gravel (Figure 4). Few measurements correspond to silty, sandy and gravel soils that are the evaluated in this research, which permeability is in the range of $1x10^{-12}$ m^2 (Figure 4) that corresponds to the field measured sampling sites. Thus, MP1 models considers the effect of coarse particles, that based on the predominant range of permeability, are gravel (75 -2 mm) and sand (2 -0.063 mm) (USDA, 2014). The effect of the coarse particles in the model MP1 is reflected in the use of arithmetic mean diameter as an indicator of soil particle size. This magnifies the particle diameter if the grain size distribution is not normal. By a slightly modification of model MP1, the modified model MP2 proposes the diminution of the sensitivity of the original model to the particle diameter by changing its exponent from 4/3 to 8/5.

$$\boldsymbol{MP3}\text{: } K = \left(\frac{p_e}{500}\right)^2 {d_m}^{4/3}\exp(-12s^4) \qquad \text{Eq. 27}$$

The third model MP3 presents a change in the input parameters as follow: the total porosity and arithmetic mean particle diameter are replaced by the effective porosity and the median particle diameter. Effective porosity represents the interconnected pores that allows the transport of fluids through the soil. This is theoretically concordant with the definition of permeability; thus, the effective porosity presents a better relationship with permeability than the total porosity. This affirmation is confirmed by the results presented in Table 14, where the soil field measures soil gas permeability is correlated, when sampling site 15 is not considered, with total porosity. However, there is a lack of correlation with total and air filled porosity.

The results of the proposed modification of the models are shown in Figure 40 and the correspondent summary statistics in Table 22.

Table 22. Summary statistics of modified predictive models of soil gas permeability (n=28)

Soil gas permeability (m^2)	Min.	Max.	Mean	Median	STDEV
FIELD measurement	1.50E-12	2.90E-12	2.12E-12	2.00E-12	3.71E-13
MP2 DS-SED estimated	1.09E-12	4.79E-12	2.38E-12	2.04E-12	9.83E-13
MP2 LD estimated	7.31E-13	3.98E-12	1.62E-12	1.21E-12	9.08E-13
MP3 DS-SED estimated	4.22E-12	1.28E-11	6.85E-12	6.43E-12	2.07E-12
MP3 LD estimated	3.60E-12	9.16E-12	5.70E-12	5.34E-12	1.50E-12

The median of modified model MP2-DS-SED shown in Table 22 is equal to the correspondent value of the field measured soil gas permeability. However, there is no correlation between them (Figure 41). The corresponding results to the model MP2-DS-LD underestimates in 31 % the median of field measured and has no correlation with the measured soil gas permeability.

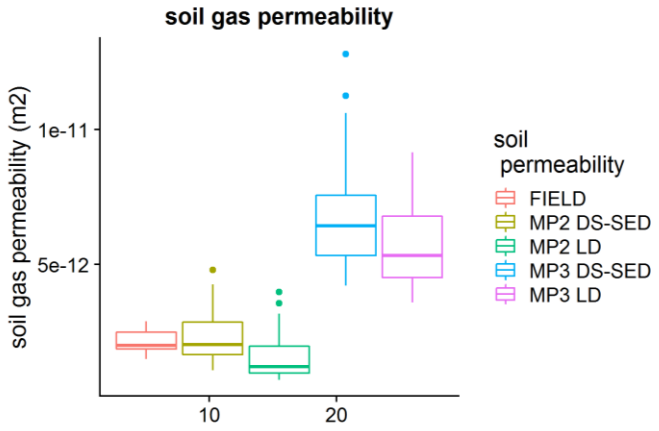

Figure 40. Comparative box-and-whiskers plot between the field measured soil gas permeability and the corresponding values obtained from the modified predictive models MP2 and MP3.

The influence of the grain size distribution method in the application of the model MP2 is reflected in the difference between the median soil gas permeability for models MP2 DS-SED and MP2 DS-LD shown in Table 22 and Figure 40. It means that the best approximation for the soil gas permeability can be obtained by model MP2 using the particle diameter from the method of dry sieving – sedimentation for particle size distribution. The lack of correlation between the measured and estimated values of soil gas permeability obtained with

model MP2 DS-SED (Figure 41) ($r_{MP2\,DS-SED} = 0.016$ and $r_{MP2\,DS-LD} = 0.195$) can be attributed to the fact that the soil pore structure is not considered in the model MP1.

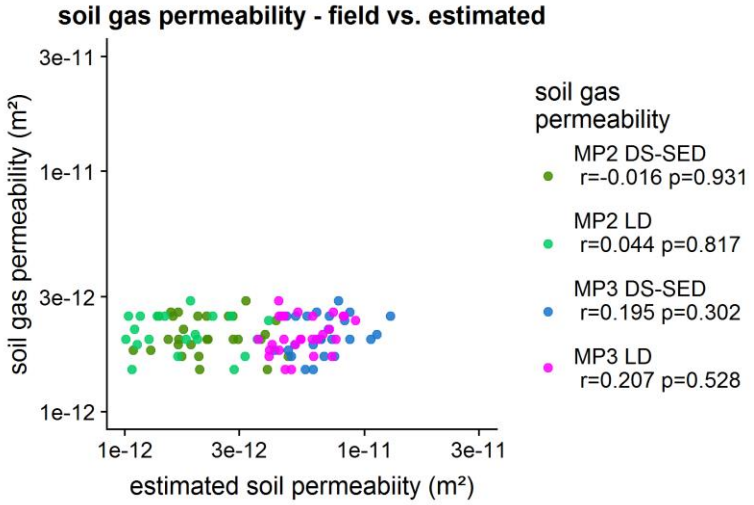

Figure 41. Correlation plot between the field measured and the estimated soil gas permeability by applying the modified models MP2 and MP3.

Hence, it is recommendable to apply the model MP2 DS-SED for the estimation of soil gas permeability for the range permeability of the study area (Table 6) and following the dry sieving - sedimentation method for gran size distribution. Besides the limitations, the median soil gas permeability obtained by model MP2 DS-SED is in perfect agreement with the median of field measured values, considering that the estimation of soil gas permeability by MP2 DS-SED model is based on only three basic soil properties (i.e., porosity, particle diameter and saturation water content) commonly available in databases. Taking into account the limitations, model MP2 DS-SED was selected for the estimation of soil gas permeability and the subsequent calculation of the geogenic radon potential.

7.2.6. Modified models to estimate soil gas radon concentration

The modifications of the theoretical models MR1 and MR2 for the estimation of soil radon concentration were based on the effect of the preferential adsorption of radium on organic material at pH < 8 that influences the radon emanation and consequently the soil gas radon concentration. At pH > 8 the absorption of radium in clay minerals is considered as the

controlling process. From the 30 measured sites, only in 9 sampling sites the pH of the soil is below 8, including sampling sites number 11 and 15 (Table 16). However, these two sampling sites (15 and 11) were excluded for the model evaluation and for its modification, thus only 7 samples will be considered in this category.

The input parameters, involved in the modification of the models MR1 and MR2, at pH < 8 are: estimated soil gas radon concentration (by models MR1 and MR2, respectively) organic, clay grain size fraction and carbonate content (Table 23). Clay grain size fraction was used as an indication of clay minerals, based in the correlation between clay fraction and the concentration of aluminum (major component in clay minerals) and rubidium (commonly adsorbed in clay minerals) of the soil (Table 12).

For the group of 21 remaining sampling sites, which soil samples has pH > 8, the influence of soil gas radon of clay and sand is the criterion for the modification of the models MR1 and MR2. However, both parameters are strongly correlated with each other that causes collinearity problem in the multivariable regression. Therefore, the silt fraction selected as an input parameter. For model MR1, volume fraction of water saturation was added since the original model does not consider this parameter. The following notation was used in the code of the models as follows: MR3-1 and MR3-2 are the modification of the models MR1 and MR2 at pH < 8, respectively, MR4-1 and MR4-2 modification of the models MR1 and MR2 at pH > 8.

The input parameters that are expressed in percentage are expressed in fraction (*f*) by dividing them to 100. The linear models calculated for the groups, based on soil pH (Table 23). For each model, coefficients are listed together with the corresponding standard error, significance, and the R^2, standard error and significance for each model is detailed in Table 23. Due to the low number of (n=7) of sampling sites with soil pH < 8, the results for the models MR3-1 and MR3-2 can be influenced by the variability of the data within the input parameters, which is reflected in the standard error and significance. The correlation coefficients for the model MR3-1 (r=0.98) and for the model MR3-2 (r=0.98) (Figure 42b), and the determination coefficient (R^2) of the multivariate linear regression demonstrate a strong linear correlation between the estimated values and field measurements (Figure 42b).

Table 23. Linear models applied to modify the models for the estimation of soil gas radon concentration MR1 and MR2

model MR5: modification of MR1

model MR3-1 modification of MR1 at pH < 8 (n=7)

$$C_\infty = a_1 C_{\infty\, MR1} + b_1 f_{organic} + c_1 f_{clay} + d_1 f_{carbonate}$$

	coefficient	Std. error	p
intercept	1.122E+04	1.213E+03	0.0115
a_1	1.233E-01	5.614E-02	0.1593
b_1	3.131E+05	2.049E+05	0.2661
c_1	2.157E+04	1.369E+04	0.2558
d_1	1.010E+05	3.363E+04	0.0952
model	R^2=0.92	Std. err=637.5	p=0.054

model MR4-1 modification of MR1 at pH > 8 (n=21)

$$C_\infty = x_1 C_{\infty\, MR1} + y_1 f_s + z_1 f_{silt}$$

	coefficient	Std. error	p
intercept	10826.3866	3703.7178	0.00949
x_1	0.3281	0.1666	0.06545
y_1	-4574.7461	18096.2051	0.80345
z_1	-4825.3382	12388.3410	0.70174
model	R^2=0.097	Std. err=3154	p=0.2011

model MR6: modification of MR2

model MR3-2 modification of MR1 at pH < 8 (n=7)

$$C_\infty = a_2 C_{\infty\, MR2} + b_2 f_{organic} + c_2 f_{clay} + d_2 f_{carbonate}$$

	coefficient	Std. error	p
intercept	1.131E+04	1.249E+03	0.012
a_2	8.556E-02	4.131E-02	0.174
b_2	3.656E+05	2.054E+05	0.217
c_2	2.164E+04	1.426E+04	0.269
d_2	9.778E+04	3.480E+04	0.107
model	R^2=0.91	Std. err=663.9	p=0.058

model MR4-2 modification of MR1 at pH > 8 (n=21)

$$C_\infty = x_2 C_{\infty\, MR2} + z_2 f_{silt}$$

	coefficient	Std. error	p
intercept	9926.0366	1607.6676	7.9e-06
x_2	0.3013	0.1291	0.0314
z_2	-5667.2588	11708.2977	0.6342
model	R^2=0.15	Std. err=3066	p=0.0927

The outlier in the both estimated and field measured soil gas radon concentration at pH < 8, corresponds to the sampling site 14, which has the highest organic material content of the 30 measurements (Table 23).

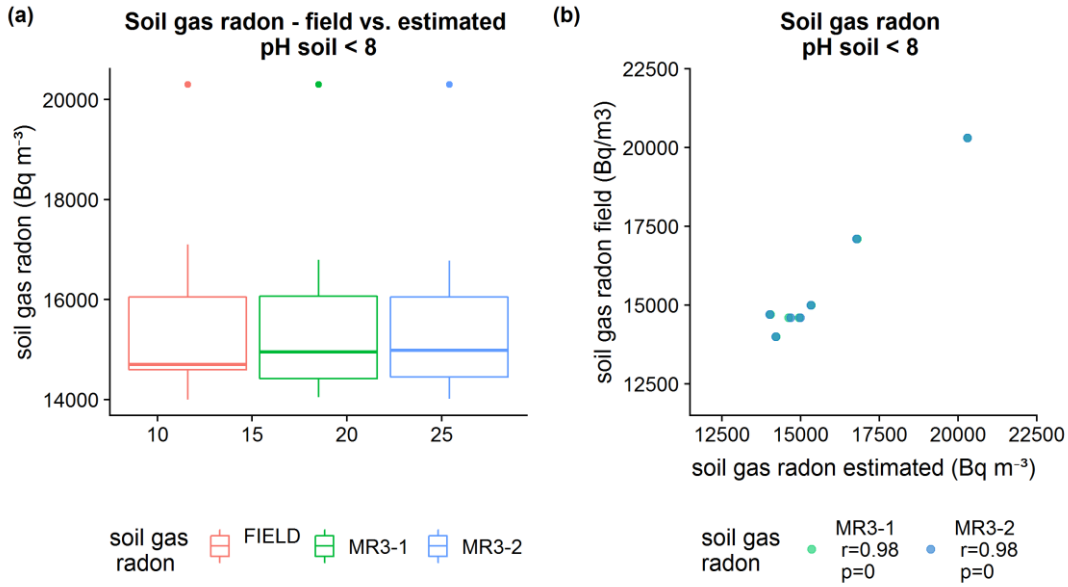

Figure 42. a) Comparative box-and-whiskers plot and b) correlation plot between the field measured soil gas radon concentration and the correspondent values obtained by the modified models MR3-1 and MR3-2 at pH < 8.

The correlation coefficient between the field measured and the estimates soil gas radon concentration is (0.48 in both cases) (Figure 43) shows a weak but significant correlation between the soil gas radon concentration measured and the estimated with the modified models MR4-1 and MR4-2. The difference between the field measured soil gas radon concentration and the estimated values with models MR4-1 and MR4-2, can be explained by the fact that at pH > 8 the effect preferential adsorption of radium in clay minerals is less pronounced compared to the preferential adsorption of radium in organic material at pH < 8 (Greeman and Rose, 1996; Nathwani and Phillips, 1979a, 1979b; Thorne and Mitchell, 2011). Hence, the influence of additional process such as advection, local mineral composition can be reflected in the soil gas radon concentration.

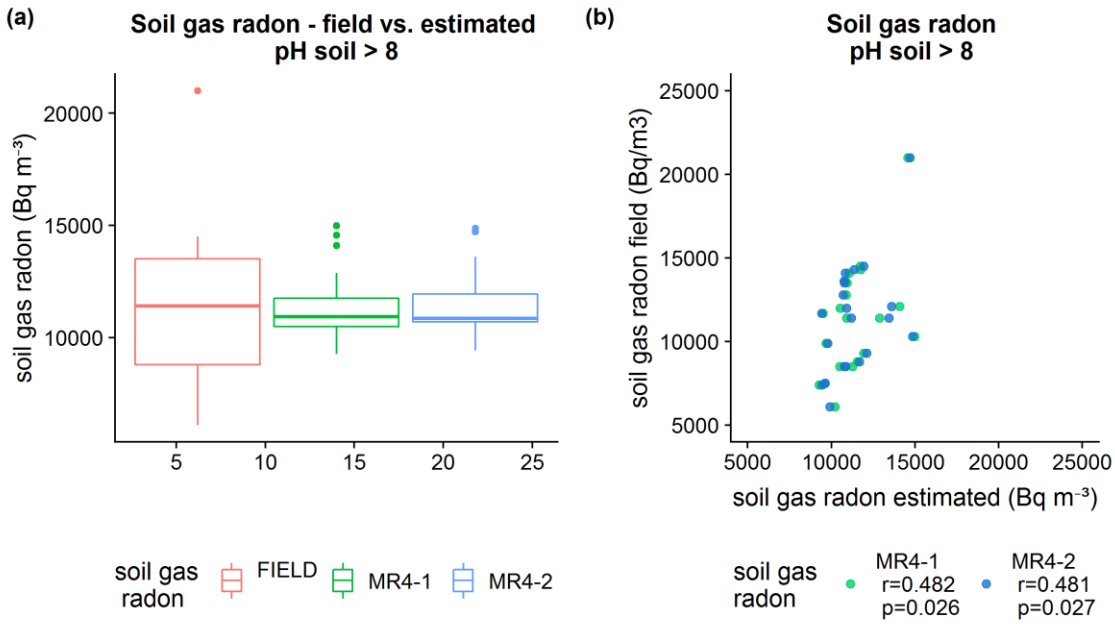

Figure 43. a) Comparative box-and-whiskers plot and b) correlation plot between the field measured soil gas radon concentration and the correspondent values obtained by the modified models MR4-1 and MR4-2 at pH > 8.

Table 24 shows the summary statistics of the estimated soil gas radon concentration at each pH range. The median soil gas radon concentration for soils at pH < 8 is only 3300 Bq m^{-3}, which is greater than the median at pH > 8. The standard deviation is not significant.

Table 24. Summary statistics for soil gas radon concentration the modified models (n=28)

	Min.	Max.	Mean	Median	STDEV
	pH < 8			n=7	
FIELD measure	14000	20300	15757	14700	2232
MR3-1 estimate	14045	20297	15755	14955	2201
MR3-2 estimate	14018	20303	15760	14989	2199
	pH < 8			n=21	
FIELD measure	6100	21000	11367	11400	3319
MR4-1 estimate	9267	14983	11366	10929	1601
MR4-2 estimate	9416	14866	11366	10856	1600

To estimate soil gas radon concentration for the 28 considered sites, the model MR5 is the resultant model for the modification of model MR1 (Table 23) that involves the multivariate linear models MR3-1 at pH < 8 and MR4-1 at pH > 8. In similar way for MR6, which is the modified model of MR2, is defined by model MR3-2 at pH < 8 and MR4-2 at pH > 8 for MR2 (Table 23).

The summary statistics for the models MR5 and MR6 is shown in Table 25. The final models determined for soil gas radon concentration estimates practically the same values due to the fact that both models are function of the same input parameters. The modified model MR5 underestimates the field measures soil gas radon concentration in 6.5 % and model MR6 in 7.4 %.

Table 25. Summary statistics for the soil gas radon concentration estimated by the modified models for soil gas radon concentration MR5 and MR6

	Min.	Max.	Mean	Median	STDEV
FIELD measured	6100	21000	12464	12450	3608
MR5 estimated	9267	20297	12463	11635	2592
MR6 estimated	9416	20303	12465	11519	2593

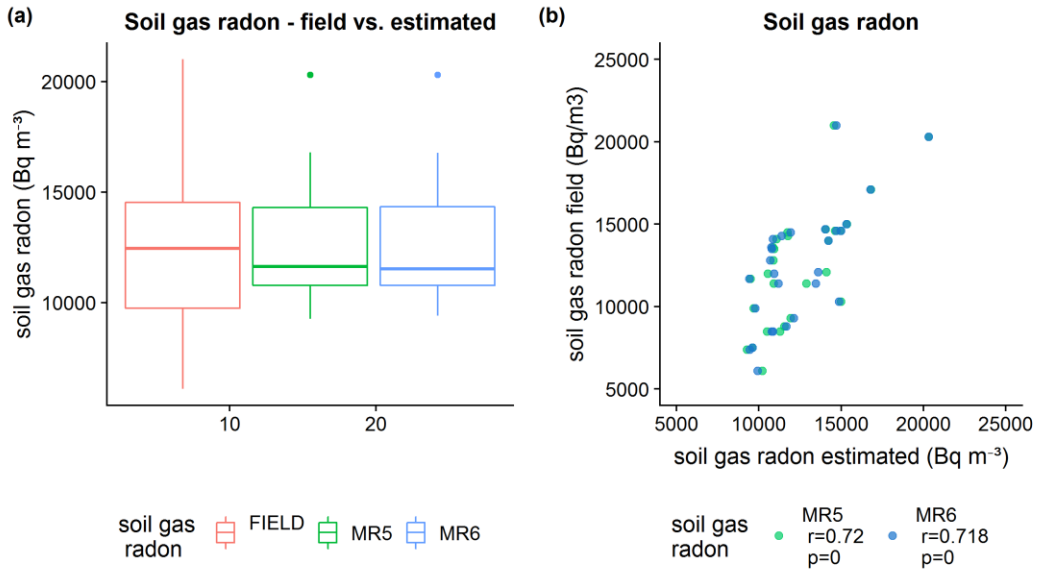

Figure 44. a) Comparative box-and-whiskers plot and b) correlation plot between the field measured soil gas radon concentration and the correspondent values obtained by the modified models MR5 and MR6.

The modified models MR5 and MR6 has positive significant correlation (r=0.72, p=0) with the measured values (Figure 44). Models MR5 and MR6 have an outlier that corresponds to the sampling site 14 (the highest organic material content). This value does not appear in the field measured data that is distributes in a wider range. The modified models MR5 and MR6 will be used for the calculation of geogenic radon potential GRP.

7.2.7. Calculated geogenic radon potential GRP with modified models

Considering the best results of the modified models improve the predictive power for permeability in model MP2 DS-SED and for soil gas radon concentration in models MR5 and MR6. The geogenic radon potential GRP based on the estimated models applying the following equations:

$$GRP1 = \frac{C_{\infty\, MR5}}{-\boldsymbol{log_{10}}(\boldsymbol{K}_{\boldsymbol{MP2\ DS-SED}})-\boldsymbol{10}} \quad \text{Eq. 28}$$

$$GRP2 = \frac{C_{\infty\, MR6}}{-\boldsymbol{log_{10}}(\boldsymbol{K}_{\boldsymbol{MP2\ DS-SED}})-\boldsymbol{10}} \quad \text{Eq. 29}$$

The results of the estimated geogenic radon potential GRP are shown in Table 26 and Figure 45 showing perfect agreement in the medians and a significant correlation with field measured GRP.

Table 26. Summary statistics of geogenic radon potential (GRP) calculated from the modified models (n=28)

	Min.	Max.	Mean	Median	STDEV
FIELD measured	3.7	13.2	7.5	7.6	2.3
GRP1 estimated	4.7	13.6	7.6	7.6	1.9
GRP2 estimated	4.8	13.6	7.6	7.5	1.9

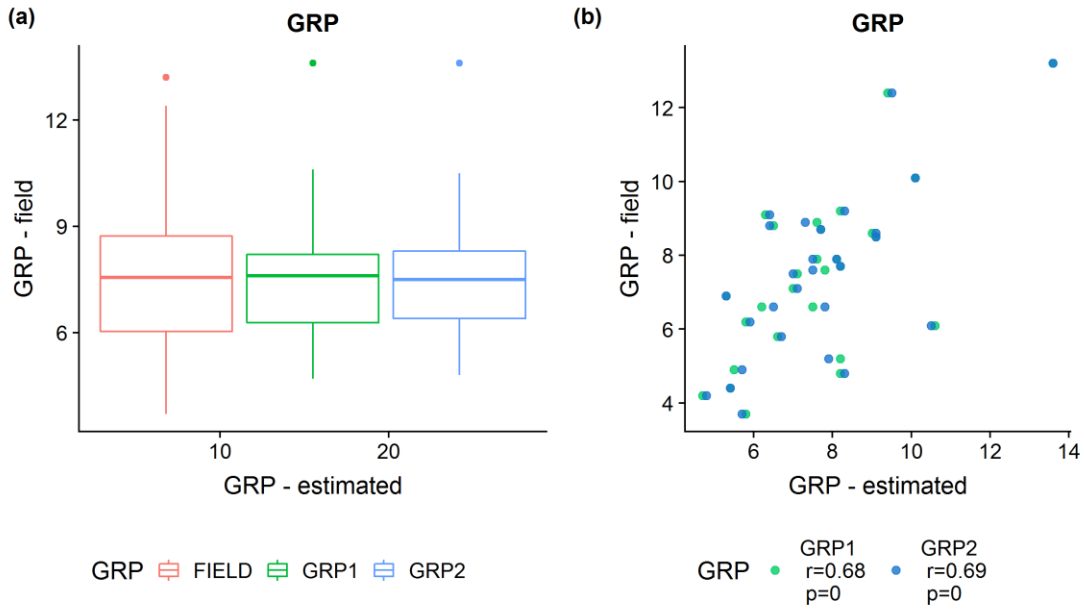

Figure 45. a) Box-and-whiskers plot and b) correlation plots between the geogenic radon potential (GRP) calculated from field measured values and the ones obtained by application of the modified models.

8. Conclusions

Evaluation of ambient gamma dose equivalent rate

- The gamma dose rate evaluation has two main findings: 1) the high gamma dose rate anomaly, characterized by high variability, spatially coincides with the high dike density area, and 2) the two main lineament directions (NE-SW and NW-SE) identified in the gamma dose rate coincide with the prevailing orientations of the underlying granitic dikes and fractures. Thus, this evaluation confirms that the main spatial features identified in the gamma dose rate map are connected to the underlying geological setting such as rock lithology, dike system and fault network arrangement in the study area. Significant positive linear correlation was found between the measured gamma dose rate and the dike density. The simple digital cross-section analysis proved to be efficient in describing spatial trends. However, the more advanced procedures of gradient (slope, aspect, curvature) calculations identified the prevailing orientations in the SW-NE and SE-NW directions as significant linear edges (lineaments) of gamma dose rates in the study area. Anisotropy along these orientations was characterized by autocorrelation and directional variogram calculations. The relief and local variability index identified areas of anomalous high local variability of the gamma dose rate coinciding with the area of high dike density in the southern part of the study area. This statement was also confirmed by their significant positive correlation. The locations of high variability are also the areas where gamma dose rates are the least predictable. The circular statistics calculated from the lineament map revealed two major directions corresponding to geological settings such as the dike system and fault zones.
- It has been shown that digital spatial analysis methods, including digital image processing techniques, are efficient in revealing spatial pattern in gamma dose rates and in identifying the relationship between the spatial pattern and the underlying geological setting at high resolution local scale, having 300 measurement sites in an about 4 x 5 km area with a 250 m sampling distance. It is concluded that these methods provide useful means for the recognition and characterization of spatial pattern in field measured ambient gamma dose equivalent rate at the local scale, too.

Evaluation of geogenic radon potential (GRP)

- The evaluation of the geogenic radon has three main findings: 1) determination of the influencing factors of geogenic soil gas radon concentration, 2) determination of usability of theoretical and empirical models to estimate soil gas radon concentration and soil gas permeability in the study area, and 3) modification of the evaluated models. The GRP in the study area is within the low risk category, with median value of 7.65 based on the classification proposed by Neznal et al. (2004) (low <10; medium ≥10 and ≤35; high >35). Determined from 30 field measurements of soil gas permeability and soil gas radon concentration in an area of 0.8 km^2. The median valued of soil gas permeability in the study area is $1.45x10^{-12}$ m^2, which belongs to the medium risk category of soil gas permeability. The median soil gas radon concentration is 13 150 Bq m^{-3} and corresponds to the low risk category according to the classification based on the classification proposed by Neznal et al. (2004).
- The soil factors that are influencing the soil gas radon concentration depends on the governing process at specific conditions. For the measured area at pH < 8, the governing geochemical process is the preferential adsorption of radium on organic material and clay at low concentration of calcium (as carbonate mainly). In this process the controlling factors are the organic material, carbonate and clay content on the soil. Above pH < 8, as the carbonate content increases, this process vanishes because calcium (generally in higher concentration than radium at this pH) competes with radium for adsorption sites in organic material. However, the radium is preferentially adsorbed by ion exchange in clays than calcium. Thus, the controlling factor in these conditions is the clay mineral content (EPA, 2004; Greeman and Rose, 1996; IAEA, 2014; Nathwani and Phillips, 1979a, 1979b; Thorne and Mitchell, 2011).
- The empirical equation, developed by Rogers and Nielson (1991) for the determination of soil gas permeability, cannot be applied such a small area with small range of soil gas permeability as applied in this study. The soil gas permeability values in the study area are in a small range, all of them are medium ($1{,}50\times10^{-12}$ m^2 – $3{,}30\times10^{-12}$ m^2) and in this narrow range, even data of Rogers and Nielson (1991) do not correlate. The estimated values are one order of magnitude higher than the field measured (765 % overestimation). Therefore, a modification of this equation is proposed in this research

to be applied in the study area. The median soil gas permeability, obtained by the modified equation, is in excellent agreement with the field measured data. However, the lack of correlation with the field measured values and the dependence of the methodology limits its application.

- The application of two theoretical models for the estimation of soil gas radon concentration is overestimated in both cases: by applying the models the soil gas radon concentration is underestimated. In this research, these models were modified by multiple linear regression models that uses the estimated soil gas radon concentration by theoretical models and the respective controlling factors at the defined conditions.

Thesis points of the doctoral study

1) I determined a high ambient gamma dose equivalent rate anomaly, spatially coincides with the high dike density area. Also, anomalous high local variability areas of the gamma dose rate coinciding with the area of high dike density characteristic for the southern part of the study area (Beltrán Torres et al., 2018).

2) I identified that the gradient (slope, aspect, curvature), which represents the sudden changes of gamma dose equivalent rates in the study area coincide with the corresponding prevailing orientations of the underlying granitic dikes (SW-NE) and fractures (NW-SE) (Beltrán Torres et al., 2018).

3) I determined that in the measured area, at pH < 8, the governing geochemical process is preferential adsorption of radium on organic material and clay at low concentration of calcium present as mainly carbonate mineral. In that process the controlling factors are the organic material, carbonate and clay content on the soil. At pH > 8, as the carbonate content increases, this process vanishes because calcium ions (generally, in higher concentration than radium at this pH) competes with radium ions for adsorption sites in organic material. Thus, the controlling factor in these conditions is the clay mineral content (Beltrán Torres et al., 2019b).

4) I proved that the empirical equation developed by Rogers and Nielson (1991) for the determination of soil gas permeability cannot be used for such a small area (< 1 km^2) with reduced range of soil gas permeability applied in this study. Therefore, I modified the model by changing the exponent of the particle diameter (from 4/3 to 8/5). Thus, the median soil gas permeability, obtained by the modified equation, is in excellent agreement with the field measured median value (Beltrán Torres et al., 2019a).

5) I determined that the two theoretical models, proposed by Porstendorfer (1994) and Várhegyi et al. (2013), for soil gas radon concentration underestimate the measured values. Based on the multiple linear regression analysis, I included the carbonate, organic material and clay content of the soil into the models. Thus, I obtain higher correlation and the same order magnitude of the modeled and the field measured values (Beltrán Torres et al., 2019a).

Summary

Since terrestrial radiation is the most important source of natural radioactivity, environment including human being is exposed to, it has high importance to define its relationship with local geology and physicochemical properties of the surrounding soil and rocks. In this framework, the PhD research focuses on a detailed study of terrestrial natural radioactivity through the independent evaluation of 1) ambient gamma dose equivalent rate and 2) geogenic radon potential that represents the potential risk of geogenic radon to the human health. The study was conducted in the western side of the Velence Hills, the largest granitic outcrop in Hungary.

1) The evaluation of the ambient gamma dose equivalent rate is based on 300 field measurements at ground level along a 250 m x 250 m regular grid in of 19.8 km^2 area that covers the full extent of the granite mass. Digital spatial analysis methods were applied in order to identify spatial pattern such as triangular irregular interpolation network (TIN), smoothing, local maxima, local variability, gradient (slope, aspect, profile curvature), autocorrelation, density and frequency distribution. As the result, it was found that the high ambient gamma dose equivalent rate anomaly spatially coincides with the occurrence of high dike density area. Also, from the gradient analysis, the prevailing SW-NE and NW-SE directions of the linear features (lineaments) of ambient gamma dose equivalent rate was determined. These coincide with the prevailing directions of the underlying granitic dikes (SW-NE) and fractures (NW-SE) confirming its relationship.

2) The evaluation of GRP was performed by field measurement of soil gas radon activity, soil gas permeability and the determination of the soil properties in 30 sampling sites in a total area of 0.8 km^2 located in the center of the granite mass in a slope sediment formation (basically soil and rock debris). The effect of soil properties during the field measured parameters was evaluated and, as a result, it was found that the carbonate, organic material and clay content of the soil are those principal parameters which define the environmental behavior of radium and consequently controls the soil gas radon activity or content. Additionally, the utility of theoretical and empirical predictive models, using values of soil gas radon concentration and soil gas permeability, were tested by comparison with the field measured corresponding values. As a conclusion, the tested models cannot be applied directly for the study area due to a significant over estimation (765 %) in the soil gas permeability and underestimation (50 %) of the soil gas radon concentration. In this sense, a modification of this model in geochemical parameters are presented in this thesis.

References

Barretto, P.M.C., 1973. Emanation characteristics of terrestrial and lunar materials and the radon-222 loss effect on the uranium-lead system discordance. Ph.D. thesis. Rice University. Houston Texas.

Barton, C.D., Karathanasis, A.D., 2002. Clay minerals. In Encyclopedia Soil Sci. Dekker. South Carolina. USA, 187-192.

Beltrán Torres, S., Petrik, A., Szabó, K.Z., Jordan, G., Yao, J., Szabó, C., 2018. Spatial relationship between the field-measured ambient gamma dose equivalent rate and geological conditions in a granitic area, Velence Hills, Hungary: An application of digital spatial analysis methods. J. Environ. Radioact. 192, 267–278.

Beltrán Torres, S., Szabó, K.Z., Szabó, C., 2019a. Testing theoretical and empirical models for soil gas radon and soil air permeability determination: comparison with field measurements. European Geoscience Union General Assembly (EGU), 7-12 April 2019, Vienna, Austria. Geophysical Research Abstracts, Vol. 21, EGU2019-17995.

Beltrán Torres, S., Szabó, K.Z., Szabó, C., 2019b. Geochemical study and evaluation of predictive models for soil gas radon concentration in a granitic area in Hungary. 3rd International Conference "Radon in the Environment 2019", 27-31 May 2019, Krakow, Poland. Book of abstracts, p. 48, ISBN: 978-83-63542-17-7.

Benkó, Z., Molnár, F., Lespinasse, M., Váczi, T., 2014. Evidence for exhumation of a granite intrusion in a regional extensional stress regime based on coupled microstructural and fluid inclusion plane studies - An example from the Velence Mts., Hungary. J. Struct. Geol. 65, 44–58.

Blin-Stoyle, R.J., 1991. Nuclear and Particle Physics, 1st ed. Springer Netherlands. ISBN: 978-0-412-38320-5. 224 pages.

Bossew, P., 2003. The radon emanation power of building materials, soils and rocks. Appl. Radiat. Isot. 59, 389–392.

Bossew, P., Cinelli, G., Hernández-Ceballos, M., Cernohlawek, N., Gruber, V., Dehandschutter, B., Menneson, F., Bleher, M., Stöhlker, U., Hellmann, I., Weiler, F., Tollefsen, T., Tognoli, P. V., de Cort, M., 2017. Estimating the terrestrial gamma dose rate by decomposition of the ambient dose equivalent rate. J. Environ. Radioact. 166, 296–308.

Bossew, P., Tollefsen, T., Cinelli, G., Gruber, V., De Cort, M., 2015b. Status of the European Atlas of Natural Radiation. Radiat. Prot. Dosimetry 167, 29–36.

Bossew, P., Tollefsen, T., Gruber, V., M, D.C., 2013. The European Radon Mapping Project. Conference material. IX Lat. Am. IRPA Reg. Congr. Radiat. Prot. Saf. - IRPA 2013 2.

Borgoni, R., Tritto, V., Bigliotto, C., Bartolo, D. De, 2011. A Geostatistical Approach to Assess the Spatial Association between Indoor Radon Concentration, Geological Features and Building Characteristics: The Case of Lombardy Northern Italy. Int. J. Environ. Res. Heal. 8, 1420–1440.

Bourdon, B., Henderson, G.M., Lundstrom, C.C., Turner, S.P., 2003. Uranium – Series Geochemistry. Reviews, in Mineralogy and Geochemistry. Turner, S.P. (Eds.), ISBN: 13 978-0-939950-64-5. 656 pages.

Branion-Calles, M.C., Nelson, T.A., Henderson, S.B., 2015. Geospatial approach to the prediction of indoor radon vulnerability in British Columbia, Canada. J. Expo. Sci. Environ. Epidemiol. 26, 554–565.

Brus, D.J., De Gruijter, J.J., 1993. Design-based versus model-based estimates of spatial means: Theory and application in environmental soil science. Environmetrics 4, 123–152.

Buda, G., 1981. Genesis of the Hungarian granitoid rocks. Acta Geol. Acad. Sci. Hungaricae 24, 309–318.

Buja, K., Menza, C., 2013. Sampling Design Tool for ArcGIS. Instruction for ESRI ArcGIS 10.0 Service Pack 3 or higher. Silver Spring. National Centers for Coastal Ocean Science, 16 pages.

Burján, Z., Nagy-Balogh, J., Gál-Sólymos, K., Szabó, C., 2002. Spectrochemical study of potential source minerals of radon anomaly. Microchem. J. 73, 47–51.

Burrough, P., 1986. Principles of Geographical Information Systems for Land Resources Assessment, in: Principles of Geographical Information Systems for Land Resources Assessment. Oxford: Clarendon Press, 45–67. ISBN: 0-19-854592-4.

Carter, M.R., Gregorich, E.G., 2008. Soil Sampling and Methods of Analysis, 2nd ed. CRC Press. Taylor & Francis Group, Florida, USA. ISBN-13: 978-0-8493-3586-0. 1263 pages.

Chauhan, R.P.P., Nain, M., Kant, K., 2008. Radon diffusion studies through some building materials: Effect of grain size. Radiat. Meas. 43, S445–S448.

Chitra, N., Danalakshmi, B., Supriya, D., Vijayalakshmi, I., Sundar, S.B., Sivasubramanian, K., Baskaran, R., Jose, M.T., 2018. Study of Radon and Thoron exhalation from soil samples of different grain sizes. Appl. Radiat. Isot. 133, 75–80.

Cinelli, G., Tollefsen, T., Bossew, P., Gruber, V., Bogucarskis, K., Felice, L. De, Cort, M. De, 2018. Digital version of the European Atlas of natural radiation. J. Environ. Radioact. Article in. 196, 240-252.

Cosma, C., Dancea, F., Jurcut, T., Ristoiu, D., 2001. Determination of ^{222}Rn emanation fraction and diffusion coefficient in concrete using accumulation chambers and the influence of humidity and radium distribution. Appl. Radiat. Isot. 54, 467–473.

Cothern, C.R., Smith, J.E.J., 1987. Environmental Radon. Springer Science & Business Media, New York. ISBN 978-1-4899-0475-1, 369 pages.

Council Directive 2013/59/Euratom, 2013. Euratom Basic Safety Standards BSS. Off. J. Eur. Union 1–73.

Das, B.M., 2008. Advance Soil Mechanics. third ed. Taylor & Francis. New York. ISBN 0-203-93584-5, 594 pages.

Davis, J.C., 2011. Statistics and data analysis in geology. J. Wiley & Sons, India. 2nd ed. ISBN-13: 978-0471837435. 656 pages.

De Cort, M., Gruber, V., Tollefsen, T., Bossew, P., Janssens, A., 2011. Towards a European Atlas of Natural Radiation: goal, status and future perspectives. Radioprotection 46, 737–743.

Drury, S., 1987. Image Interpretation in Geology. Allen and Unwin, London, UK. ISBN: 0045500371.

Durrani, S.A., Ilic, R., 1997. Radon Measurements by Etched Track Detectors. Applications in Radiation Protection. World Scientific. ISBN: 978-9810226664. 416 pages.

Durridge Company Inc., 2018. Soil gas probe, in-ground radon detection accessory for the RAD7. User manual. DURRIDGE Company Inc. Revision 2018-11-01. 15 pages.

Eijkelkamp, 2009. 07 Sample ring kits. Operating instructions. Eijkelkamp Agrirsearch Equipment. 12 pages.

EPA, 2004. Understanding variation in partition coefficient Kd values Volume III: Review of geochemistry and available Kd values for americium, arsenic, curium, iodine, neptunium, radium, and technetium. Report EPA 402-R-04-002C. Office of Air and Radiation. Environmental Protection Agency. United States, Washington.

ESRI, 2016. How Create Random Points works. ArcGIS Deskt. Environmental Systems Research Institute, Inc. URL http://desktop.arcgis.com/en/arcmap/10.3/tools/data-management-toolbox/how-create-random-points-works.htm (accessed 7.16.18).

Evans, I.S., 1972. General geomorphometry, derivatives of altitude, and descriptive statistics, in Chorley, R.J. (Ed.), Spatial Analysis in Geomorphology. Methuen & Co. Ltd. London. 17–90.

Faure, G., Mensing, T.M., 2005. Isotopes: Principles and applications, 3rd ed. Wiley. ISBN: 0471384372. 897 pages.

Ferro, V., Mirabile, S., 2012. Comparing particle size distribution analysis by sedimentation and laser diffraction Method. J. Agric. Eng. 2, 35-43.

Folkerts, K.H., Keller, G., Muth, H., 1984. An experimental study on diffusion and exhalation of ^{222}Rn and ^{220}Rn from building materials. Radiat. Prot. Dosimetry. 9. 27-34.

Garbrecht, J., Martz, L.W., 1995. Agricultural research service publication NAWQL 95-3, in: TOPAZ: An Automated Digital Landscape Analysis Tool for Topographic Evaluation, Drainage Identification, Watershed Segmentation and Subcatchment Parameterization. TOPAZ User Manual. - U.S. Department of Agriculture. 95-103.

García-Talavera, M., García-Pérez, A., Rey, C., Ramos, L., 2013. Mapping radon-prone areas using γ-radiation dose rate and geological information. J. Radiol. Prot. 33, 605–620.

Gonzalez, R.C., Woods, R.E., 1993. Digital Image Processing, third. ed. Prentice Hall, Upper Saddle River, N.J. 793 pages.

Greeman, D.J., Rose, A.W., 1996. Factors controlling the emanation of radon and thoron in soils of the eastern U.S.A. Chem. Geol. 129, 1–14.

Guibas, L., Stolfi, J., 1985. Primitives for the manipulation of general subdivisions and the computation of Voronoi diagrams. ACM Trans. Graph. 4, 74–123.

Gurau, D., Stanga, D., Dragusin, M., 2014. Review of the principal mechanism of radon in the environment. Rom. J. Phys. 59, 904–911.

Gyalog, L., Horváth, I., 1999. Geological map of the Velence hills, 1:25000 scale. Geological Institute of Hungary, Budapest, Hungary.

Hansen, J.S., Damkjaer, A., 1987. Determining ^{222}Rn diffusion lengths in soils and sediments. Health Phys. 53, 455–9.

Hassan, N.M., Hosoda, M., Ishikawa, T., Sorimachi, A., Sahoo, S.K., Tokonami, S., Fukushi, M., 2009. Radon Migration Process and Its Influence Factors; Review. Japanese J. Heal. Phys. 44, 218–231.

Hiemstra, P.H., Pebesma, E.J., Twenhöfel, C.J.W., Heuvelink, G.B.M., 2009. Real-time automatic interpolation of ambient gamma dose rates from the Dutch radioactivity monitoring network. Comput. Geosci. 35, 1711–1721.

Hillel, D., 1998. Environmental soil Physics. Elsevier, San Diego, USA. ISBN-13:978-0-12-348525-0. 761 pages.

Hirst, W., Harrison, G.E., 1939. The diffusion of radon gas mixtures. Proc. R. Soc. London. Ser. A. Math. Phys. Sci. 169, 573–586.

Horváth, I., Daridáné Tichy, M., Dudko, A., Gyalog, L., Ódor, L., 2004. Geology of the Velence Hills and the Balatonfő. Geological Institute of Hungary, Budapest. ISBN: 963-671-237-9. 316 pages.

Hosoda, M., Sorimachi, A., Yasuoka, Y., Ishikawa, T., Sahoo, S.K., Furukawa, M., Hassan, N.M., Tokonami, S., Uchida, S., 2009. Simultaneous Measurements of Radon and Thoron Exhalation Rates and Comparison with Values Calculated by UNSCEAR Equation 50, 333–343.

IAEA, 2014. Behavior of Radium. International Atomic Energy Agency. Technical reports 746. Revised Edition. ISBN 978–92–0–143310–7. 267 pages.

ICRU-51, 1993. Quantities and units in radiation protection, International Commission on Radiation Protection. Report 51. Maryland, USA. ISBN 0-913394-50-5. 17 pages.

Ielsch, G., Ferry, C., Tymen, G., Robé, M.C., 2002. Study of a predictive methodology for quantification and mapping of the radon-222 exhalation rate. J. Environ. Radioact. 63, 15–33.

Ishimori, Y., Lange, P., Martin, P., Mayya, Y.S., Phaneuf, M., 2013. Measurement and Calculation of Radon Releases from NORM Residues. International Atomic Agency Energy Agency. Technical reposts series 474. Vienna, Austria. ISBN: 978-92-0-142610-9. 85 pages.

Jiang, H., Ge, L., Lin, Y., Gu, Y., 2011. Preliminary Study on a Regional Radon Concentration in Surface Soil Prediction Method. Prog. Nucl. Sci. Technol. 1, 364–367.

Jordan, G., Meijninger, B.M.L., van Hinsbergen, D.J.J., Meulenkamp, J.E., van Dijk, P.M., 2005. Extraction of morphotectonic features from DEMs: Development and applications for study areas in Hungary and NW Greece. Int. J. Appl. Earth Obs. Geoinf. 7, 163–182.

Jordan, G., Petrik, A., De Vivo, B., Albanese, S., Demetriades, A., Sadeghid, M., Team, the GEMAS Project Team., 2018. GEMAS: Spatial analysis of the Ni distribution on a continental-scale using digital image processing techniques on European agricultural soil data. J. Geochemical Explor. 186, 143-157.

Jordan, G., 2007. Digital Terrain Analysis in a GIS Environment. Concepts and Development, in Peckham, R.J., Jordan, G. (Eds.), Digital Terrain Modelling. Development and Applications in a Policy Support Environment. Springer-Verlag Berlin. ISBN: 978-3-540-36730-7. 2–39.

Konert, M., Vandenberghe, J., 1997. Comparison of laser grain size analysis with pipette and sieve analysis: A solution for the underestimation of the clay fraction. Sedimentology 44, 523–535.

Li, M., Wilkinson, D., Patchigolla, K., 2005. Comparison of particle size distributions measured using different techniques. Part. Sci. Technol. 23, 265–284.

Lilley, J.S., 2001. Nuclear Physics: Principles and Applications, first. ed. Wiley, Manchester. ISBN: 0-471-97936-8. 393 pages.

Mann, H.B., Whitney, D.R., 1947. On a Test of Whether One of Two Random Variables Is Stochastically Larger Than the Other. Ann. Math. Stat. 18, 50–60.

Manohar, S.N., Meijer, H.A.J., Herber, M.A., 2013. Radon flux maps for the Netherlands and Europe using terrestrial gamma radiation derived from soil radionuclides. Atmos. Environ. 81, 399–412.

Markkanen, M., Arveka, H., 1992. Radon emanation from soils. Radiat. Prot. Nuclear Technology Publishing. Dosimetry 45, 269–272.

Merkus, H., 2009. Particle Size Measurements. Fundamentals, Practice, Quality. Springer. ISBN: 978-1-4020-9015-8. 533 pages.

Mezősi, G., 2015. Granite Weathering in the Velence Hills, in: Lóczy, D. (Ed.), in Landscapes and Landforms of Hungary. Springer International Publishing. 89–95. ISBN: 978-3-319-08997-3. 294 pages.

Moldrup, P., Poulsen, T.G., Schjønning, P., Olesen, T., Yamaguchi, T., 1998. Gas Permeability in Undisturbed Soils: Measurements and Predictive Models. Soil Sci. 163, 180–189.

Morawska, L., Philllips, C.R., 1993. Dependence of the Radon Emanation Coefficient on Radium Distribution and Internal Structure of the Material. Geochim. Cosmochim. Acta 57, 1783–1797.

Nathwani, J.S., Phillips, C.R., 1979a. Adsorption of ^{226}Ra by soils (I). Pergamon Press Ltd. Great Britain. Chemosphere 5, 285–291.

Nathwani, J.S., Phillips, C.R., 1979b. Adsorption of ^{226}Ra by soils in the presence of Ca^{2+} ions. Specific adsorption (II). Pergamon Press Ltd. Great Britain. Chemosphere 8, 293–299.

Nazaroff, W.W., 1992. Radon Transport from Soil to Air. American Geophysical Union. Rev. Geophys. 30, 137-160.

Nazaroff, W.W., Nero, A. V., 1988. Radon and its decay products in the indoor air. John Wiley & Sons, California, USA. ISBN: 0-471-62810-7. 518 pages.

NERMS, 2014. OKSER 2013. Annual Report of the National Environmental Radiological Monitoring System. p. 86.

Neznal, Me., Neznal, Ma, Matolín, M., Barnet, I., Miksova, J., 2004. The new method for assessing the radon risk of building sites. In Czech Geol. Survey Special Papers, vol. 16. Czech Geol. Survey, Prague. http://www.radon-vos.cz/pdf/ metodika.pdf.

Nielson, K.K., Bollenbacher, M.K., Rogers, V.C., Woodruff, G., 1989. Users Guide for the MK-II Radon/Permeability Sampler: U. S. Environmental Protection Agency.

Pansu, M., Gautheyrou, J., 2006. Handbook of soil analysis: mineralogical, organic and inorganic methods. Springer-Verlag Berlin Heidelberg. ISBN: 9783540312109. 993 pages.

Pásztor, L., Zsuzsanna, K., Szatmári, G., Laborczi, A., Horváth, Á., 2016. Mapping geogenic radon potential by regression kriging. Sci. Total Environ., 544, 883–891.

Pereira, A., Lamas, R., Miranda, M., Domingos, F., Neves, L., Ferreira, N., Costa, L., 2017. Estimation of the radon production rate in granite rocks and evaluation of the implications for geogenic radon potential maps: A case study in Central Portugal. J. Environ. Radioact. 166, 270–277.

Petersell, V., Jüriado, K., Raukas, A., Shtokalenko, M., Täht-Kok, K., 2015. Quaternary deposits and weathered bedrock material as a source of dangerous radon emissions in Estonia. Geologos 21, 139–147.

Porstendorfer, J., 1994. Properties and behaviour of Radon and Thoron and their decay products in the air. J. Aerosol Sci. 25, 219–263.

Quindós, L.S., Fernández, P.L., Sainz, C., Fuente, I., Nicolás, J., Quindós, L., Arteche, J., 2008. Indoor radon in a Spanish region with different gamma exposure levels. J. Environ. Radioact. 99, 1544–1547.

Ramli, A.T., Hussein, A.W.M.A., Lee, M.H., 2001. Geological influence on terrestrial gamma radiation dose rate in the Malaysian State of Johore. Appl. Radiat. Isot. 54, 327–333.

Reimann, C., Filzmoser, P., Garrett, R.G., Dutter, R., 2008. Statistical data analysis explained. Applied Environmental Statistics with R. West Sussex, England. John Wiley & Sons, Ltd. ISBN: 978-0-470-98581-6. 343 pages.

Rodgers, J.L., Nicewander, W.A., 1988. Thirteen ways to look at the correlation coefficient. Am. Stat. 42, 59–66. doi:10.1080/00031305.1988.10475524

Rogers, V.C., Nielson, K.K., 1991a. Correlations for Predicting Air Permeabilities and ^{222}Rn Diffusion Coefficients of Soils. Health Phys. 61, 225–230.

Rogers, V.C., Nielson, K.K., 1991b. Multiphase radon generation and transport in porous materials. Health Phys. 60, 807–815.

Sander, R., 2015. Compilation of Henry's law constants (version 4.0) for water as solvent. Atmos. Chem. Phys. 15, 4399–4981.

Sanusi, M.S.M., Ramli, A.T., Gabdo, H.T., Garba, N.N., Heryanshah, A., Wagiran, H., Said, M.N., 2014. Isodose mapping of terrestrial gamma radiation dose rate of Selangor state, Kuala Lumpur and Putrajaya, Malaysia. J. Environ. Radioact. 135, 67–74.

Sas, Z., Szántó, J., Kovács, J., Somlai, J., Kovács, T., 2015. Influencing effect of heat-treatment on radon emanation and exhalation characteristic of red mud. J. Environ. Radioact. 148, 27–32.

Schaefer, B., 2016. Radiogenic isotope geochemistry. A Guide for Industry Professionals, 1st ed. Cambridge University Press, Sidney, Australia. ISBN: 978-1-107-03958-2. 196 pages.

Shweikani, R., Giaddui, T.G., Durrani, S.A., 1995. The effect of soil parameters on the radon concentration values in the environment. Radiat. Meas. 25, 581–584.

Smith, K.A., Mullins, C.E., 2000. Soil and Environmental analysis. Practical methods, 2nd. ed. Marcel Dekker, Inc., New York. ISBN 0-8247-0414-2. 637 pages.

Spiess, A.-N., 2018. Package 'propagate'. Propagation of uncertainty using higher-order Taylor expansion and Monte Carlo simulation. R-software package. Cran-r project. https://cran.r-project.org/web/packages/propagate/index.html.

Sposito, G., 2008. The chemistry of soils. 2nd. ed. Oxford University Press, Inc., New York. ISBN 978-0-19-531369-7. 329 pages.

Straden, E., Kolstad, K., Lind, B., 1984. The influence of moisture and temperature on radon exhalation. Radiat. Prot. Dosimetry 7, 55–59.

Szabó, C., Kubovics, I., Molnár, Z., 1993. Alkaline lamprophyre and related dyke rocks in NE Transdanubia, Hungary: The Alcsutdoboz-2 (AD-2) borehole. Mineral. Petrol. 47, 127–148.

Szabó, K.Z., Jordan, G., Horváth, Á., Szabó, C., 2014. Mapping the geogenic radon potential: Methodology and spatial analysis for central Hungary. J. Environ. Radioact. 129, 107–120.

Szabó, K.Z., Jordan, G., Petrik, A., Horváth, Á., Szabó, C., 2017. Spatial analysis of ambient gamma dose equivalent rate data by means of digital image processing techniques. J. Environ. Radioact. 166, 309–320.

Szegvary, T., Conen, F., Stöhlker, U., Dubois, G., Bossew, P., de Vries, G., 2007. Mapping terrestrial g-dose rate in Europe based on routine monitoring data. Radiat. Meas. 42, 1561–1572.

Takahashi, S., Ikeda, T., Shinagawa, Y., Kunii, T.L., Ueda, M., 1995. Algorithms for extracting correct critical points and constructing topological graphs from discrete geographical elevation data. Comput. Graph. Forum.

Takeno, N., 2005. Atlas of Eh-pH diagrams. Intercomparison of thermodynamic databases. Geol. Surv. Japan Open File Rep. No.419. National Institute of Advanced Industrial Science and Technology Research Center for Deep Geological Environments. 285 pages.

Tanner, A.B., 1980. Radon migration in the ground: a supplementary review. In Gesell, T. F. and Lowder, W. M., Proceedings Natural Radiation Environment III. Technical Information Service, US Department of Energy, Washington D.C. p. 5-56.

Thorne, M., Mitchell, N., 2011. NDA RWMD Biosphere Assessment Studies FY2010-2011: The Biosphere Transport, Distribution and Radiological Impact of Uranium Series Radionuclides from a Geological Disposal Facility. Report QRS-1378ZM-5. Nuclear Decommissioning Authority (NDA) Radioactive Waste Management Directorate (RWMD). 171 pages.

Tukey, J.W., 1977. Exploratory Data Analysis, 1st ed. Addison Wesley. ISBN: 978-0201076165 712 pages.

UNSCEAR, 2008. Sources and Effects of Ionizing Radiation. United Nations Scientific Committee on the Effects of Atomic Radiation UNSCEAR 2008 Report to the General Assembly Scientifics Annexes A and B. in Vol. 1 Sources. New York. p 223-463.

UNSCEAR, 2000. Sources and Effects of Ionizing Radiation. United Nations Scientific Committee on the Effects of Atomic Radiation UNSCEAR 2000 Report to the General Assembly Scientifics Annexes. in Vol. 1 Sources. New York. p 83-156.

USDA, 2014. Soil Survey Field and Laboratory Methods Manual. Soil Survey Investigations Report No. 51. Version 2. Nebraska, USA.

Várhegyi, A., Somlai, J., Sas, Z., 2013. Radon migration model for covering U mine and ore processing tailings. Rom. Reports Phys. 58, 298–310.

Wang, J.F., Stein, A., Gao, B.B., Ge, Y., 2012. A review of spatial sampling. Spat. Stat. 2, 1–14.

Washington, J.W., Rose, A.W., 1992. Temporal variability of radon concentration in the interstitial gas of soils in Pennsylvania. J. Geophys. Res. 97, 9145–9159.

Weigel, F., 1978. Radon. Chem. Inst. for Inorganic Chemistry Munich University. Ztg 102, 287–299.

Wilhelm, E., Battino, R., Wilcock, R., 1976. Low-pressure solubility of gases in liquid water. Chemical Review. 77, 129-262.

Yakovleva, V.S., 2005. A theoretical method for estimating the characteristics of radon transport in homogeneous soil. Ann. Geophys. 48, 195-198.

Yeşilkanat, C.M., Kobya, Y., Taşkin, H., Çevik, U., 2015. Dose rate estimates and spatial interpolation maps of outdoor gamma dose rate with geostatistical methods: A case study from Artvin, Turkey. J. Environ. Radioact. 150, 132–144.

Yu, C., Kamboj, S., Cheng, J.J., 2015. Data collection Handbook to support modeling aspects of radioactive material in soil and building structures. Environmental Science Division. Argonne National Laboratory. ANL/EVS/TM/14-4. Chicago, USA.

Annex I.
Soil properties descriptive statistics and scatter plot

In the following figures of descriptive statistics in the left site and scatterplot by each measurement sites are shown for the several soil properties. The descriptive statistics plots include, in the upper side the corresponding histogram of the measures parameter overlaid with the cumulative density function (CDF) and in the bottom the box-and-whiskers plot shows the position of the median value and an indication of the existence of outliers. Overlaid to the box-and-whiskers plot, are the scatter plot, with the scale alienated to the upper plot, that shows the number of measurements corresponding to the respective bin of the histogram. On the left side is the corresponding scatter plot each sampling site, where the error bar represents the standard deviation from the replicates or the error of measurements in other cases.

Bulk density of dry soil

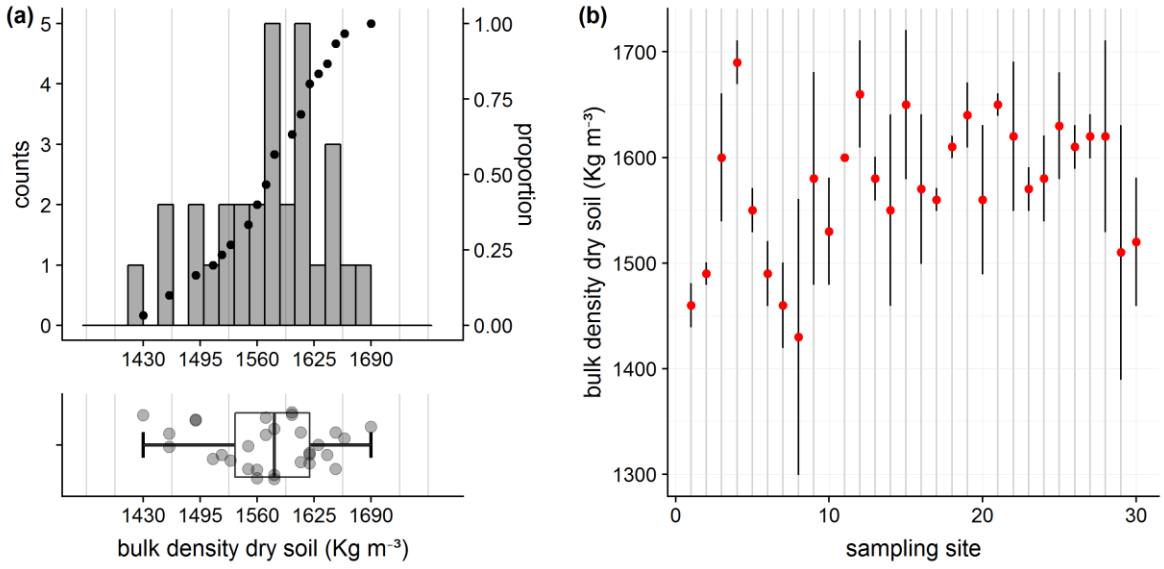

Figure a 1. Descriptive statistics and scatter plot of bulk density of dry soil

Gravimetric water content

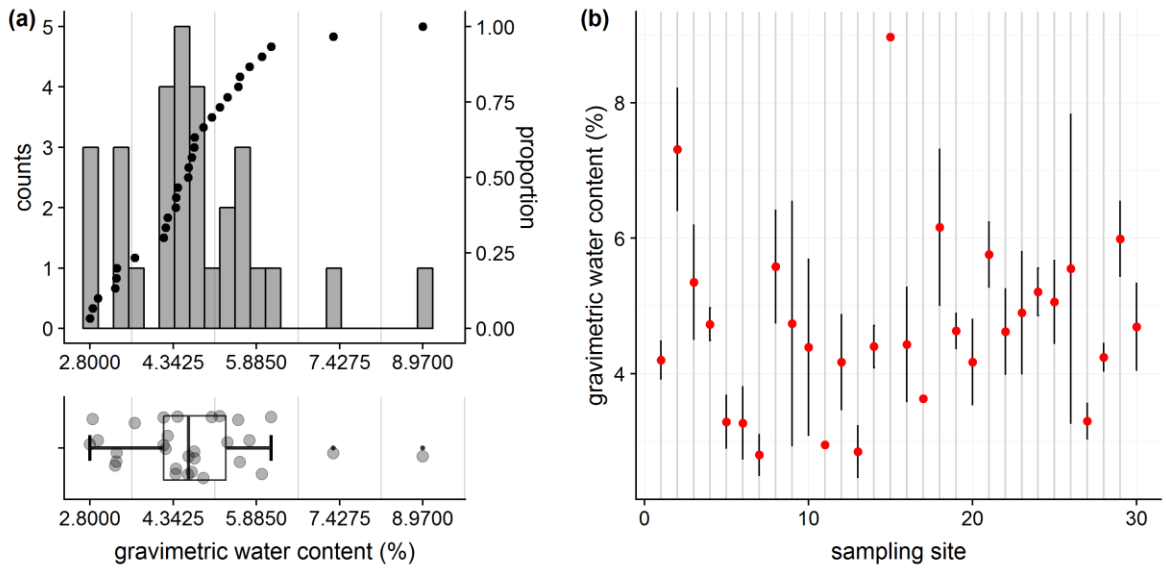

Figure a 2. Descriptive statistics and scatter plot of gravimetric water content

Total porosity

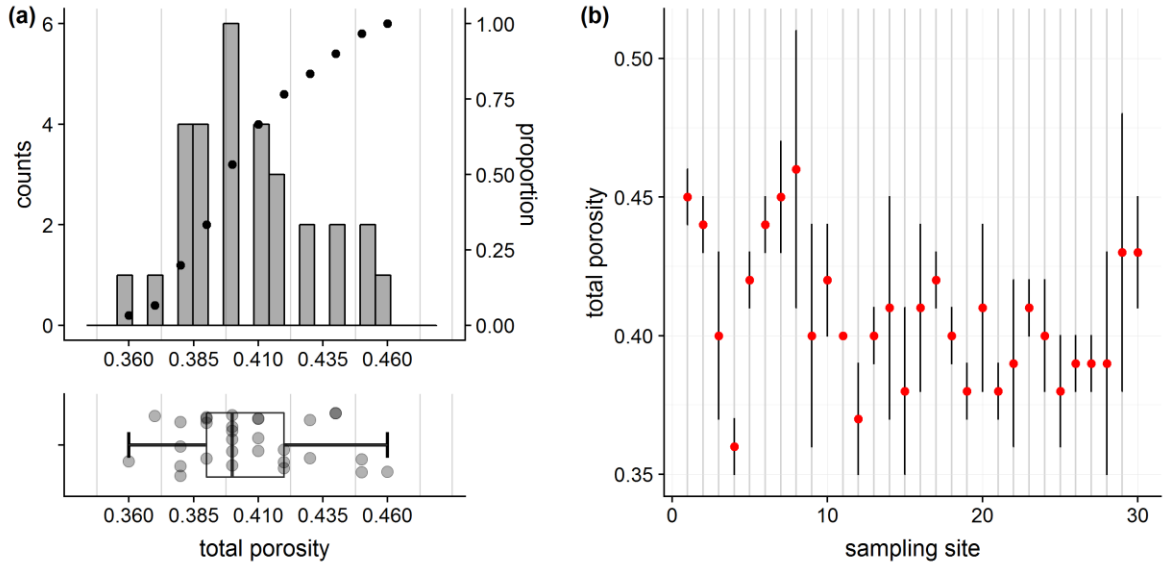

Figure a 3. Descriptive statistics and scatter plot of total porosity

Volume fraction of water saturation

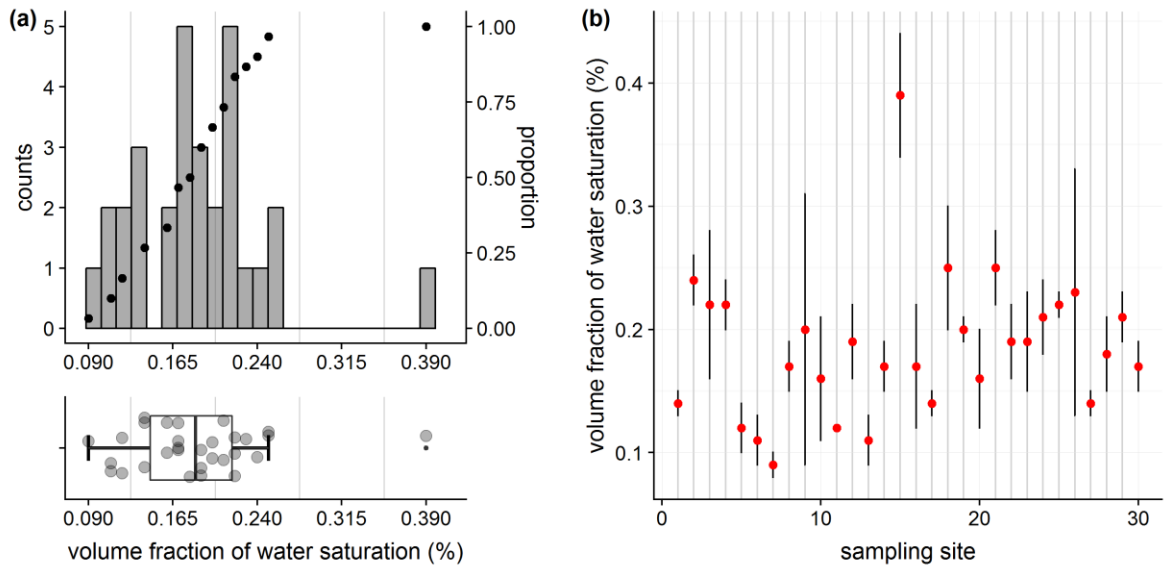

Figure a 4. Descriptive statistics and scatter plot of volume fraction of water saturation

Soil pH in distilled water

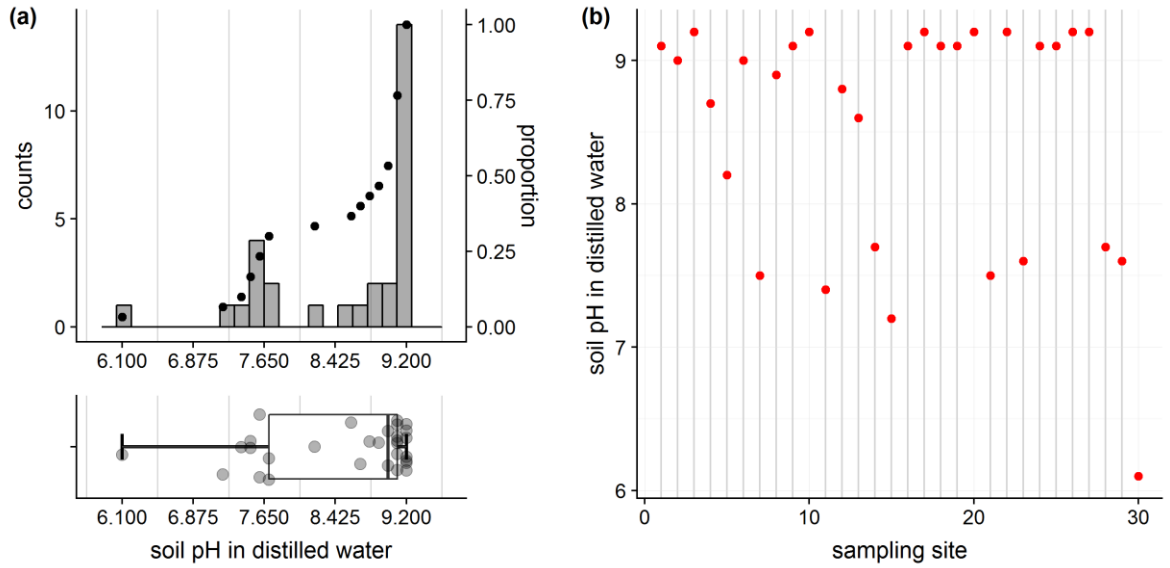

Figure a 5. Descriptive statistics and scatter plot of soil pH in distilled water

Carbonate content

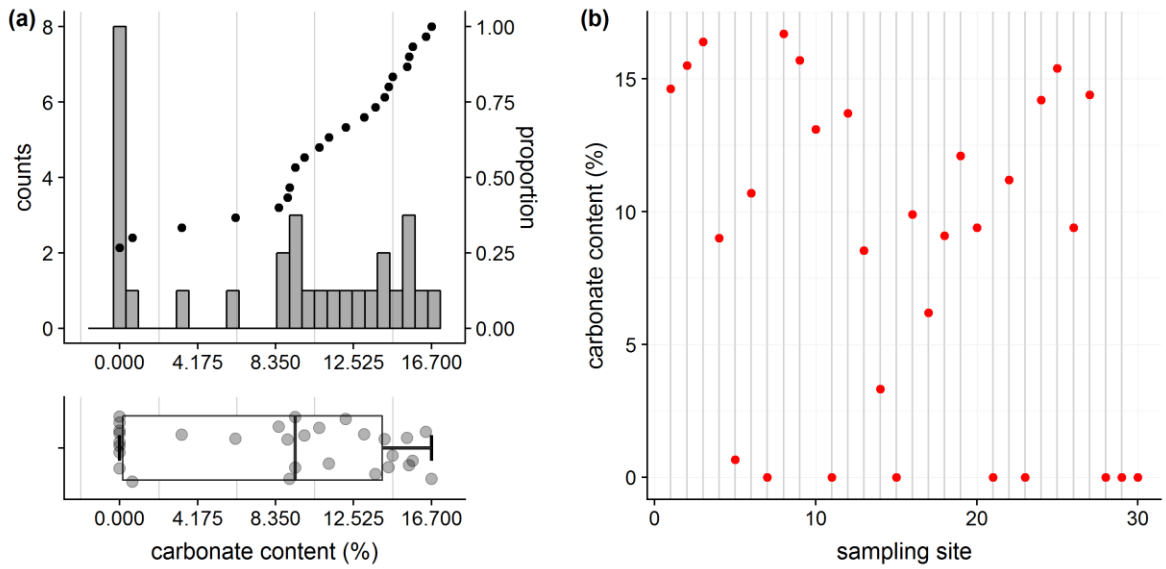

Figure a 6. Descriptive statistics and scatter plot of carbonate content of soil

Organic material content

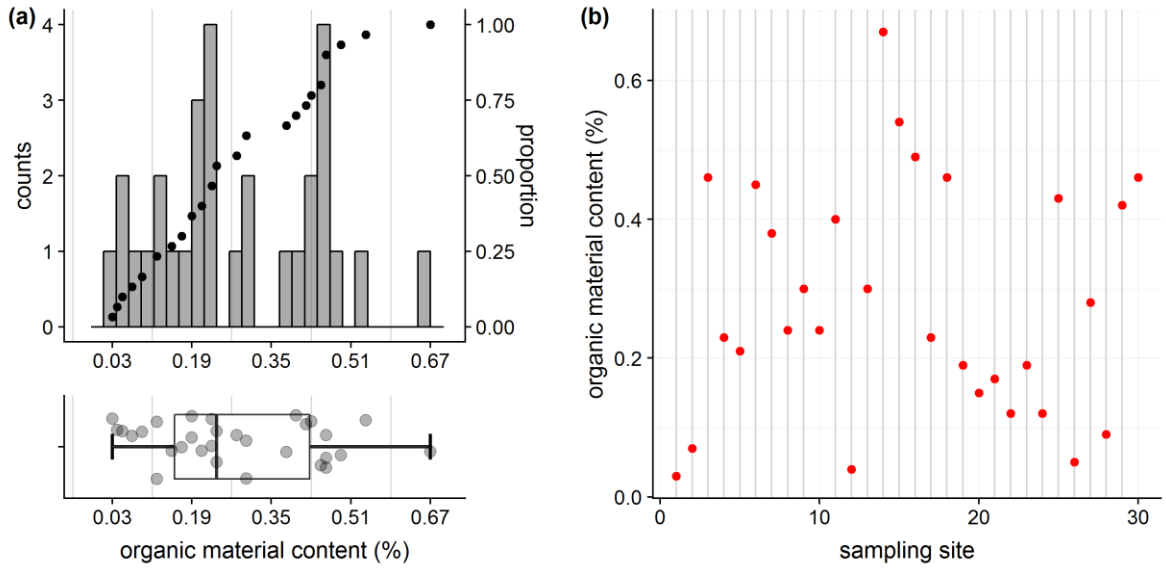

Figure a 7. Descriptive statistics and scatter plot of material content of soil

Annex II.
Particle size distribution

The log normal distribution of the grain size analysis is shown in the following figure as an example from the 30 sampling sites.

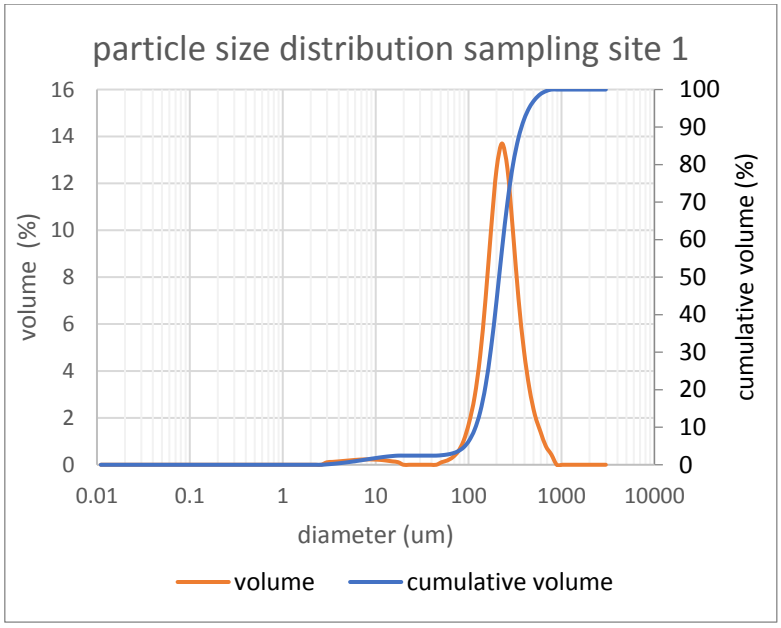

DOI: 10.15476/ELTE.2019.178